2010

The Development Of Scalable Pump Techniques For Gg Iag Fiber Lasers And Passive Athermalization Techniques For Solid State Laser

William Hageman
University of Central Florida

THE DEVELOPMENT OF SCALABLE PUMP TECHNIQUES FOR GG IAG FIBER LASERS AND PASSIVE ATHERMALIZATION TECHNIQUES FOR SOLID STATE LASERS

by

WILLIAM B. HAGEMAN
B.S. Kansas State University, 1999
M.S. Kansas State University, 2000
M.S. Kansas State University, 2002
M.S. University of Central Florida, 2008

A dissertation submitted in partial fulfillment of the requirements
for the degree of Doctor of Philosophy in Optics
in the College of Optics and Photonics
at the University of Central Florida
Orlando, Florida

Spring Term
2010

Major Professor: Michael Bass

ABSTRACT

This dissertation consists of two parts: research pertaining to the development of scalable pump techniques for gain guided index-antiguided fiber lasers and research relating to the development of passive athermalization schemes for solid state lasers.

The first section primarily details the development of a side pump scheme that allows for power scaling of gain-guided index anti-guided fibers. While these fibers have been demonstrated in past research, none have used a pump technology capable of pumping with the efficiencies, uniformity, and necessary length to allow for scaling of the fiber lasers to high output powers. The side pumped scheme developed in this section demonstrates a 6 W output power fiber laser with room for improvement in efficiency and beam quality.

The second section details work done on the development of technologies for passively athermalizing the output of solid state laser systems. Techniques for passively removing the dependence of laser output power/energy on the operating temperature of the laser system promise to reduce the weight, power consumption, and cost of fielded laser systems. Methods for achieving passive athermalization are discussed, as well as prior research in laser athermalization, background theory, enabling technologies, and experimental results. This work provides the basis for continued research of passive athermalization and the eventual demonstration of this technology.

This dissertation is dedicated to my wonderful wife Amy, and beautiful children Annika and Daniel.

ACKNOWLEDGMENTS

I would like to thank my advisor Dr. Michael Bass for all of his insight, support, and friendship throughout this research and my time at CREOL. Without his help, none of this would be possible.

I would also like to thank the members of my committee, Dr. Glenn Boreman, Dr. Patrick LiKamWa, and Dr. Louis Chow for their time, patience, and input throughout the dissertation process.

I would like to acknowledge the help of all of my colleagues in the Bass group and throughout the College of Optics. I would like especially acknowledge the help of Ms. Ying Chen for her advice both in the lab and at the chalkboard, which has helped me through many problems. I would also like to thank Dr. Xiangru Wang, Dr. Shaofeng Guo, and Dr. Gyu Ug Kim for their contributions to this research.

I would like to thank the financial support by DoD JTO MRI Contract No. W911NF-05-1-0517, the U.S. Army Night Vision and Electronic Systems Directorate under Contract No. W15P7T-06-D-R401, the State of Florida, and Sandia National Laboratory. I would also like to acknowledge support from Northrop Grumman Laser Systems in supplying both passive q-switch materials and sound advice.

Finally, I would like to thank my wife Amy, daughter Annika, son Daniel, and all of my parents and family for all of their help and support throughout the course of this work. Without their love and sacrifice, I could never even have imagined being able accomplish so much. Thank you!

TABLE OF CONTENTS

LIST OF FIGURES

LIST OF TABLES

PUMPING SCHEMES FOR GAIN GUIDED INDEX-ANTIGUIDED FIBERS

Introduction

While fiber lasers have been in existence since shortly after the initial development of the laser itself [1, 2], they have only relatively recently become a ubiquitous part of the modern laser landscape [3]. Fiber lasers hold several basic advantages over traditional bulk solid state laser systems. They can have very simple geometries with minimal free space alignment, making them good candidates for applications where physical compactness and ruggedness is desired. Their inherent modal output allows for high beam quality with inherent thermal and physical stability. In addition, fibers have an inherently high surface area to active volume ratio, which facilitates thermal management. All of these properties make the use of fibers as high-powered oscillators and amplifiers a technology of great potential [3].

One of the areas of greatest interest in pushing fiber laser technology to higher powers is the development of large mode area (LMA) fibers. One of the key constraints preventing further power scaling of fiber lasers has been the limitation of the maximum mode area that can be achieved in a fiber laser while exhibiting single mode operation. Due to this limitation of the active mode area, fiber lasers that attempt to push to higher output powers while maintaining optimal output beam quality run into problems due to excessive power density in the fiber core. High power density in the doped core of the fiber leads to the emergence of undesired non-linear effects. Since nonlinear processes scale with the square of the electric field, the magnitudes of these effects increase directly with the power density of radiation present in the laser. These

nonlinear effects include stimulated Raman scattering (SRS), stimulated Brillouin scattering (SBS), self phase modulation, and self focusing [3, 4, 5]. While self focusing is independent of the core size of the fiber [3], the other non-linear effects listed here can all be mitigated increasing the core size and thus decreasing the power per mode area carried by the fiber.

Several types of LMA fibers have been developed and will be discussed in later sections. However, the technology that has led to the largest single mode areas seen in fiber lasers [6,7] is that of gain guided, index antiguided fibers (GG IAG). These fibers have produced single mode lasing in core sizes as large as 400 μm in diameter and thus appear to have a great deal of potential for use as high power laser oscillators and amplifiers. However, all previous demonstrations of GG IAG fiber have had serious limitations in the ability to efficiently pump the lengths of fiber needed to effectively scale up the power of these devices. This dissertation section discusses work pertaining to the development of scalable pump techniques for GG IAG fibers.

History and Background of Fiber Laser Development

The advent of the fiber laser goes back to the beginning of the laser era and the first demonstration of lasing in a glass gain material. In 1961, Snitzer first published the observation of laser (then called 'optical maser') action of neodymium $^{3+}$ ions in barium crown glass [2, 8, 9]. This laser actually consisted of Nd $^{3+}$ doped barium glass rod surrounded by an undoped outer cladding. The experiment consisted of testing two fibers with core diameters of 300 μm and 32

μm, both with a length of 3 inches. Both fibers were pumped with helical flashlamps and used silvered end surfaces as reflectors.

While the fiber laser has been in existence since the early days of the laser, it was lost in the shadow of bulk, solid state laser systems until it began a resurgence with the onset of the optical fiber telecommunications industry and the advent of high brightness diodes as viable pump sources. In the 1970s, fiber lasers were demonstrated that were pumped both by diode end pumping and bulk laser pumping [10, 11]. The 1980s saw the use of silica as the host glass of choice for fiber lasers and the advent of the first single mode fiber laser [12], the first tunable fiber laser, and the first q-switched fiber laser [13,14].

Up through the 1980s, the output power of fiber lasers was limited by the ability of diode sources available at the time to effectively couple to the small single mode core of the optical fiber. The standard pump technique was to pump directly into the core of the fiber, letting the pump energy be absorbed as it propagated along the core. Since single mode, step index fibers have small core sizes (on the order of a few microns), the elliptical nature of the available high power diode pump sources and the small output power of single transverse mode pump sources greatly reduced the pump efficiency that could be obtained. In 1988, Snitzer [15] introduced a new end pump technique, the use of a 'double-clad fiber', which has become the standard method for pumping to this day. Figure 1 below shows a diagram of a typical double-clad fiber. This type of fiber geometry uses a typical high index doped core glass surrounded by a lower index cladding (an in a traditional fiber). However, the cladding glass is then surrounded by a second cladding of even lower index, allowing light introduced into the first cladding to guide

down the length of the fiber. In this way, light end pumped into the first cladding of the fiber slowly refracts into the core of the fiber, allowing for longer pumped fiber lengths and a much larger end pump area even when using small diameter laser cores.

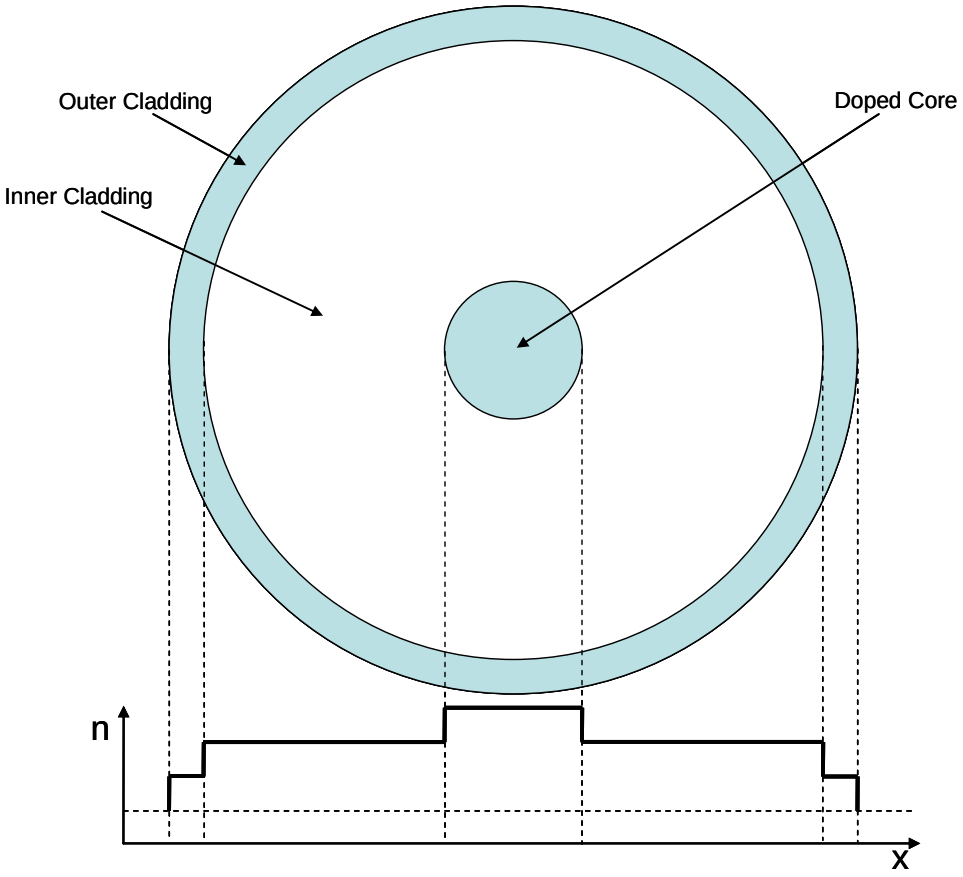

Figure 1 - Schematic of double clad fiber and its index profile. The index of the core is higher than the inner cladding index, which is in turn higher than the index of the outer cladding.

The advent of the double clad fiber allowed a rapid advancement in the power obtained from fiber lasers, with a record high power of 110W demonstrated in 1999 [16]. With the removal of pump power as the limiting factor in the power scaling of fibers, the next stumbling

block for increasing the power of fiber lasers became optical damage and undesirable non-linear effects that arose from very large power density in the small single mode core of the step index fiber [16, 17, 18]. The most direct concept used to combat the problems arising from high power density in the core was to develop single mode fiber lasers with large mode areas (LMA). LMA technologies allowed the rapid increase in fiber laser output power from 110W up to 3kW over the space of just 7 years [19]. A wide array of LMA techniques will be discussed in more detail in the following section.

Large Mode Area Fiber Designs

There are a number of fiber designs that have been developed to create large mode areas while maintaining lower order mode output. While mode area is correlated with core size, the area of the mode is not necessarily equal to the size of the core. Due to the non-uniform nature of the modes in the fiber core and the extension to greater or lesser degree of the core modes into the surrounding cladding, the effective area of a mode can be larger or smaller than the actual core size of the fiber.

The basic equation that governs the number of modes propagating is a step index fiber is the V parameter [20], which is defined as:

(1) $$V = \frac{2\pi}{\lambda_0} a \sqrt{n_{core}^2 - n_{clad}^2}$$

Here λ_0 is the free space wavelength of light in the fiber, *a* is the core radius of the fiber, n_{core} is the index of refraction of the fiber core, and n_{clad} is the index of refraction of the fiber cladding. When the V parameter reaches values of greater than 2.405 (the first zero in the J_0 Bessel function), only the fundamental (LP_{01}) mode can be sustained in the fiber. This sets a limit as to how large a fiber core can be before higher order modes begin to propagate in the fiber. Using this equation, a fiber with step index difference between core and clad of only 0.001 and operating at a wavelength of 1 μm would have a maximum single mode operation core radius of only 7 μm. A good approximation for the size of the lowest order mode in a step index fiber (when V is greater than 2.405) [21] is given by:

$$w_L = a\left(0.65 + \frac{1.619}{V^{3/2}} + \frac{2.879}{V^6}\right) \quad (2)$$

In equation (2), w_L is the radius of the lowest order mode, a is the radius of the fiber core, and V is the V parameter shown in (1).

Conventional Low Numerical Aperture Techniques

The first, and most basic LMA technique is the use of very low numerical apertures (NA), created by maintaining a very small index step between core and cladding. Low numerical apertures can create very weak guiding of higher order modes in the fibers with V parameters greater than 2.405. There are multiple methods then used to facilitate lasing in only the lowest order mode to the exclusion of the higher order modes allowed by large V parameters. The first LMA fiber of this type used a tailored dopant concentration in the core to facilitate gain in the

lowest order mode [22]. This resulted in high beam quality (M^2 of 1.3) with a core diameter of 21 μm.

Another method used to select single mode lasing in a multimode core is the combination of the use of low numerical aperture with intentional bending of the fiber. Losses for the high order modes increase with bending more rapidly than loses for the lowest order mode, making the bending a mode selection mechanism [23, 24, 25]. These fibers have an index profile as shown in Figure 2a with a very small index difference between clad and core, but large index difference between the pump cladding and outer cladding, giving weak guiding in the core but high numerical aperture for pump light.

Another conventional low numerical aperture LMA technique was the introduction of an M shaped dopant and index profile in the core of the fiber. This type of fiber had raised refractive index at the outer edges of the core (leading to its nickname of 'batman' fiber) which created a flatter mode profile across the core, resulting in larger mode areas (by a factor of 2-3 times) without increases in the core size itself [26,27]. A diagram of this type of fiber is shown in Figure 2b.

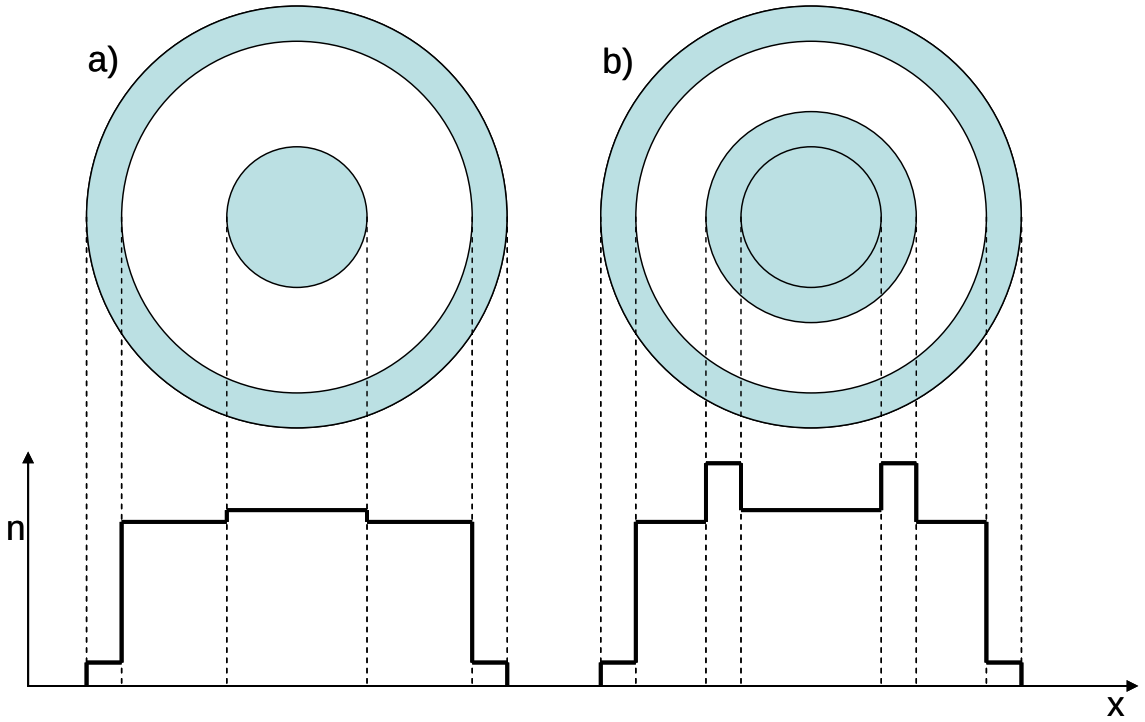

Figure 2 - Index profiles of: a) a standard low numerical aperture LMA fiber and b) an 'M' shaped (batman) flat-mode fiber.

Photonic Crystal Fibers (PCF)

Photonic crystal fibers are a class of fibers that use an organized structure of refractive index differences (through use of air holes or inclusion of glasses with high or low refractive index) to modify the numerical aperture of the core to a value less than that which can be obtained with conventional fiber fabrication processes [28, 29].

The first type of PCF fiber used for creating high power fiber lasers was the air-filled, or holey fiber. In this type of fiber, air holes are used in the fiber to create the desired numerical aperture and create LMA single mode fibers. Figure 3 shows a diagram of a typical air-filled

fiber design. As illustrated in the diagram, the doped fiber core is surrounded by a periodic pattern of air gaps that produce the desired numerical aperture for core guiding. Surrounding this periodic structure is a ring of air gaps used to create a high NA inner cladding for pump purposes, with silica glass of unaltered index surrounding the 'air clad' to form the outer cladding.

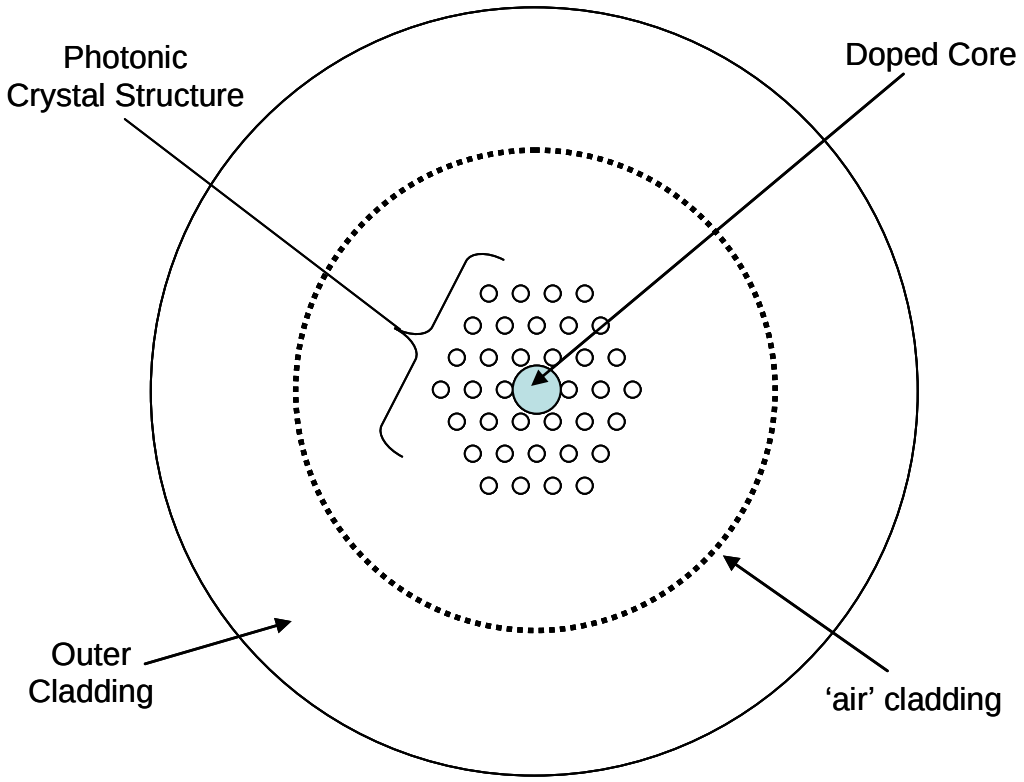

Figure 3 - Sketch of a typical LMA photonic crystal fiber.

PCF fibers can still be thought of as having a V parameter that controls the modes allowed to propagate in the fiber core. This effective V parameter, V_{eff}, can be approximated with the following equation.

$$V_{eff} = \frac{2\pi}{\lambda} \Lambda F^{1/2} \sqrt{n_0^2 - n_a^2} \quad (3)$$

Here Λ is the spacing between air holes, F is the fill factor of air (or other fill material) to glass, and n_a is the index of refraction of air or other fill material in the periodic structure. As seen before with equation (1), a V parameter of less than 2.405 will result in single mode propagation. One important thing to note is the lack of a core diameter term in the expression for V_{eff}. While this expression is approximate and does not hold for extremely large core sizes, a PCF set up in this manner can be an 'endlessly' single mode structure [30].

Another version of the PCF fiber is the all solid-core PCF. These fibers use low or high index materials to replace air in the periodic PCF structures. This allows for easier fabrication of fibers from preforms as well as easier cleaving and splicing of fibers once they are produced [31]. Otherwise, these fibers behave in much the same way as the more traditional holey fibers.

The final type of PCF to be discussed is the leakage channel fiber [32, 33, 34], which is sketched in Figure 4. These fibers utilize a series of low index regions surrounding the fiber core with bridges of core material reaching from the core to the surrounding cladding. This results in high order modes leaking from the core to the surrounding clad, allowing robust operation of the lowest order mode. These fibers have reached core diameters of up to 170 μm [32] with an all-solid design that allows for easy cleaving, splicing, and bending.

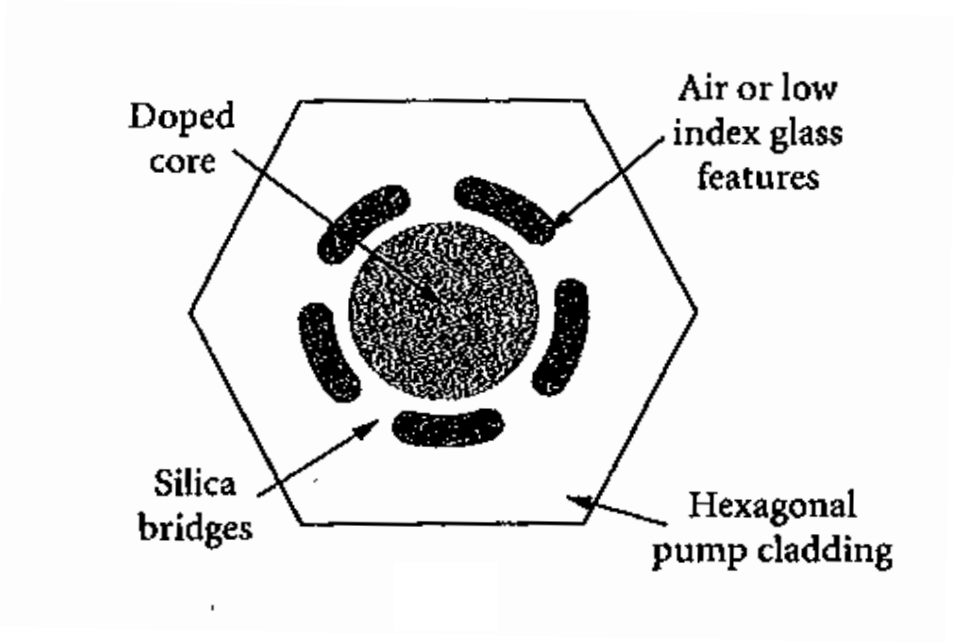

Figure 4 - Diagram of leakage channel fiber. Core is surrounded by low index glass with bridges of index equal to that of the core and cladding linking them. From [3].

Other LMA Technologies

Other LMA technologies have been used in addition to conventional fibers and PCF fibers. The chirally coupled core is a technology in which the primary core of the fiber is surrounded by a smaller, lossy core that wraps around the primary gain core in a helical pattern along the length of the fiber. The purpose of the secondary chiral core is to provide a loss mechanism for higher order modes that extend into the surrounding cladding from the central core [35, 36]. These fibers have the advantage of not needing a low numerical aperture main core in order to create very high quality single mode operation. However, the creation of the needed perform and the

twisted fiber pulling technique needed for fabrication are difficult. Figure 5 shows a diagram of the chiarally coupled core fiber.

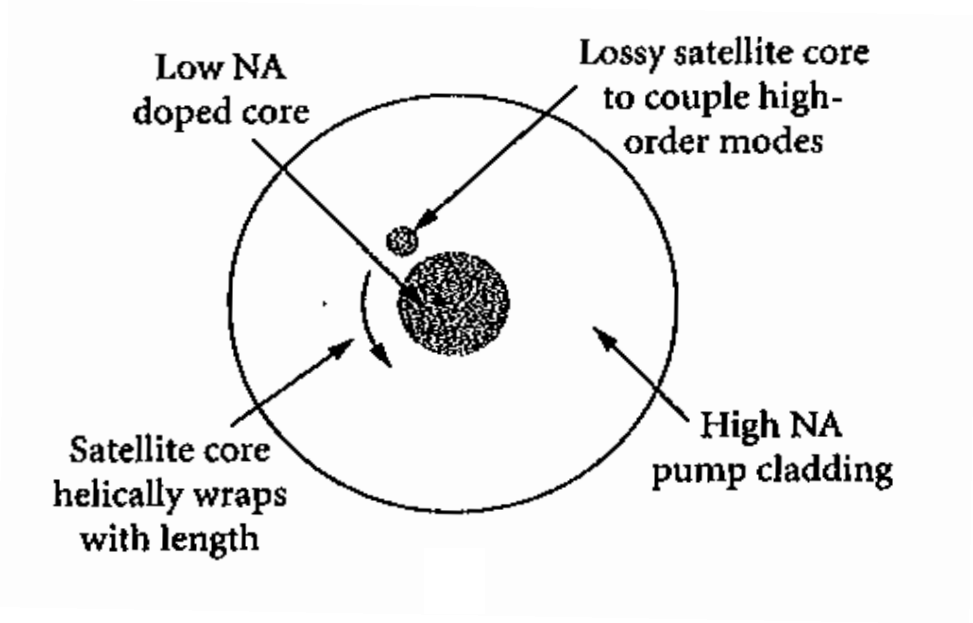

Figure 5 - Sketch of the cross section of a chirally coupled core fiber. The satellite core wraps helically around the length of the primary core providing loss to the higher order modes. From [3].

Another technique for power scaling is the use of multiple cores. This technique combines the light from many smaller cores into a high quality beam in the far field [37, 38]. While the multiple cores preclude the need for pushing the cores to low numerical apertures, the manufacture of multicore preforms is difficult due to the need drill holes and make insertions of several cores.

The final technique to be discussed and the technology around which this study is centered is the use of GG IAG fibers. As stated previously, this technique, where the refractive

index of the core glass is lower than that of the clad glass resulting in an index antiguided fiber, has resulted in the largest core sizes reported in a single mode fiber oscillator with cores of up to 400 μm in diameter [6, 7]. Figure 6 shows a sketch of the refractive index profile of a typical GG IAG fiber.

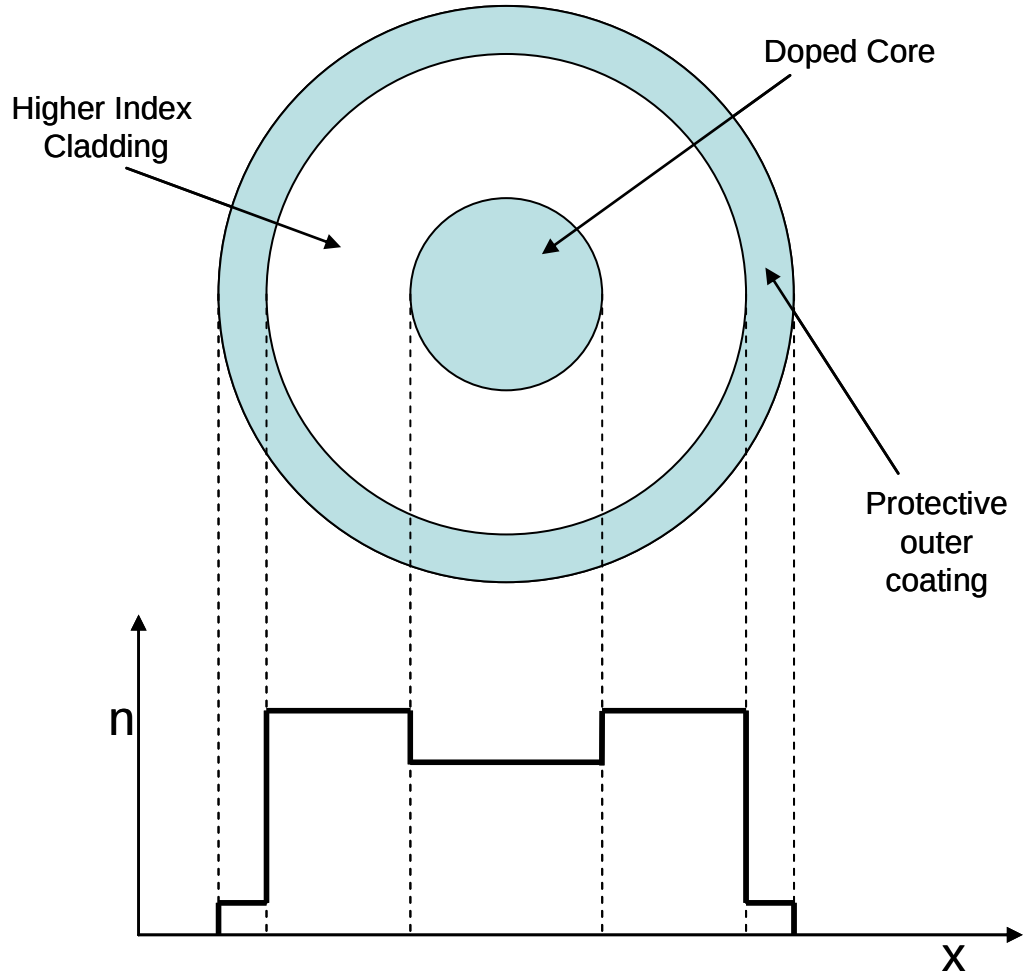

Figure 6 - Cross section of GG IAG fiber and plot of radial refractive index

At present, the primary limiting factor in pushing GG IAG fibers into the high power regime is the development of higher efficiency, length scalable pump schemes. The development and operating theory of these fibers will be discussed in the following section.

The Development of Gain Guided, Index Anti-Guided Fiber Lasers

The subject of propagating modes in gain guided fibers was initially broached in a paper by Anthony Siegman in 2003 [39]. In this paper, he looked at a wide array of gain and index profiles in fiber and slab waveguides. Of particular interest was the possibility of a very large core, single (LP_{01}) mode, fiber oscillator or amplifier with gain in the core but an anti-guided step index (i.e. the refractive index of the core being less than the refractive index of the cladding). While the calculations showed this to be possible, the initial indications were that a very small difference between core and cladding refractive indices (of less than 1e-4) was required. The difficulty of creating a fiber with completely consistent index difference of this small a magnitude initially prevented any experimental demonstration of large mode area fibers using this technique.

A breakthrough came in 2006 when laser action in a gain guided index anti-guided fiber was first demonstrated in an experiment by Chen et. al. [40, 6]. In this experiment, a fiber laser was created utilizing a 100 μm diameter core of Kigre Q100 glass (doped with 10% Nd^{3+}) and 250 μm diameter phosphate glass cladding. The index step of the fiber was 4.5×10^{-3} (1.5689 for core glass and 1.5734 for clad glass at 590 nm) or almost two orders of magnitude greater than

what was thought to be viable in Siegman's original paper. The fiber was pumped with a diffuse reflection, close coupled flashlamp pumped cavity while being held within a capillary tube. A high reflectivity mirror was placed at one end of the fiber and the partial reflectivity due to Fresnel reflection at the opposite end of the fiber was utilized as an output coupler.

With this experimental result, Siegman re-addressed the theory of gain-guided, index-antiguided (GG IAG) fibers in a 2007 paper [41]. This paper noted the fact that for anti-guided index steps, the primary guiding mechanism is grazing incidence reflection at the core-clad interface, with gain guiding slightly altering the mode, creating a truly confined propagating mode in the core and surrounding cladding when the gain in the fiber reaches a threshold level. The propagating modes in a GG IAG fiber can be easily characterized by $\tilde{V}^2$, a complex valued analog to the square of the traditional V parameter used in conventional step index fibers (1). This $\tilde{V}^2$ can be broken into its real and imaginary parts, ΔN and G, as shown below.

(4) $$\tilde{V}^2 \equiv \Delta N + jG$$

(5) $$\Delta N \equiv \left(\frac{2\pi a}{\lambda}\right)^2 \times 2n_0 \times \Delta n$$

(6) $$G \equiv \left(\frac{2\pi a}{\lambda}\right)^2 \times \left(\frac{n_0 \lambda}{2\pi}\right) \times g$$

In these equations, a is the radius of the fiber core, g is the power gain coefficient of the core with respect to the cladding, Δn is the index step at the core-clad interface, n_0 is the average of the core and clad indices of refraction, and λ is the vacuum wavelength of the propagating light.

The allowed modes in the fiber can then be plotted versus ΔN and G in the complex V^2 plane. A plot showing the LP_{01} and LP_{11} modes taken from [41] is shown in Figure 7.

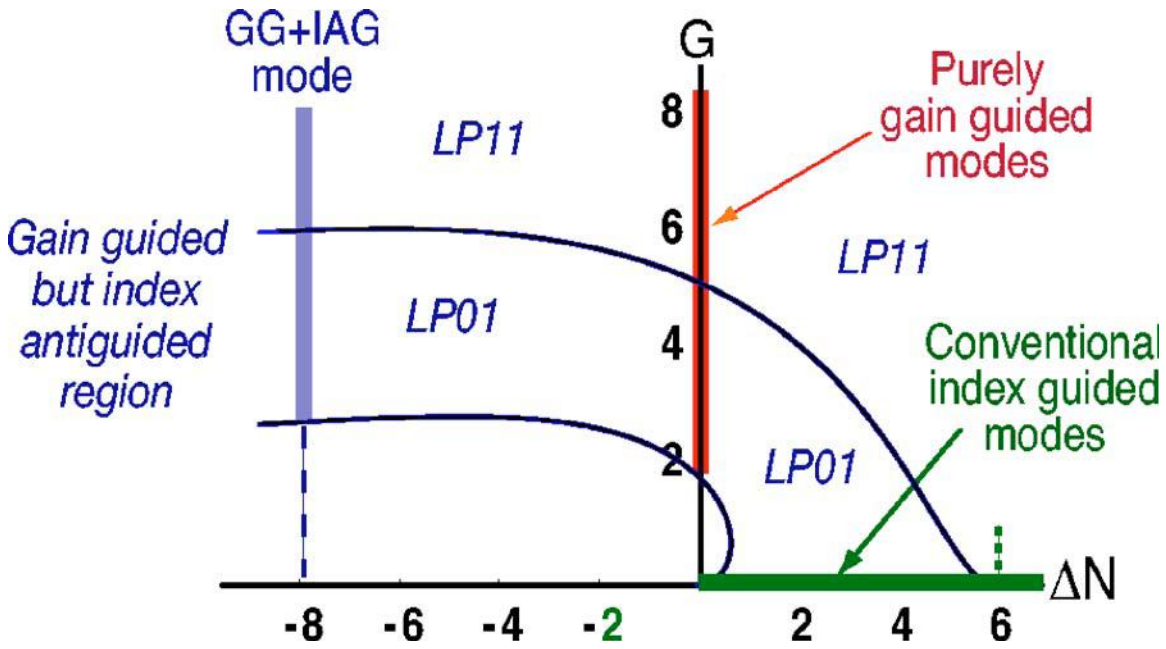

Figure 7 - Plot used with permission from [6] showing how the LP01 and LP11 modes can exist in fibers containing purely index guiding, purely gain guiding, or GG IAG configurations.

As can be seen in Figure 7, for a GG IAG configuration the LP_{01} mode will not exist until the gain in the core reaches an initial threshold G_{01} and will then exist by itself until a second gain threshold G_{11} is reached where the LP_{11} mode becomes allowed. In [41] Siegman shows that for large index difference parameters ($-\Delta N>50$), the G_{01} and G_{11} threshold can be estimated as shown in equations (7) and (8) below.

(7) $$G_{01} \cong \sqrt{\frac{4 j_{01}^4}{-\Delta N}} \cong \sqrt{\frac{133.8}{-\Delta N}}$$

(8) $$G_{11} \cong \sqrt{\frac{4 j_{11}^4}{-\Delta N}} \cong \sqrt{\frac{862.2}{-\Delta N}}$$

This updated theory was immediately validated with coincident experimental work by Chen et. al. [7], where single-mode lasing was demonstrated in index anti-guided fibers with Nd^{3+} doped core diameters of 100, 200, 300 and 400 μm. This paper also illuminated two major requirements for establishing the LP_{01} mode oscillation. The first requirement is that the threshold gain for laser oscillation be greater than the threshold gain for the establishment of the LP_{01} mode in the fiber.

(9) $$g_{th}^{osc} > g_{gg}^{01}$$

Here, g_{th}^{osc} is the threshold power gain per unit length for laser oscillation, which is given by:

(10) $$g_{th}^{osc} = -\frac{1}{2l_g}\ln(R_1 R_2) + \alpha$$

where α is the loss in the resonator, R_1 and R_2 are the resonator mirror reflectivities, and l_g is the gain length of the active laser medium. The quantity g_{gg}^{01} can be determined for large vales of negative ΔN by combining equations (6) and (7) resulting in (11) below.

(11) $$g_{gg}^{01} = \sqrt{\frac{133.8}{2n_0^3(-\Delta n)}}\frac{\lambda^2}{(2\pi)^2 a^3}$$

For a given optical fiber geometry and operating wavelength, the values of n_0, Δn, a, λ, α, and l_g are set and the resonator mirror reflectivities are the only variables that can be manipulated to

meet the criteria set in (9). Thus, if the net reflectivity is too high, the laser will reach oscillation threshold before the gain threshold for the gain guided LP_{01} mode, resulting in the multimode oscillation of parasitic modes [7].

The second requirement in addition to (9) is that the laser reach threshold oscillation before the creation of an allowed LP_{11} mode in the gain guided fiber. At a gain per unit length equal to g_{gg}^{01}, there is lossless propagation of the LP_{01} mode. In order for laser oscillation of the LP_{01} mode to become possible, the gain must be increased to an amount g_{th}^{osc} above the g_{gg}^{01} threshold. Thus, the following inequality must be maintained:

$$g_{th}^{osc} + g_{gg}^{01} < g_{gg}^{11} \tag{12}$$

By combining the restriction of (12) with (9) the following inequalities must be met.

$$2g_{gg}^{01} < g_{tot}^{osc} < g_{gg}^{11} \tag{13}$$

$$g_{gg}^{01} < g_{th}^{osc} < (g_{gg}^{11} - g_{gg}^{10}) \tag{14}$$

Here, the term g_{tot}^{osc} designates the total gain per unit length in the fiber at onset of laser oscillation. Equation (14) sets an upper and lower limit on the threshold gain of the laser, and by extension sets an upper and lower limit on the mirror reflectivities that can be used in the system in order to produce single mode, LP_{01} output. Thus, for a given fiber geometry and anti-guided index step, utilization of the proper end mirror reflectivity will result in single mode lasing.

With the demonstration of extremely large mode area fiber lasers, attention then turned to establishing a method of diode pumping the GG IAG fiber. The early GG IAG fiber experiments [40, 6, 7] were conducted with the use of flashlamp pumping of the fiber. Figure 8, taken with permission from [6], shows a sketch of the GG IAG fiber experiment and the use of a flashlamp with close coupled diffusive pump cavity.

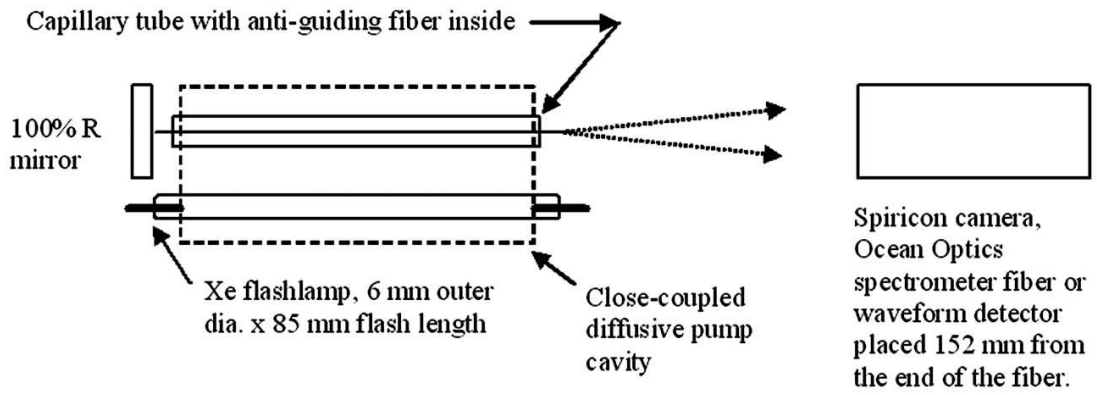

Figure 8 - Sketch of initial demonstration of GG IAG single mode experiment taken from [6]. In this experiment, the Fresnel reflection of the core glass was used as an output coupler. Later experiments involving larger core diameters used external dielectric mirrors to provide proper reflectivity for single mode operation.

While the use of a flashlamp pump source worked well to demonstrate the concept of obtaining single mode operation with extremely large mode areas, the technique is not useful for applications other than proof of concept experiments in the laboratory. The flashlamp pump is highly inefficient due to the small ratio of fiber core to flashlamp diameter and the technique is not generally extendable to longer fiber lengths and higher output powers.

In 2008, a paper by Sudesh et al [42] was published describing the first diode pumped, gain-guided, index-antiguided single mode fiber laser. Figure 9 contains a sketch (taken from [42]) of the experimental setup used to demonstrate the diode end pumped GG IAG laser. A 2.6 cm long fiber with 200 μm diameter, 1% Nd^{3+} doped Q100 phosphate glass core and 340 μm diameter cladding was end pumped from a fiber coupled diode source emitting at 803 nm. The core and cladding indices of refraction were 1.5689 and 1.5734, respectively. The fiber was placed in a 0.5 mm deep V groove machined in a water-cooled aluminum plate, which was then filled with a thermally conductive paste. The pump light was coupled into the end of the optical fiber through aspheric lenses to produce a 400 μm diameter illumination spot on the face of the GG IAG fiber. The resonant cavity was created through the use of a dichroic end mirror (HR at 1 μm and AR at 800 nm) butt coupled to the pump end of the fiber and a 98% reflectivity output coupler (at 1 μm) within 1 mm of the output end of the fiber.

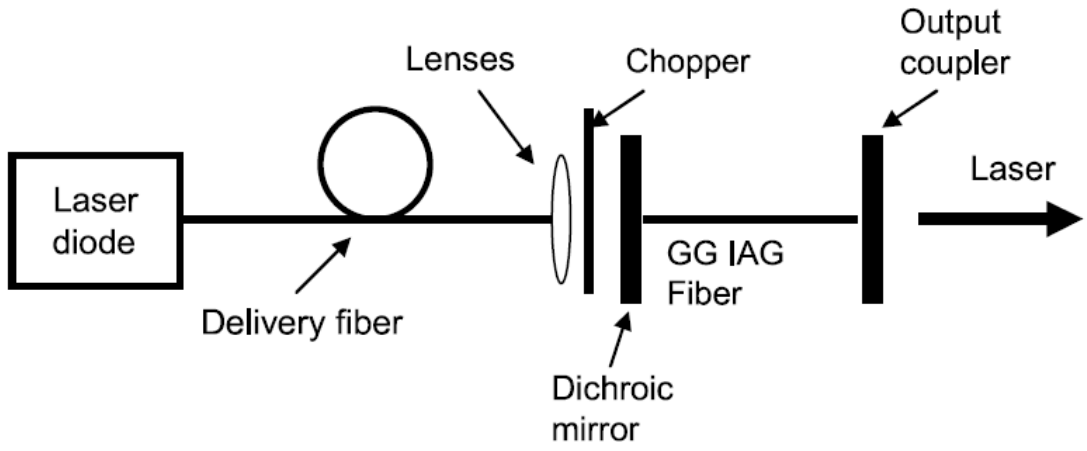

Figure 9 - Sketch of experimental setup showing diode end pumped GG IAG fiber from [42]

The diode end pumped fiber produced an output beam with high beam quality (M^2 of 1.2-1.5) but low efficiency (slope efficiency of 1.5% before rolling off at high pump powers due to thermal effects and a maximum optical to optical efficiency of only 0.8%). This low efficiency was due to the index anti-guiding effect of the core-clad refractive index step. In traditional end pumped fibers, pump light injected into the cladding would couple into the core along the length of the fiber resulting in high pump efficiency. However, with an index anti-guided fiber the majority of pump light injected into the cladding remains confined to the cladding due to total internal reflection at the core-clad interface. Additionally, a significant portion of light that is pumped directly into the core is quickly refracted into the cladding where it also remains confined.

Beyond these experimental results, a series of recent papers have looked at theoretical models to predict the effects of fiber curvature and bending on the field distribution and loss in a GG IAG fiber [43], the potential for a GG IAG fiber utilizing parabolic index distribution [44], the feasibility of ytterbium doped GG IAG fibers as amplifiers [45], and the potential use of GG IAG fibers as directional fiber couplers [46]. While experimental implementation of these concepts has not been undertaken, they show the potential for the use of the GG IAG concept in other applications and fiber geometries.

Pump Requirements for GG IAG fibers

In order to obtain power scaling with GG IAG fiber lasers, a new pump method must be developed. Any method used must meet three main criteria. First, the pump efficiency must be

reasonably high (>50%) with the capability of delivering very high total pump power in order to make high power applications a possibility. Any high energy system is driven primarily by a need for efficiency, through maximizing the direct optical to optical efficiency of the laser, minimization of absorbed pump light that is converted to waste heat in the gain medium, and reduction of pump light that is unabsorbed by the gain medium that eventually heats other physical components of the laser system. In short, the total absorbed power from pumping must be capable of meeting (through combination of high pump efficiency and high overall pump power) the demands placed on it in a high power system.

Second, the pump method must be capable of pumping the antiguided core relatively uniformly along the length of the fiber. As discussed in the previous section, equation (13), the gain per unit length of the active core must be greater than twice the gain threshold for the onset of single mode propagation in the fiber, but less than the gain needed for the onset of the first higher order mode. Since the gain component of $\tilde{V}^2$, G, is directly proportional to the gain per unit length, which is in turn directly proportional to the inversion and hence absorbed pump power, a calculation can be quickly done to determine the percentage variation in absorbed pump power that can be tolerated in the fiber while maintaining lowest order mode oscillation.

$$\frac{G_{11} - 2G_{01}}{G_{11}} = \frac{\sqrt{\frac{862.2}{-\Delta N}} - 2\sqrt{\frac{133.8}{-\Delta N}}}{\sqrt{\frac{862.2}{-\Delta N}}} = \frac{\sqrt{862.2} - \sqrt{535.2}}{\sqrt{862.2}} = 21\% \tag{15}$$

Thus, the total variation in absorbed pump power cannot vary by more than 21% without serious detriment to the single mode nature of the fiber laser output beam.

Third, the pump technology must be capable of being scaled to fiber lengths long enough to meet whatever requirement is set by the fiber geometry, refractive indices, and obtainable reflectivities. Figure 10 is a plot of fiber lengths calculated to provide single mode output for various fiber core diameters, assuming Δn of -0.0045 from previous experiment, and an output coupler reflectivity of 90% which would provide efficient CW operation.

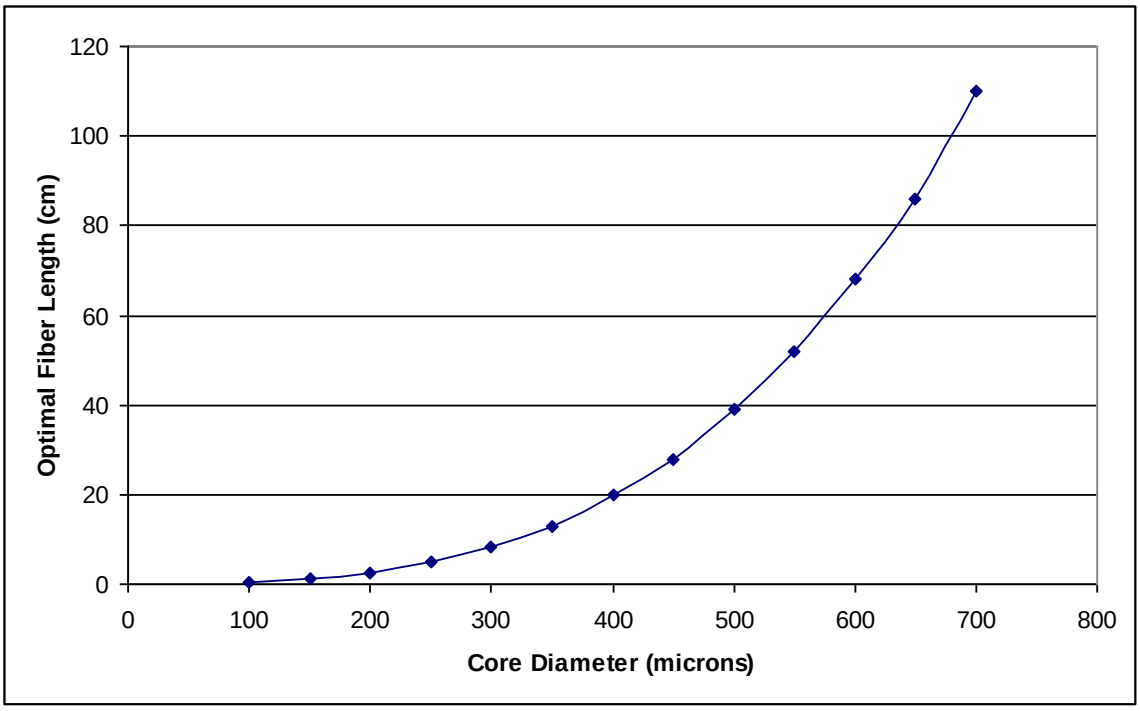

Figure 10 - Calculated optimal GG IAG fiber lengths that would result in single mode operation with a 90% R output coupler and HR end mirror for various fiber core sizes. Calculations assume delta n of 4.5 x 10^{-3} and alpha = 0.

As seen in Figure 10, the optimal fiber length increases with increasing core size, such that once core sizes reach 400 μm, the fiber length has increased to over 20 cm. This indicates that a pump technology created for GG IAG fibers must deliver pump energy with only 21% total variation over lengths on the order of up to half a meter.

Looking at the three basic pump requirements of high power/efficiency, uniformity, and the capability to meet fiber lengths of up to 0.5 m, it is then possible to assess the two previously used pump technologies against these requirements. Flashlamp pumping does not meet the efficiency requirement, but does provide good uniformity of pump distribution along the length of the fiber, thus making it a good pump mechanism for the initial proof of concept experiments that were performed by Chen et. al. [6, 7]. The flashlamp pump technology could conceivably pump fiber lengths of up to 0.5 meters but would be incredibly unwieldy and inefficient.

Diode end pumping of the fiber core, in a manner similar to Sudesh et al. [42] could have the potential for acceptable pump efficiency if the pump mode could be highly tailored to match the core size with a very low numerical aperture focusing system. However, the maximum length of fiber that can be pumped with the required uniformity is limited by the characteristic absorption length, $1/\alpha$, of the doped core. For a 1% Nd^{3+} doped, Kigre Q100, phosphate glass core as used in [42], the absorption length is 0.36 cm. Using Beer's law for absorption, the profile of absorbed power along the length of the fiber can be calculated for an end pumped fiber and the results are shown in Figure 11 below.

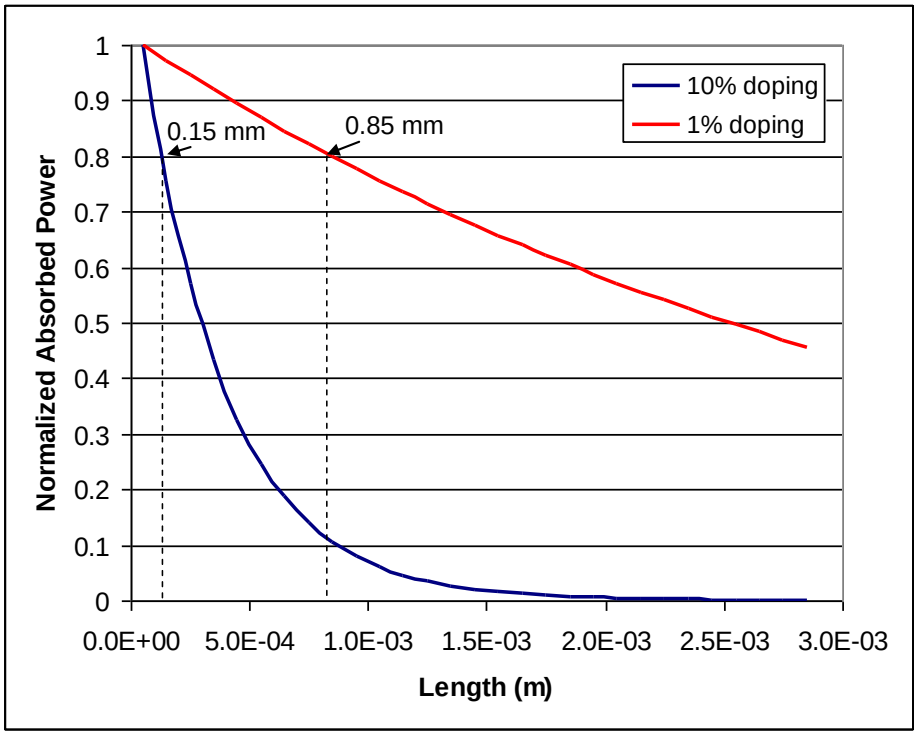

Figure 11 – Calculated normalized absorbed pump power along the rod axis for 1% and 10% Nd^{3+} doping. It can be seen that to maintain only a 20% variation in gain induced pump, the pump length cannot be increased more than roughly 1 mm even for 1% doping.

Figure 11 shows that the short absorption lengths will prevent the effective end pumping of GG IAG fibers of any considerable length if there is no pump leakage from the cladding into the core that would normally extend the pump length of double clad fibers. For this reason, direct end pumping of a GG IAG fiber without other modification is not capable of pumping the fiber lengths needed for efficient operation of a high power GG IAG fiber.

Alternate Pump Methods

Since flashlamp pumping and direct diode end pumping are not suitable technologies for pumping high power GG IAG fibers, new methods must be considered. The first of these is the concept of the index crossover fiber; the second is side pumping.

Index Crossover Pump Technique

The concept of index crossover [88] is based upon the use of a fiber with low dispersion cladding and higher dispersion core. If the dispersions of the glasses are properly chosen, it would be possible to have a core index higher than the cladding index at pump wavelengths, while having the core index lower than the surrounding cladding index at the longer wavelength of laser operation. This would make a GG IAG fiber at the laser wavelength, and a standard step index fiber at pump wavelength.

Due to the conventional relative refractive indices at pump wavelength, the fiber would then be capable of being pumped through standard double clad pumping discussed in a previous section. The double clad pump technique has proven to be highly efficient and effective for fibers of many meters in length, while maintaining a very uniform pump profile [15,47-49], making it an ideal fit for pumping GG IAG fibers if the index crossover can be realized.

The first step to creating an index crossover pumped GG IAG fiber is the identification of glasses that exhibit index crossover at a wavelength somewhere between the pump and laser wavelengths. Unfortunately, dedicated laser glasses such as Q100 (Kigre inc.) and LG760

(Schott) are purposefully designed to be low dispersion glasses. Since normal dispersion results in a decrease in refractive index at longer wavelengths, a fiber exhibiting a core index greater than the cladding index at short wavelengths and a core index less than the cladding index at long wavelengths must have a core glass with higher dispersion than the cladding glass. This makes the prospect of finding a crossover cladding compatible with existing laser glasses very problematic. This phenomenon is evident in selected pairs of non-laser glasses taken from the Schott catalog and shown in Figures 12 and 13. Figure 12 shows the individual refractive indices of the glasses and the cross over of the dispersion curves of the glasses. Figure 13 shows the calculated delta n between the two fibers across the span of wavelengths of interest for a Nd^{3+} doped core.

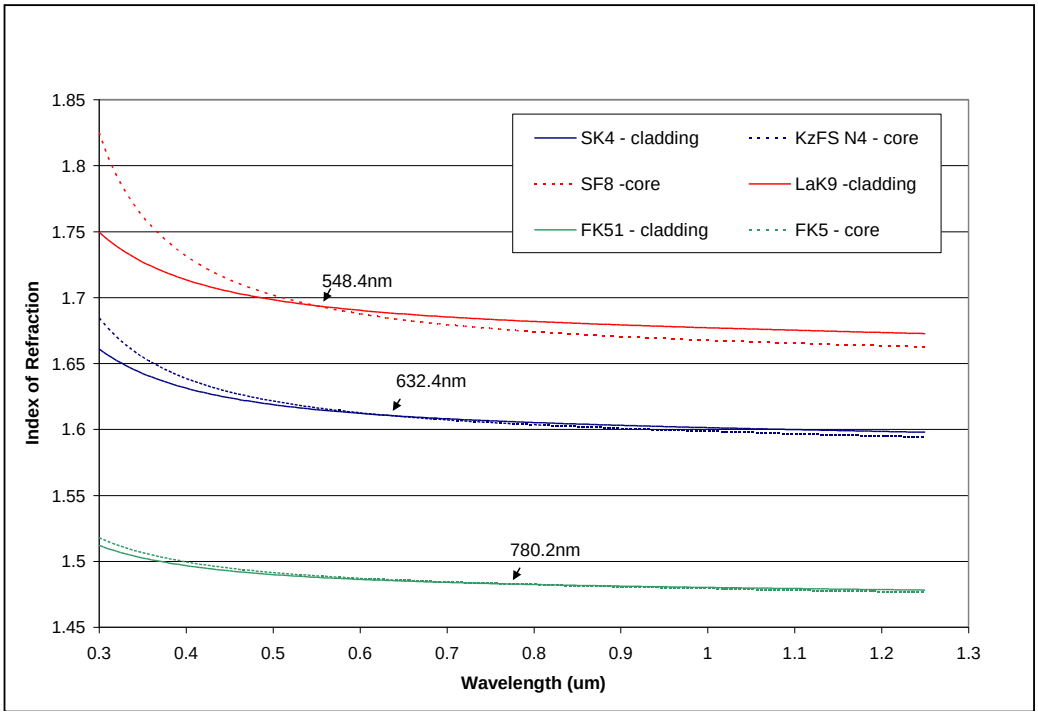

Figure 12 - The dispersive crossover of three pairs of Schott glasses (KzFS N4/SK4, SF8/Lak9, and FK51/FK5). These glass pairs exhibit a low dispersion clad glass and higher dispersion core glass.

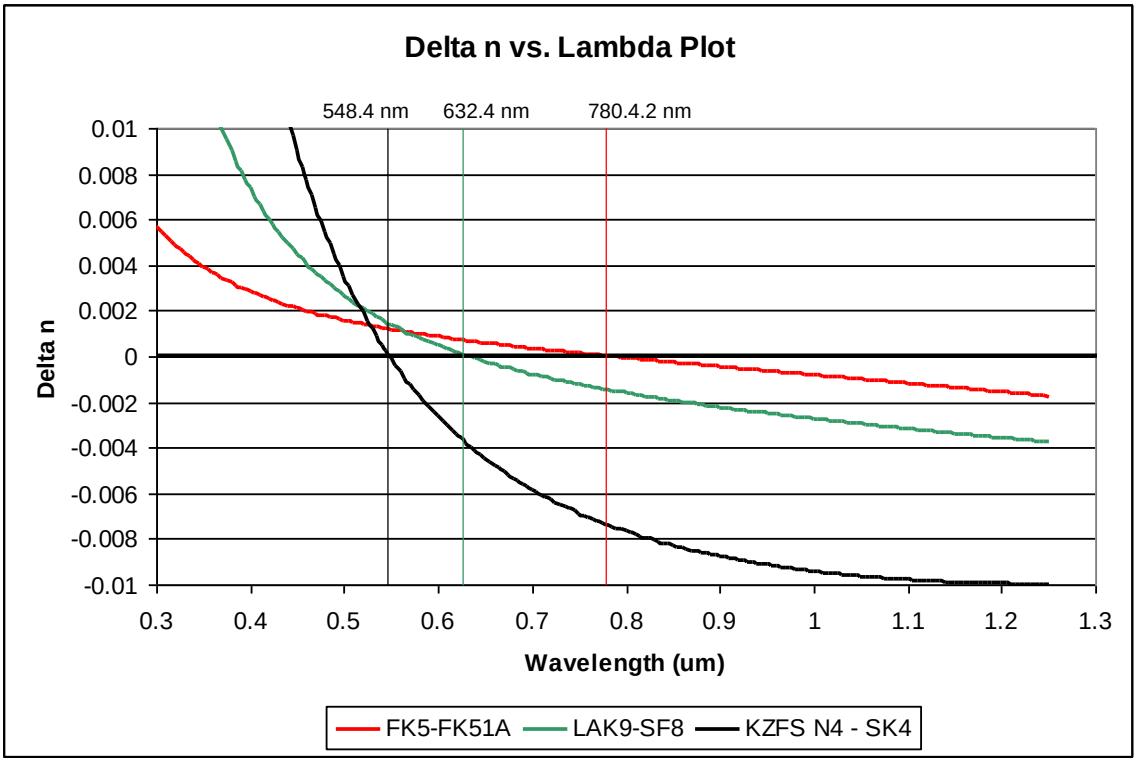

Figure 13 - Delta n for the same three pairs of Schott glasses seen in Figure 12. Previous GG IAG experiments were done with delta n = -0.0045.

As shown in figures 12 and 13, the cross over points for these glasses are all below the 800 nm pump band for Nd^{3+}. However, Nd^{3+} does have pump bands at shorter wavelengths. A typical Nd^{3+} absorption spectrum is shown in Figure 14, exhibiting pump bands at 600 nm and 530 nm that could be used to take advantage of the index crossover exhibited in the three previously mentioned Schott glasses.

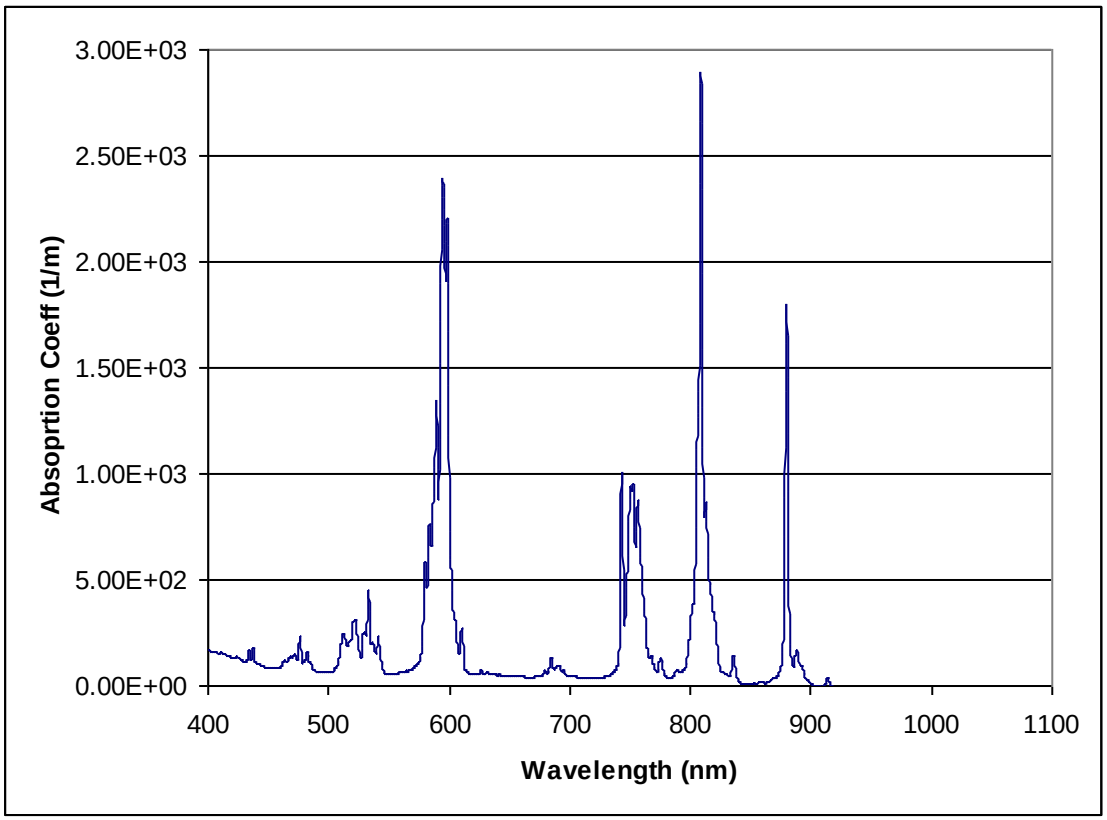

Figure 14 - Nd $^{3+}$ absorption coefficient in 1% doped Nd:$YV0_4$ (used to show absorption typical of Nd $^{3+}$). This plot shows pump bands at 600nm and 530nm, which could be utilized to take advantage of index crossover pumping.

Unfortunately, these glasses are not presently doped with Nd $^{3+}$ ions and a great deal of developmental work would need to be completed in order to determine if they could be made into viable laser materials. One important component of this would be to measure how doping of the core glass would effect its refractive index. To this end, theoretical calculations were made using the Kramers-Kronig relationships represented in the following integrals [50].

$$n(\omega) = 1 + \frac{1}{\pi} P \int_{-\infty}^{+\infty} \frac{\kappa(\omega')}{\omega' - \omega} d\omega' \qquad (16)$$

(17) $$\kappa(\omega) = -\frac{1}{\pi} P \int_{-\infty}^{+\infty} \frac{n(\omega') - 1}{\omega' - \omega} d\omega'$$

In these equations, *n* and κ are the real and imaginary components of the complex refractive index, ω is the angular frequency of light, and P refers to the Cauchy principal value of the integral. The linking of *n* and κ means that through equation (16) the real index of refraction of a material can be calculated from a measurement of the material's absorption spectrum.

Using the absorption spectrum shown in Figure 14, equation (16) was numerically evaluated and the variation in refractive index determined. This index variation over the range of the absorption measurement was then summed with the undoped index of the glass. Figure 15 shows the resulting index difference created by 1% Nd doping and Figure 16 shows how doping of the core glass would effect the Δn curve of a fiber made of FK5 and FK51A glass.

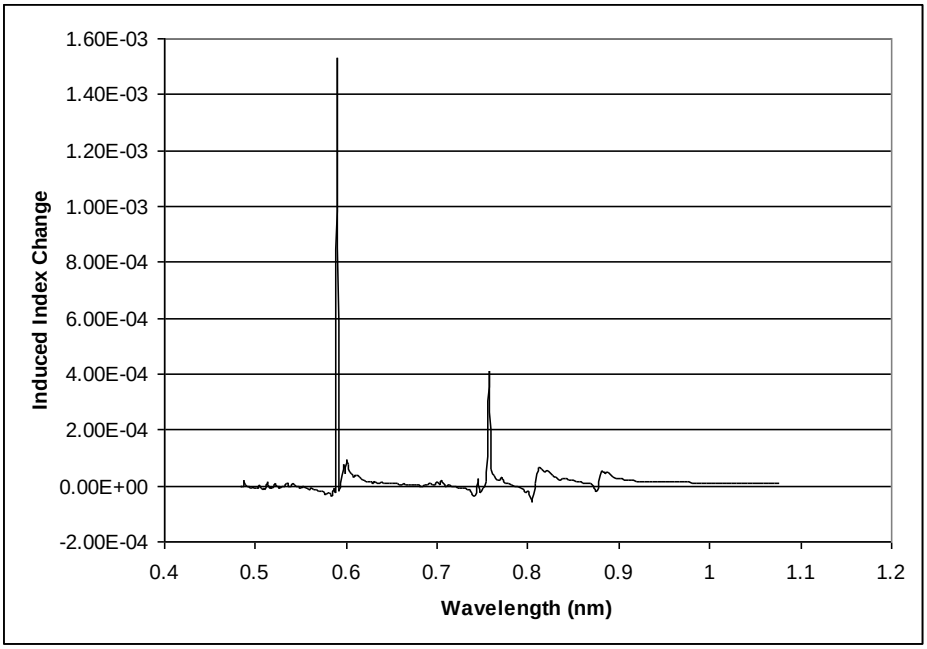

Figure 15 - Calculation of the induced refractive index change due to 1% Nd $^{3+}$ doping

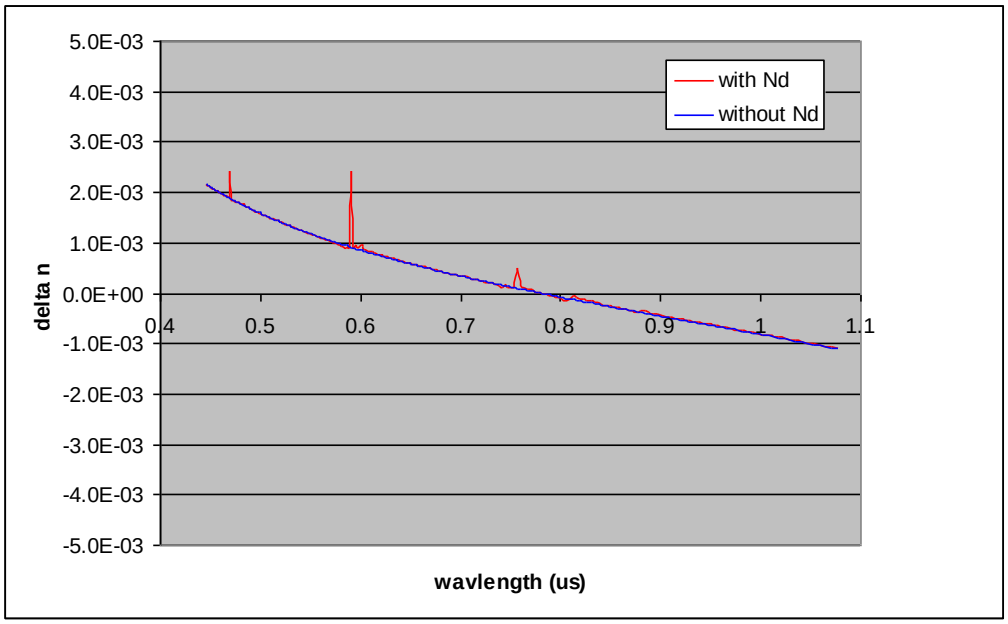

Figure 16 - Calculated delta n for a FK5/FK51A GG IAG fiber with 1% Nd doped core

Of interest is the result that occurs with higher doping concentrations. If the doping concentration is raised to 10% Nd $^{3+}$ then the induced index change begins to create a region of positive delta n at wavelengths slightly above the center of the 800 nm resonance. The delta n curve for 10% doping is shown in Figure 17.

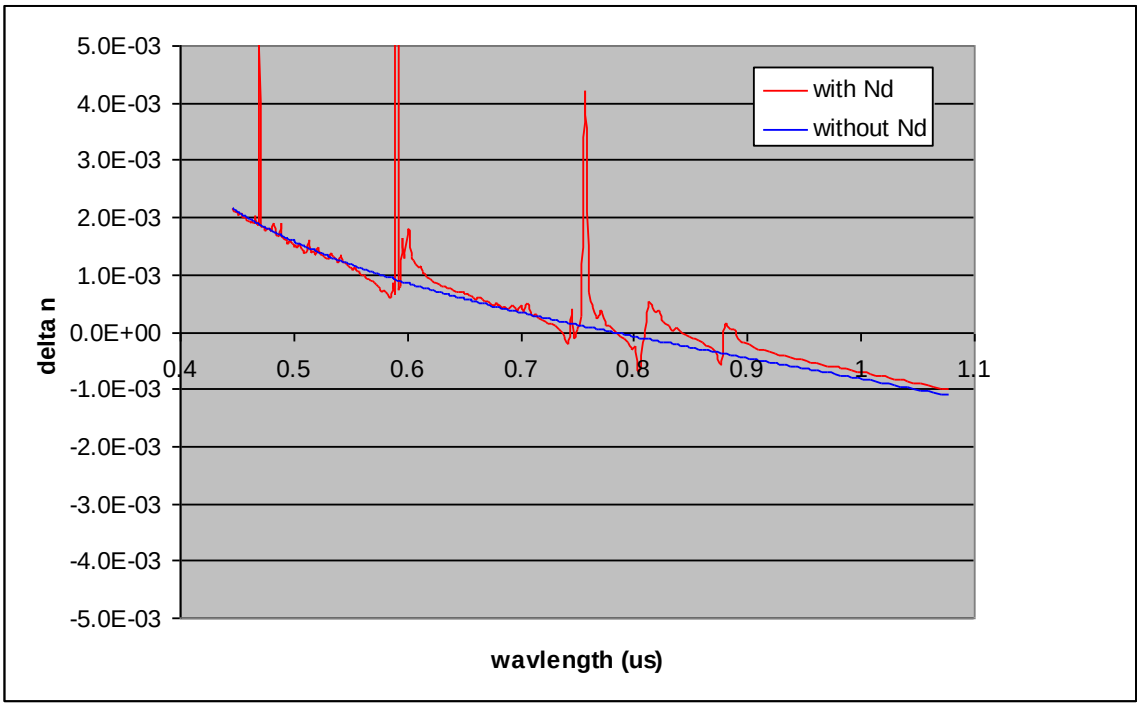

Figure 17 - Calculated delta n for a FK5/FK51A GG IAG fiber with 10% Nd doped core

Pumping at wavelengths slightly longer than the central absorption peak of the 800 nm pump band in a FK5/FK51A fiber could allow for index crossover pumping without having to resort to shorter wavelength pump bands and the resultant increase in quantum defect.

While the index crossover pump technique is potentially very useful, it needs a good deal of investment in time and resources to make it viable. Glasses that show promise with dispersive properties that yield crossover at a useful wavelength have not yet been shown to be viable host

materials for laser dopant ions. In addition, there are a number of mechanical issues in creating a fiber. These glasses are not proven to be drawable into a fiber, and could have significant mechanical issues when drawn together in a fiber (should it be made) due to difference in their rates thermal of expansion. The calculations in this section show crossover to be highly desirable for GG IAG applications but implementation is beyond the scope of this research.

Side Pumping of GG IAG Fibers

Due to the difficulties of end-pumping GG IAG fibers, one potential avenue to avoid the problems presented by the anti-guided index of the fiber is to pursue direct side pumping of the fiber. Linear diode laser bars are a well developed technology and are sold by several companies in a wide variety of wavelength's and output powers. The linear nature of these sources and the availability of linear arrays of multiple bars (developed for side pumping of bulk, solid state laser rods) make them an attractive pump source for a small linear gain medium such as a GG IAG fiber.

As stated in the previous section on pump requirements for GG IAG fibers, there are three main requirements that a side pumped technology must meet. First, a method must be devised to focus the pump light from the linear diode bars into the fiber to achieve maximum pump efficiency. The fiber available to us for testing the side-pumped concept was a GG IAG fiber with Kigre Q100 phosphate glass core doped with 10% wt. Nd^{3+}. The fiber core was 100 μm in diameter with refractive index of 1.5689 and the total cladding diameter was 250 μm with a cladding refractive index of 1.5734 for a total index step difference of -0.0045. A great deal of

alignment sensitivity is needed to keep the linear pump bars aligned to the fiber core along the entire length of the fiber. Keeping the diodes aligned to the fiber to within half the radius of the core (25 μm) over the length of a 4 cm fiber requires angular alignment of the line of pump diodes to within roughly 600 μrad of the axis of the fiber. In addition, the translational positioning of the fiber relative to the diode bars must be very precise. The 100 μm width of the fiber core coupled with the <100 μm RMS spot size of the focused pump beam requires that the beam be aligned within a few microns in order to ensure the maximum amount of pump light enters the fiber. In addition, ray trace simulation (discussed in the next section) shows the depth of focus of a 6 mm cylinder lens to be roughly 100 μm (measured as distance over which less than 10% change from the minimum RMS spot size is observed). This depth of focus requires that the vertical distance between the focusing cylinder and the fibers be held to less than 100 μm along the length of the fiber, resulting in a maximum alignment error of the beam pump axis of 2.5 mrad. These positional tolerances can be accomplished in the lab by utilizing linear and rotational translation stages with precision micrometers. Efficient pumping of such a small diameter core also requires that pump light make more than one pass through the core glass. As seen in Figure 10, the absorption length for 10% doped Q100 glass is 360 μm. This means that for the majority of pump light to be deposited in the core, the light would have to pass through the equivalent length of 4 core diameters. To accomplish this, the fiber must be held in some sort of reflective pump cavity.

The second major requirement of the side pump technology is that it produce a uniform pump distribution along the fiber length and through the fiber cross section. If linear diode bars are used as a pump source, this requirement will determine the distance that the bars will be held

from the fiber. Since standard diode bars are 1 cm in length, multiple bars must be used to pump any significant length of GG IAG fiber. However, there is a mechanical limitation as to how close diode bars can be placed next to each other in an array. Light emitted from a bar typically diverges quickly in the fast axis (roughly 40 degrees FWHM) perpendicular to the length of the bar, and a bit slower (roughly 10 degrees FWHM) in the slow axis parallel to the length of the bar. With gaps between bars, the diodes must be held far enough back from the fiber to allow the slow axis divergence of the diode beams to fill in the dead regions between diode bars. This will determine the minimum distance that the bars can be placed from the fiber.

The third requirement of the side pumped technology is that it must in theory be able to pump lengths of GG IAG fiber up to 0.5 meters. Diode manufactures, such as Northrop Grumman's Cutting Edge Optronics, already manufacture well toleranced linear diode arrays up to 12 cm in length. Several of these arrays could be ganged together to create a linear pump source that would be able to meet the length requirement of any viable GG IAG fiber. While aligning multiple pump arrays to a small fiber could be quite difficult, it is not impossible.

Proposed Fiber Side Pump Method

Taking the requirements of a side pumped system into account, the following geometry (shown in Figure 18) for a side pumped technology was proposed. First, a GG IAG fiber would be mechanically held in a V groove precision machined in a water-cooled copper block. This would keep the fiber mechanically straight and free from bending loss. The fiber would be surrounded by indium solder in the groove so that it was completely coated along its sides. The indium

would provide physical restraint of the fiber, a good thermal contact from the fiber side surface to the copper cooling block and a reflective surface surrounding the fiber to increase pump efficiency. With the fiber fully coated in indium, the entire copper block could then be polished until a flat pump window was established along the side of the fiber, allowing pump light access to the fiber.

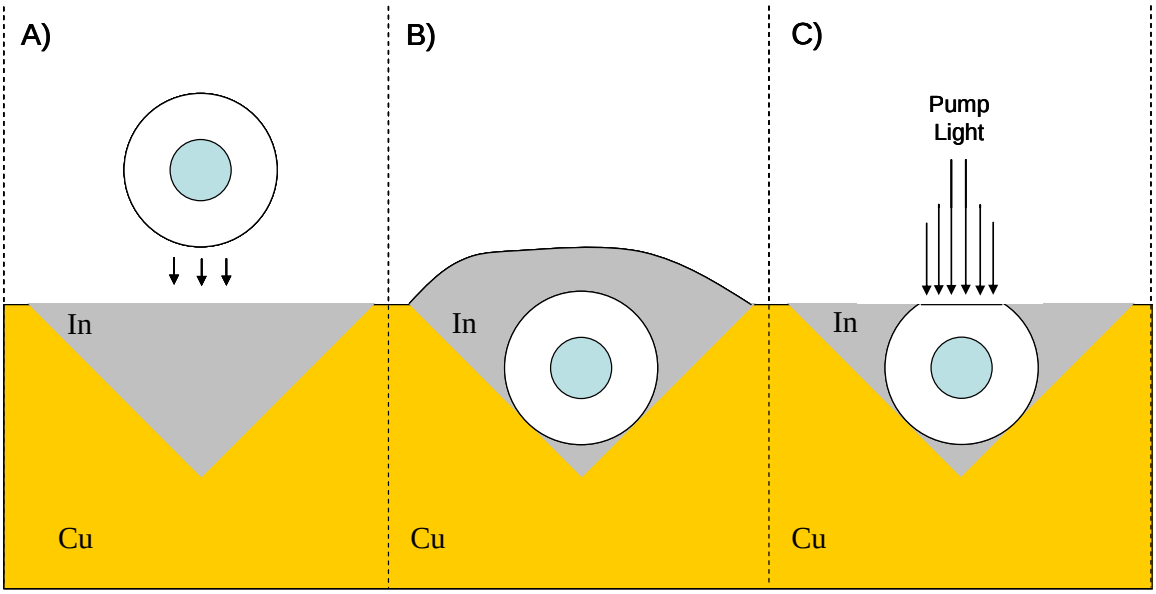

Figure 18 - Diagram of side pumped fiber concept. A) The fiber is pressed into molten indium filled copper V-groove. B) The fiber has sides completely coated with molten indium which is then allowed to solidify. C) Entire fixture is polished until fiber and indium are level with copper surface. The fiber now has a polished window for pump light to enter.

Ray Trace Modeling of Side Pump Geometry

Before creating a final design for GG IAG side pumping, a number of details needed to be worked out. Many of these issues could be addressed through ray trace modeling before beginning to fabricate the fiber for side pumping. To this end, optical ray trace modeling was

conducted using Breault Research Organization's Advanced Systems Analysis Program (ASAP) software. A model of the 100 μm core GG IAG fiber described previously, with characteristics summarized in Table 1 below, was constructed along with an optical source model for the series of linearly arranged diode bars.

Core Diameter:	100 μm
Cladding Diameter:	250 μm
Core Glass Refractive Index:	1.5689
Clad Glass Refractive Index:	1.5734
delta n:	-0.0045
doping wt% (Nd 3+):	10%
ion number density	1.14E21 cm^{-3}
absorption coef.	2.8 mm^{-1}

Table 1 - Physical and geometric parameters of GG IAG fiber

Each bar in the diode source was constructed from characteristics taken from a typical CEO diode bar shown in Table 2.

Divergence (lensed in Fast Axis):	3 degrees FWHM
Divergence (Slow Axis):	10 degrees FWHM
Emitter Size:	90 μm x 1 μm
Emitters per bar:	69
emitter pitch:	133.3 μm
bar length:	1 cm
bar to bar spacing	1.5 mm

Table 2 - Diode bar characteristics used in ray trace modeling (taken from parameters supplied by Cutting Edge Optronics)

A series of three linearly aligned diode bars were constructed as sources in ASAP with their output apodized to fit a Gaussian directionality distribution matching the fast and slow axis FWHM values reported in Table 2.

Optimal Diode Bar to Fiber Spacing

With the source and fiber created in ASAP, the first task was to find the optimal working distance of the diode bars from the GG IAG fiber. As mentioned previously, the 1.5 mm spacing between bars has the potential to leave gaps in the pump distribution along the length of the fiber. Since the diode bars have a slow axis divergence angle of 10 degrees, as the bars are pulled away from the fiber, the spread of the pump light will fill in the gaps between diode bars. A series of plots of the longitudinal pump distribution found in the fiber core as a three bar, linear diode array is placed at different distances, D, from the fiber is shown in Figure 19.

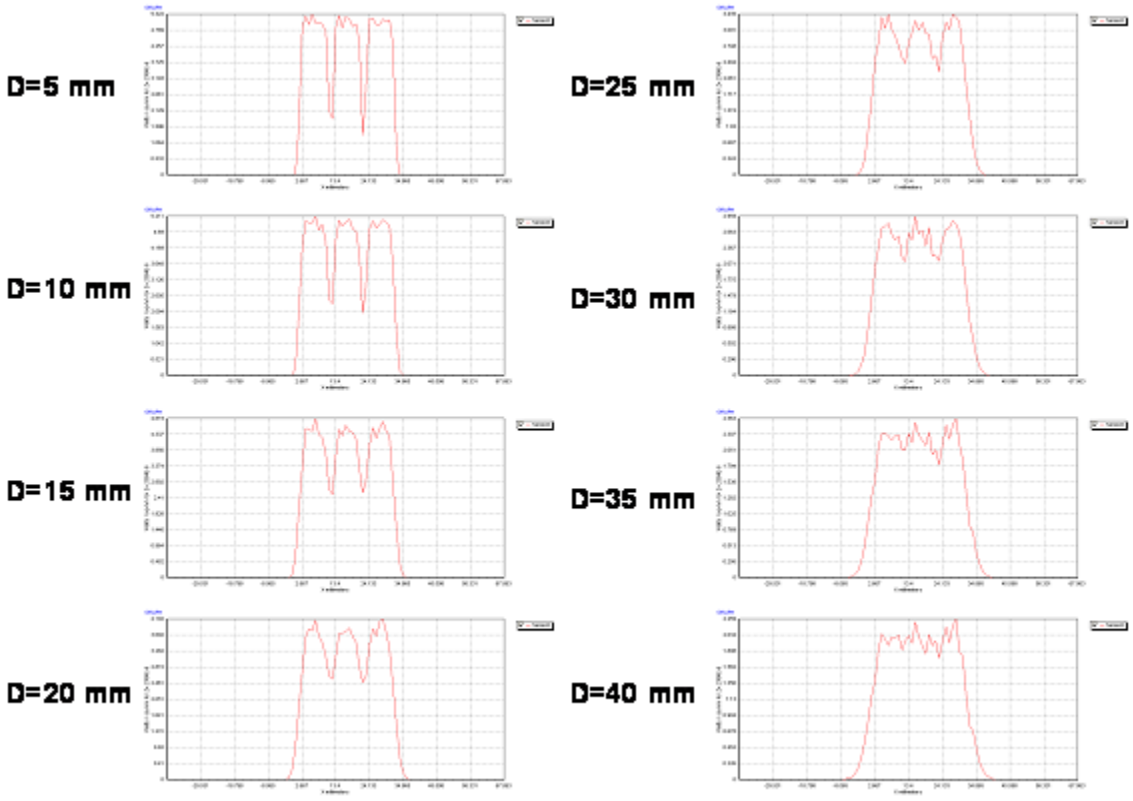

Figure 19 - Calculated absorbed pump power distribution as a function of position along the axis of the GG IAG fiber core for different distances from the diode bar source to fiber.

As the distance between the pump bars and the fiber core increases to 40 mm, the gaps between diodes fade out to the point where they are no longer distinguishable from the random noise in the simulation. This can be seen numerically in Figure 20, a plot of the maximum peak to valley ratio for each distribution versus diode distance from the fiber.

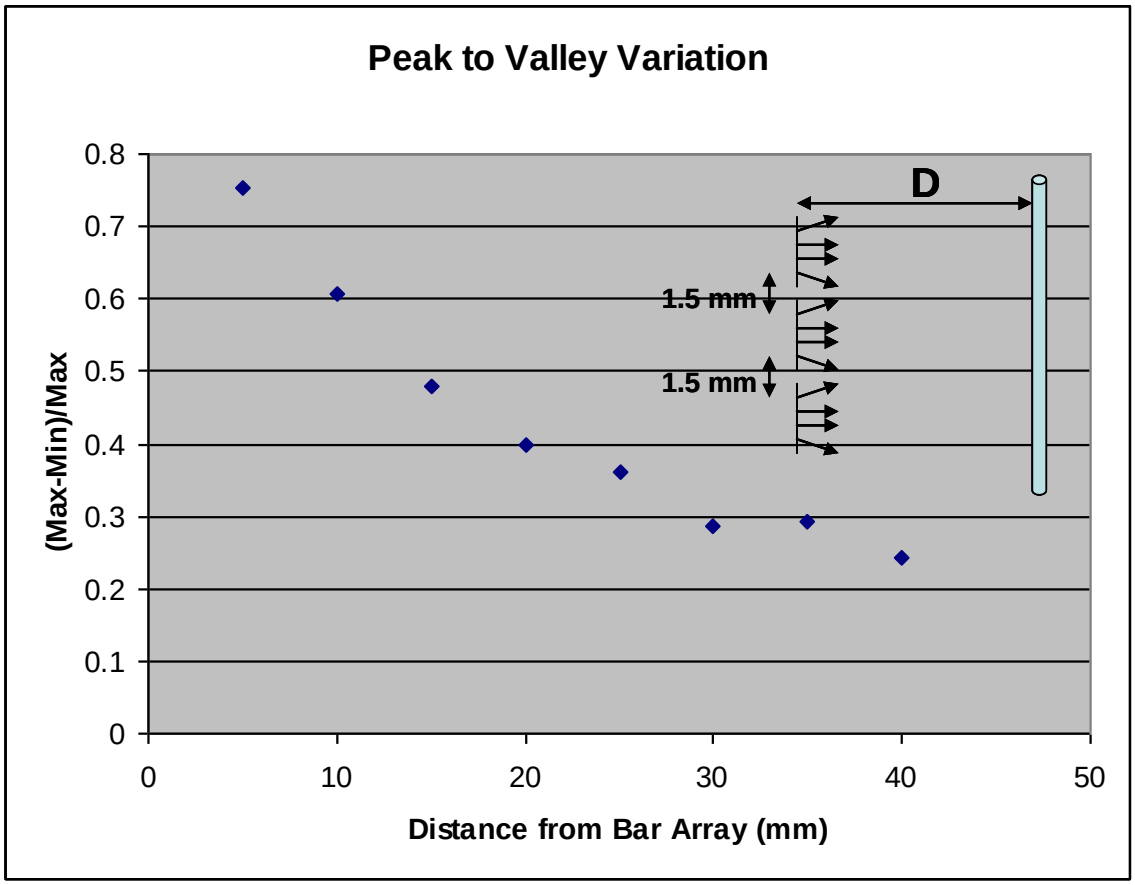

Figure 20 – Calculated peak to valley variation in the pump distribution along the axis of the GG IAG fiber core for varying diode bar source to fiber distance.

Since the gaps between diode bars are effectively smoothed out at distances greater than 40 mm, this becomes the minimum distance of the diode bars relative to the fiber in the final system design.

Optimization of Focusing Lens

Due to the diode bars being lensed in the fast axis, the divergence of the beam perpendicular to the fiber axis is small, but still very significant relative to the small size of the fiber pump

window and core diameter. Since the diode bars must be held back from the fiber in order to obtain maximum uniformity along the fiber length, an additional focusing optic must be used to focus the expanded beam into the fiber. The easiest way to accomplish the needed single axis focusing is through the use of cylindrical lens placed in an intermediate position between the pump diodes and the fiber. Raytrace visualizations of the relative geometry of the pump diode source, rod lens, and fiber are show in Figure 21.

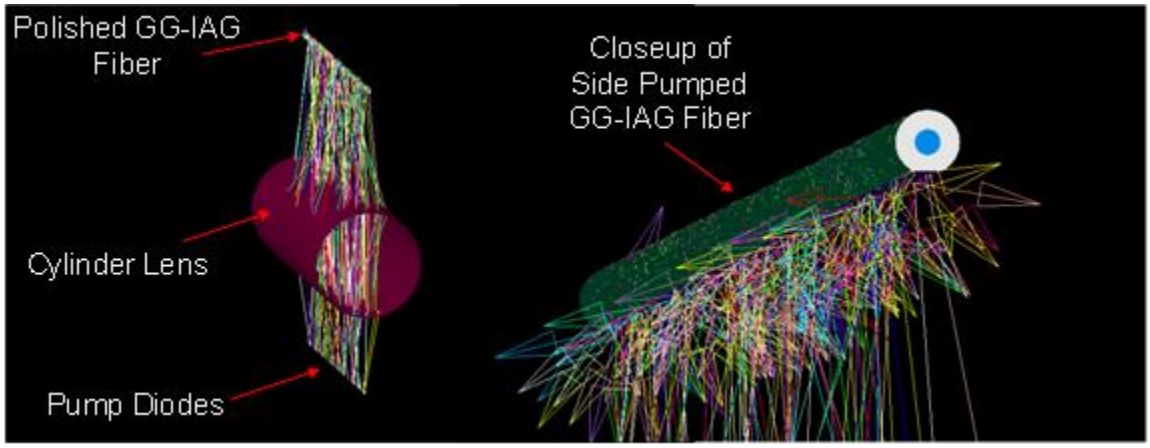

Figure 21 - 3D visualization of pump source, focusing cylinder lens, and GG IAG fiber

Ray trace simulations were run to find the optimal cylinder lens diameter for the system. As the cylinder diameter becomes larger, the effective focal length of the lens becomes longer, resulting in larger minimum spot sizes. As the cylinder becomes smaller, it begins to fail to collect more and more pump light. Additionally, the strong curvature of small diameter lenses leads to greater spherical aberration, enlarging the minimum spot size. The rms spot size of the pump beam (in the direction perpendicular to the fiber axis) is plotted in Figure 22 versus the diameter of the focusing cylinder lens. The tightest focal spot was produced by a focusing cylinder lens diameter of 6 mm.

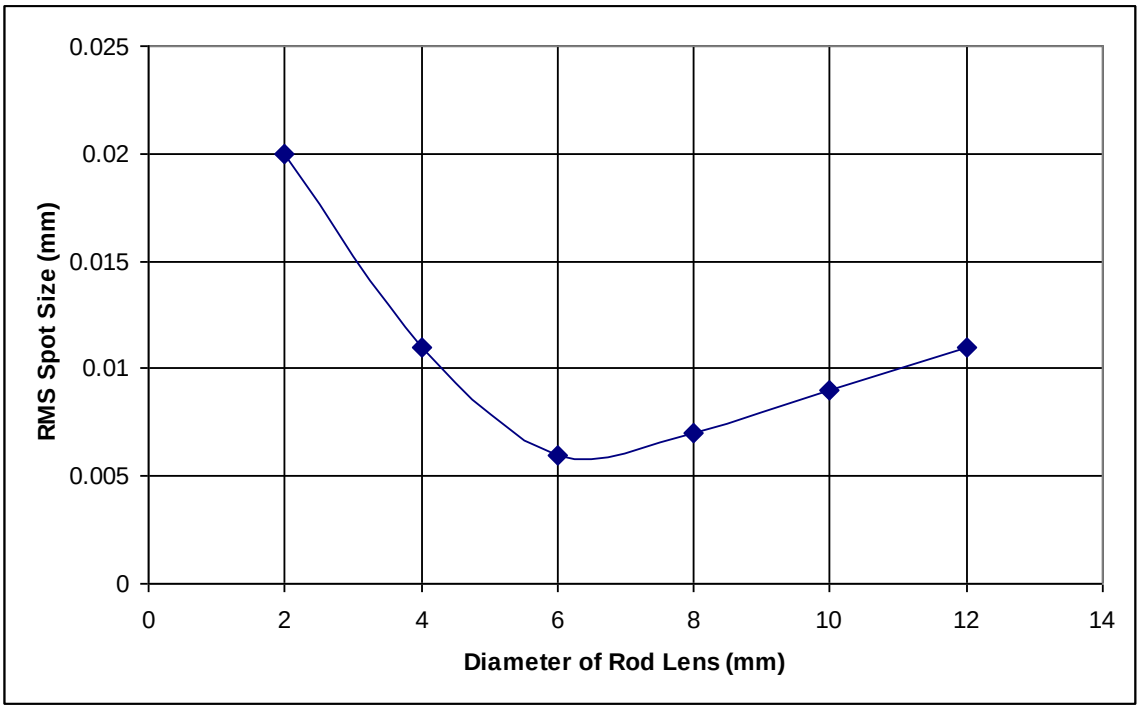

Figure 22 - Calculated RMS spot size vs. cylinder lens diameter. The minimum spot size is generated by a cylinder lens with 6 mm diameter.

Optimizing Pump Window

With the spot size of the pump beam determined, the next step was to find the corresponding optimal size of the polished side pump window on the GG IAG fiber. A window with too small an opening would prevent pump light from entering the fiber, while too large a window would allow reflected pump light to escape from the fiber without depositing maximum energy in the core. Using the 6 mm rod in the pump scheme, the side pump setup was tested with varying depths of polish, defined as the depth of material removed from the side of the fiber to form the flat pump window. The resulting plot of absorption efficiency vs. polish depth is shown in Figure 23 with an inset drawing clarifying the meaning of polish depth.

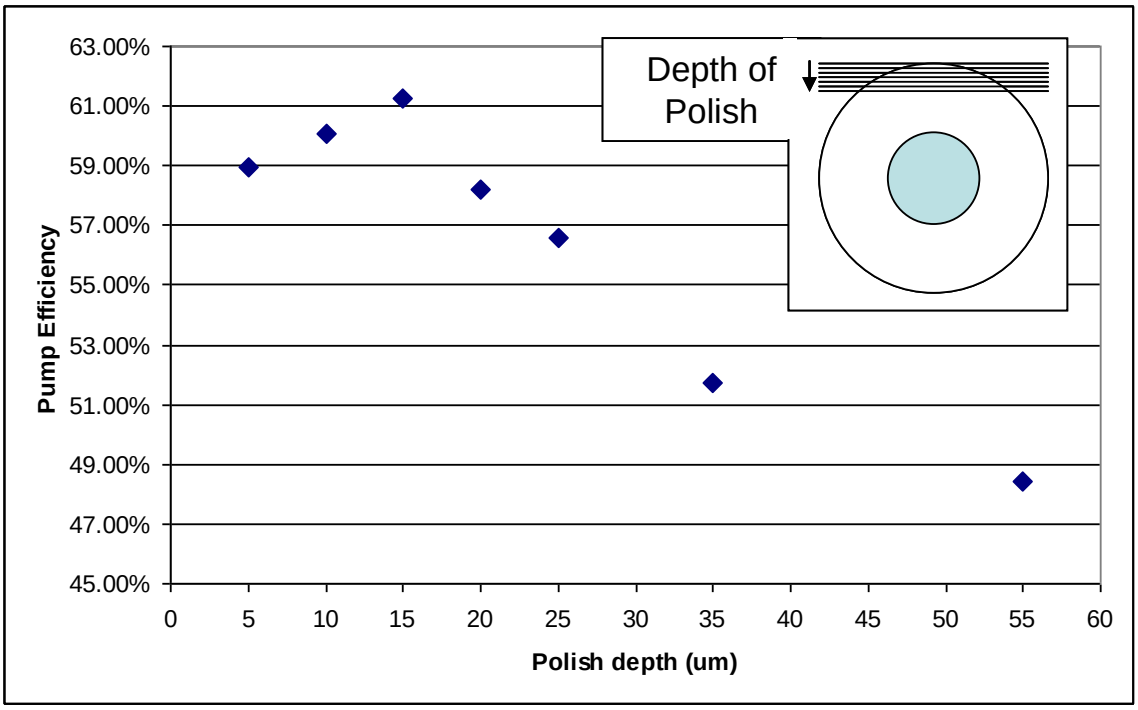

Figure 23 - Calculated pump efficiency (ratio of total pump light to absorbed pump light) versus the depth of the polished side pump window in the GG IAG fiber.

The optimal polish depth of 15 μm corresponds to a pump window opening of 120 μm, or roughly the size of the core diameter.

Cross-sectional pump uniformity

The final factor that must be evaluated using the ray trace software is the uniformity of the pump light absorption across the cross-section of the GG IAG fiber core. Small variations in the pump distribution in the core would not be likely to cause significant problems with the gain guiding process since the determining factor is the amount of gain a light ray sees along the total path between bounces at the core/clad interface. However, highly lopsided gain distributions in the

core could result in improper guiding of laser light and distortion or disintegration of the lowest order mode.

Figure 24 shows images of the calculated pump absorption profile for the GG IAG fiber with optimal diode to fiber distance, and depth of polished flat. The row a) presents images obtained from a simulation using a cylinder rod with diameter 1.2 cm as a focusing lens, and row b) contains images obtained from a simulation using a cylinder rod with a diameter of 0.6 cm. The three images in each row represent different physical models of the reflective interface between the fiber cladding and the surrounding reflective metal. The first image in each row presents the distribution found when the fiber cladding surface is smooth and all reflections at the fiber-indium interface are considered to be specular. The second image in each row shows the absorbed pump distribution when the fiber exhibits a ground glass finish on its side surface, simulated by a Gaussian roughness model in the ASAP code (see APPENDIX A for code). This roughness results in diffuse reflection at the fiber-indium interface. In addition, the third image in each row shows the resulting distribution of pump energy when the interface between the clad glass and indium metal is described as a completely random scatterer. It can clearly be seen from these images that diffuse reflection from the outer surface of the fiber is key to getting a more uniform pump distribution in the fiber core.

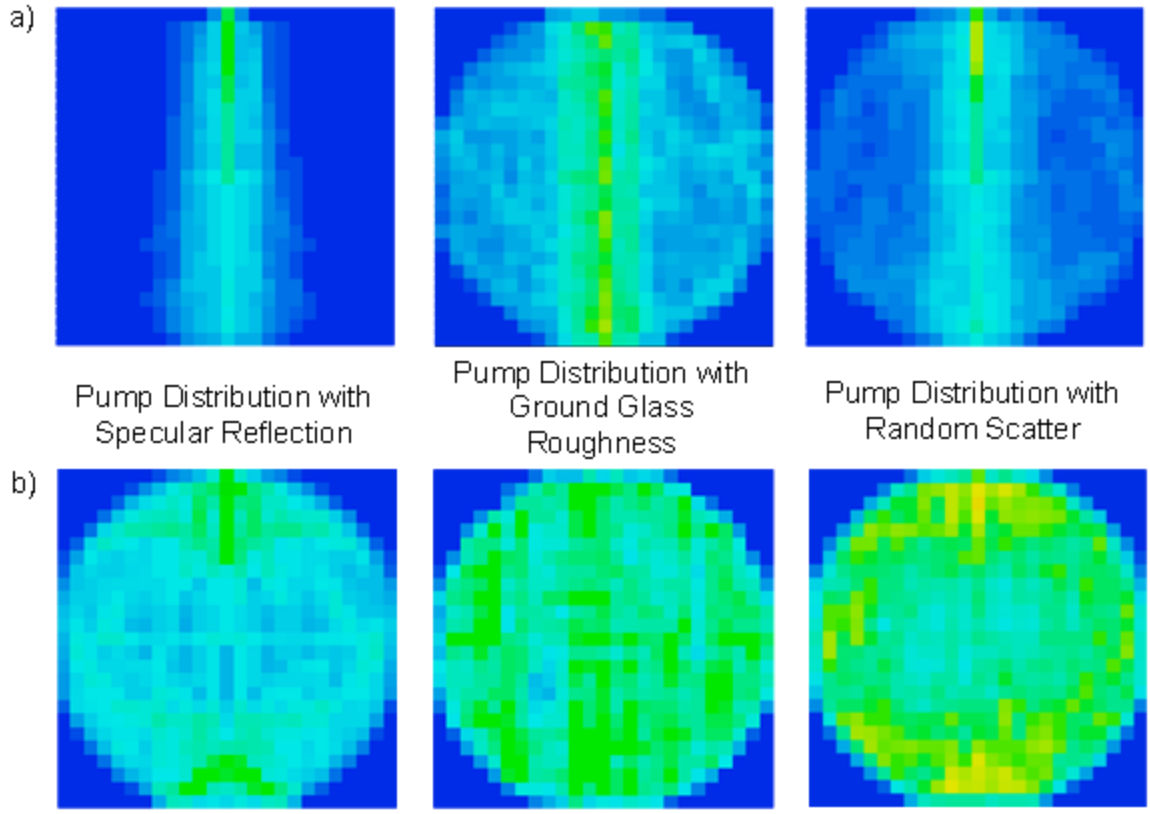

Figure 24 - Images of simulated pump energy distribution in the core of the GG IAG fiber. Three different models are shown for the type of reflection at the fiber-indium interface: pure specular reflection, a Gaussian roughness model that simulates the roughness of ground glass, and pure random scattering at the interface. All images in row a) were obtained using a cylinder rod with diameter 1.2 cm as a focusing lens. Images in row b) were obtained with a cylinder rod with diameter 0.6 cm. In all images, light is initially incident from below the image.

A large difference in uniformity exists between the utilization of a 1.2 cm focusing rod and a 0.6 cm focusing rod. From previous simulation shown in Figure 21, the 0.6 cm rod creates the minimum RMS spot size of 60 μm, while the 1.2 cm rod creates a spot size of 110 μm. Both of these focal sizes are tight enough to pass through the pump window that is 120 μm wide. Interestingly, the pump efficiency when using the 1.2 cm rod is slightly higher at 62% than when using the tighter focusing 0.6 cm rod (56% efficient). This is most likely due to the lower numerical aperture of the larger cylinder lens creating a smaller angular spread in the incident

pump light, resulting in more direct pumping of the core and fewer interactions with the reflective cladding surface.

The results in Figures 23 and 24 indicate that there is a tradeoff between maximum pump efficiency and pump uniformity of the GG IAG core. Since the difference in efficiency between the highly non-uniform distributions created with low NA pumping is only slightly more (6%) than when pumping with maximum NA, the use of high NA pumping with the 6 mm diameter focusing cylinder rod appears to the be best choice.

Non-ideal Reflection

In previous simulations, a pump efficiency of 56% was found when the interface between the fiber and the surrounding indium was considered to be 100% reflective. In order to see what the effect of non-ideal reflection from the indium interface, this simulation was repeated with varying values of indium reflectivity. The effect of the reflectivity at the cladding-metal interface is shown in Figure 25, a plot of expected pump efficiency vs. the reflectivity of the fiber-indium interface.

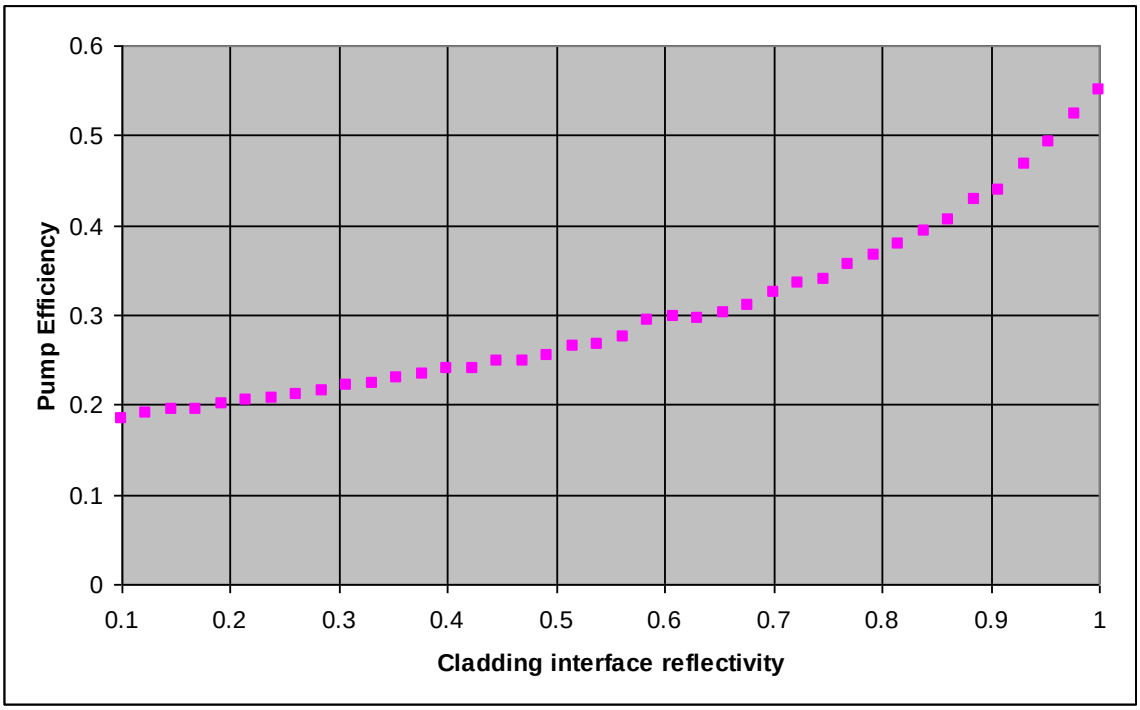

Figure 25 - Pump efficiency vs. the reflectivity of the cladding-metal interface. The simulation was conducted for a side pump system with 6mm diameter rod lens focused at a 120 um pump window.

This clearly shows the importance of the reflectivity of the cladding-metal interface. A drop from 100% reflectivity to 80% reflectivity induces a relative drop of 35% in the expected pump efficiency.

After completing the raytrace simulations, the basic parameters for the implementation of side pumping the GG IAG laser can be specified. The diode bar must be held at least 40 mm from the fiber; light can then be focused into the fiber using a 6 mm diameter cylinder lens. The fiber should have a flat window polished on its side with an ideal depth of 15 μm that would create a window roughly 120 μm wide along the length of the fiber. To optimize the pump distribution along the cross-section of the core, the outer surface of the fiber should be roughened

to create as diffuse a reflection as possible at the fiber-indium interface. Additionally, maximizing the overall reflectivity at the fiber-metal interface is of great importance in maintaining high pump efficiency.

Thermal Modeling of GG IAG Side Pumped Implementation

Another area of concern before implementing the side pumping scheme is the thermal properties of the fiber when held as in Figure 18. In order to analyze the amount and distribution of heating in the fiber due to pump light, finite element modeling (FEM) was conducted though the use of Comsol Multiphysics software. With Comsol, a cross-sectional model of the fiber–indium-V block scheme was created and meshed for FEM modeling. The resulting model is shown in Figure 26.

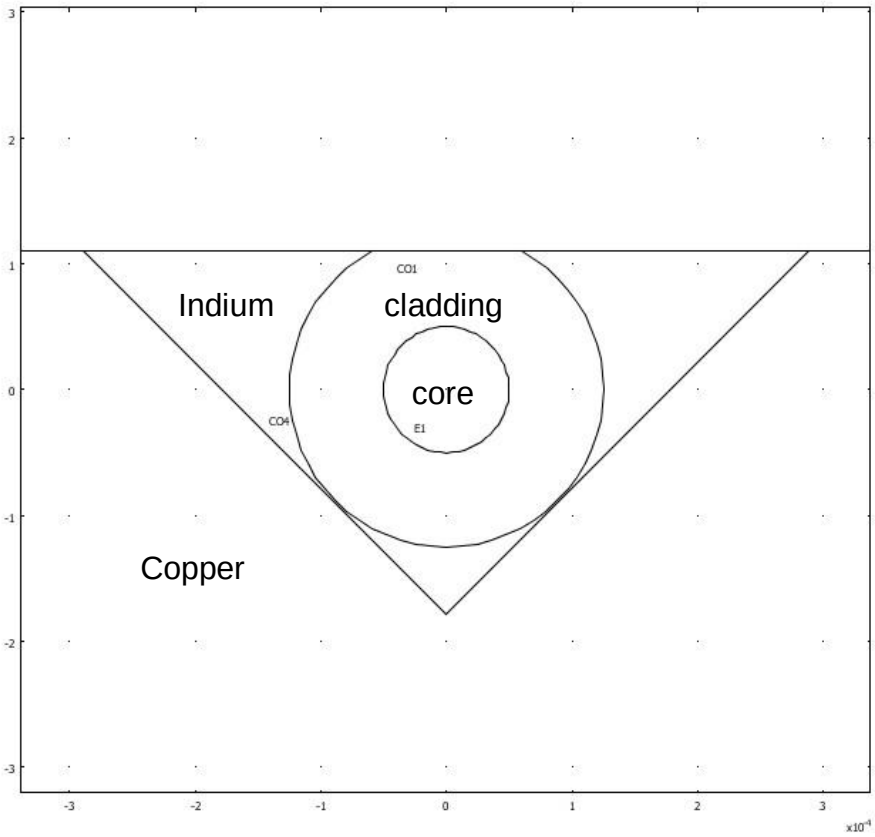

Figure 26 - Cross sectional model of side pumped fiber scheme created in Comsol Multiphysics for thermal analysis.

The physical properties used for the constituent materials of the fiber and mounting structure are listed in Table 3.

	Thermal Conductivity (W/(m*K))	Youngs Modulus Gpa	Poisson Ratio	Density (kg/m^3)
Copper	400	110	0.35	8700
Indium	86	11	0.33	7290
glass	0.82	71.5	0.24	3204

Table 3 - Thermal and physical properties of modeled materials

All air interfaces in the model were set to be thermally insulating, assuming no convective or conductive cooling through the air. The copper block was cooled by two water passages that were assumed to keep the water-copper interface surface at 10 °C.

The heat density inside the core was calculated by using the pump efficiency of the diode side pump and the quantum efficiency of Kigre Q100 glass. Raytrace modeling discussed in the previous section established a pump efficiency of roughly 60% for the geometry under consideration for the side pump scheme. The quantum defect is defined as the ratio of the energy of a photon at laser wavelength to the energy of a photon at the pump wavelength. Thus, the quantum efficiency is one minus the quantum defect.

$$\eta_q = 1 - \left(\frac{hc}{\lambda_{laser}}\right) \Big/ \left(\frac{hc}{\lambda_{pump}}\right) = 1 - \frac{\lambda_{pump}}{\lambda_{laser}} \tag{18}$$

The total heat deposited in the core is then given by

$$P_{heat} = P_{in} * \eta_{pump} * \eta_q \tag{19}$$

Where η_{pump} is the pump efficiency of the system and η_q is the quantum efficiency. For the system, $\eta_{pump} = 0.6$ and $\eta_q = 0.24$. Consequently, the total heat is given by $0.144 * P_{in}$. The power density of heat in the fiber core is the heat divided by the core volume. For one centimeter of fiber the heat density in the core when pumped by diode bars with 50W of CW

power per centimeter of pump length is 91 GW/m^3. This value was used in the Comsol simulation resulting in the final temperature distribution shown in Figure 27 below.

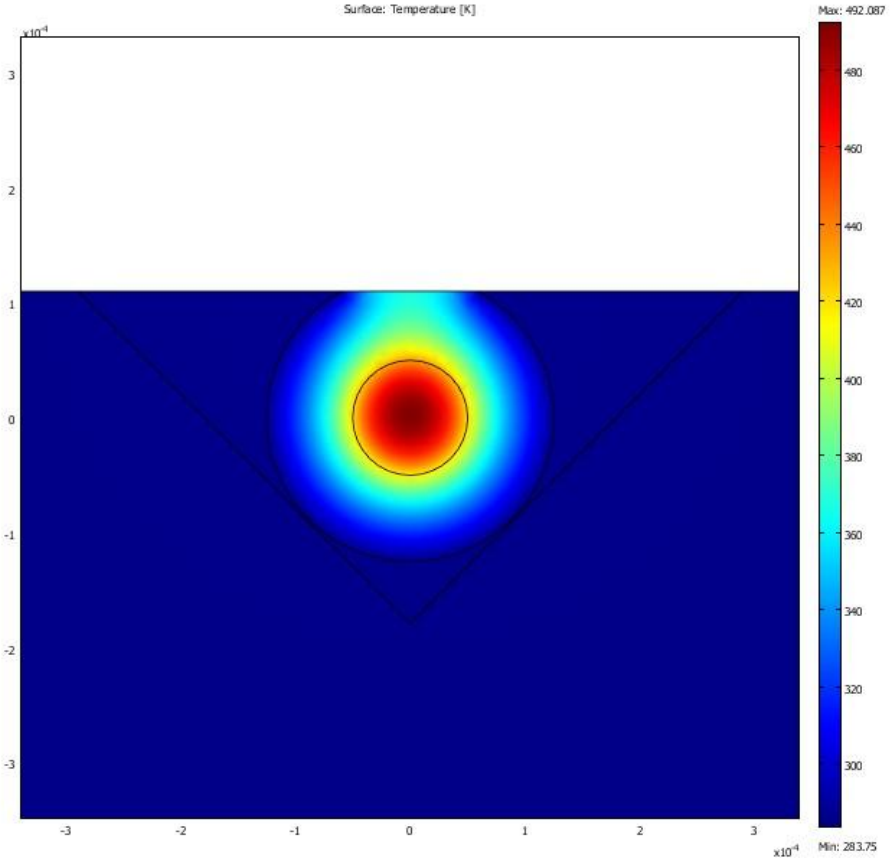

Figure 27 – Temperature distribution in the GG IAG fiber when pumped with 50 W/cm. Maximum core temperature is 219 °C.

The thermal simulation shows that the fiber will reach peak core temperatures of roughly 220 °C. While this is quite hot, it is well below the softening point of the glass at 470 °C. Kigre Q100 glass has a negative change in refractive index with respect to temperature, $dn/dt=-4.6x10^{-6}$ K^{-1}. For this reason, there is no concern that the core glass will lose its antiguiding property due to thermal heating. Figure 28 shows a plot of the temperature distribution across the core of the fiber.

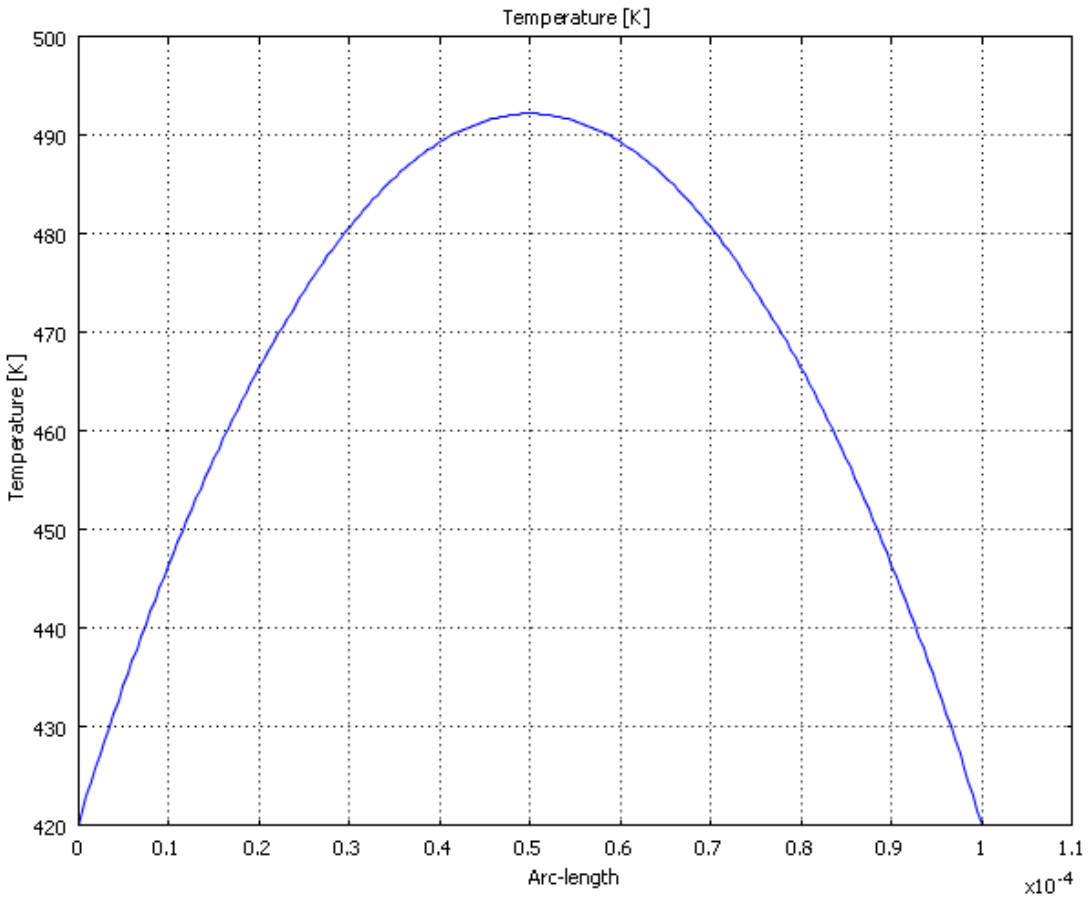

Figure 28 - Temperature distribution across the diameter of the GG IAG fiber core. Total temperature differential is roughly 70 °C.

The 70 °C temperature difference from the center of the core to the outer edges of the core results in an index difference of -0.00032 from the center of the core to the edges, which is only 7% of the index difference between core and cladding. Figure 29 shows the refractive index of the GG IAG both while unheated and when pumped with maximum power (50W/cm).

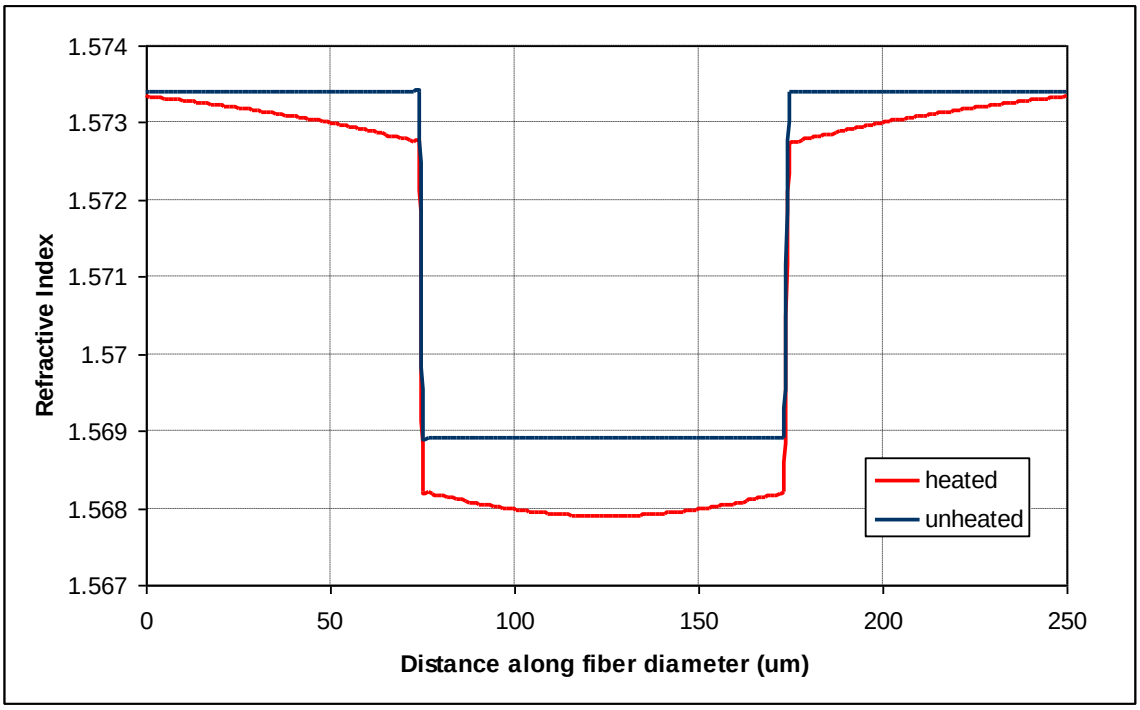

Figure 29 - The calculated refractive index of the GG IAG fiber with and without pump heating. Note that the index step at the core-clad interface does not change due to the uniform and smooth heat distribution in the radial direction.

Modeling of GG IAG Fiber Laser Output

Using Eqs. (14), (10) and (11) the upper and lower limits of output coupler reflectivity that will result in a single mode output for a GG IAG laser can be calculated. For the fiber with a = 50 μm, $\Delta n = -0.0045$, $n_0 = 1.57115$, alpha = 0.01, and $\lambda = 1054$ nm, the reflectivity of the output coupler (assuming the other end reflector is HR) must be between 46% and 29.3% for a 3 cm fiber and between 35.5% and 19.5% for a 4 cm fiber.

Simple modeling of the output from the GG IAG fiber can be accomplished through use of the explicit equations for the output power of the laser developed from the steady state rate

equations for the laser. The development of these equations is explained in full in the second part of this dissertation discussing the temperature dependence of solid state laser systems. These equations can be found in reference textbooks such as Solid State Laser Engineering by W. Koechner [50]. The output out a laser can be expressed simply as:

$$P_{out} = \eta_{slope}(P_{in} - P_{th}) \tag{20}$$

Here P_{in} is the input pump power, η_{slope} is the slope efficiency of the laser, and P_{th} is the threshold power for laser operation. The expressions for η_{slope} and P_{th} are:

$$\eta_{slope} = \frac{(1-R)}{(1+R)} \frac{2\eta}{(L-\ln(R))} \tag{21}$$

$$P_{th} = \frac{(L-\ln(R))h\nu A}{2\sigma_{21}\eta\tau} \tag{22}$$

Here, L is the logarithmic round trip loss in the resonator, R is the reflectivity of the output coupling mirror, h is Plank's constant, ν is the frequency of the laser light, A is the laser mode area, σ_{21} is the emission cross section of the laser transition, η is the pump efficiency of the laser, and τ is the florescence lifetime of the upper laser level. For a 3 cm long fiber, the optical reflectivity of the output coupler required to maintain single mode lasing is 40%, and for a 4 cm long fiber, it is 30%. The optical properties of Q100 glass are listed in Table 4 and were used in equations (21) and (22) to produce a simple output model for the GG IAG laser.

Index of Refraction	1.555
Fluorescent Lifetime	190 us
loss	.0008 %/cm
laser wavelength	1054 nm
linewidth	25 nm
emission cross section	4.4e-20 cm^2

Table 4 - The optical properties of Q100 laser glass

Using the properties from Table 4, and equations (21) and (22), the output can be predicted for both 3 and 4 cm GG IAG lasers made from the 100 μm core, 10% doped GG IAG fiber.

Figure 30 shows plots of predicted laser output versus pump power for 3 and 4 cm lasers for assumed pump efficiencies of 50%, 40%, 30%, and 20%.

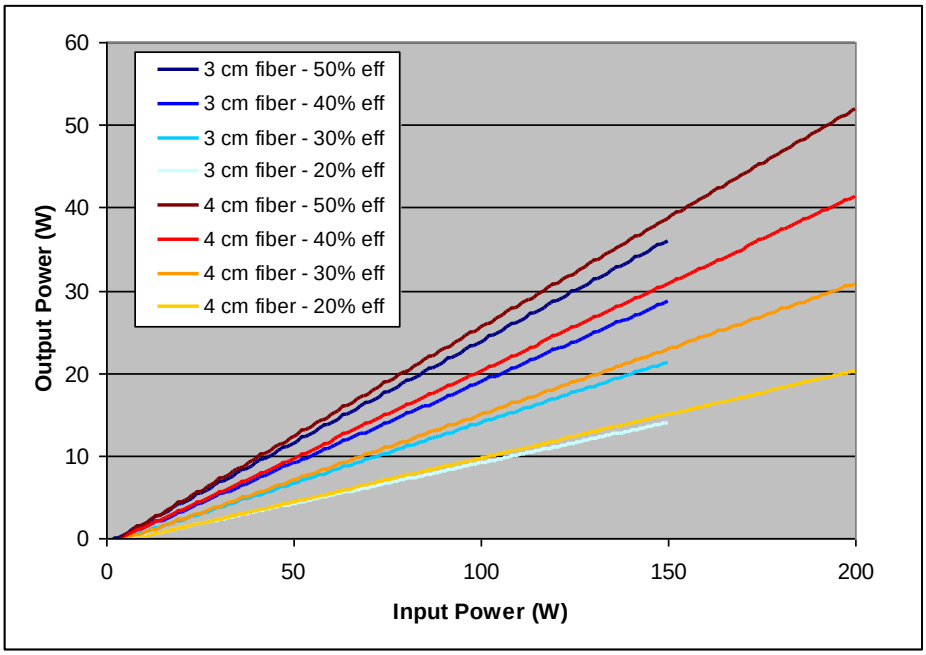

Figure 30 – Calculated theoretical CW output for 3 and 4 cm long GG IAG fibers with pump efficiencies of 50%, 40%, 30%, and 20%. The maximum assumed pump power was 50 W/cm.

These plots show that the side-pumped GG IAG fiber laser designed above is capable of up to 35 W of output power for a 3 cm fiber, and over 50 W for a 4 cm fiber.

Experimental Preparation

Having fully modeled the GG IAG fiber and optical side pump configuration, the next step was to begin implementing the side pump scheme. The initial simulation showed that the 100 μm core diameter, 250 μm clad diameter fiber should be prepared with a roughened outer surface and a 15 μm deep polished flat for side pumping. Optical diode to fiber distance was found to be 40+ mm from the fiber, utilizing a 6 mm diameter focusing rod held a little over 6 mm from the fiber. Surrounding the rod with indium solder and holding it in a water cooled copper V-groove would provide enough thermal contact to prevent severe thermal problems in the fiber. For initial testing, three micro-lensed, 50 W CW, 808 nm diode bars purchased from spectra physics were already on hand for a side pumped proof of principle test. A linear array of four 50 W micro-lensed diode bars, with emission centered at 808 nm, was ordered from Dilas.

Fiber Preparation

The first step in fiber preparation was to roughen the outer surface of the fiber. The first attempt at surface roughening was to etch the phosphate glass fiber with HF acid. A glass frosting kit containing a buffered HF solution was purchased and tested on glass slides. These test cases showed good ‘frosting’ of the glass with a resulting surface roughness similar to a standard

ground glass finish. However, when this solution was used on the phosphate glass fibers, it had no effect. Higher molar concentrations of HF acid were used and none was found to affect the phosphate glass.

A paper was located that purported success in etching phosphate glasses with strong alkali solutions of KOH or NaOH [51]. Tests were conducted on test pieces of phosphate glass fibers to determine the optimal KOH concentration for etching the fiber phosphate glass. Figure 31, shows a plot of fiber diameter vs. time for a 10 M KOH solution (the highest concentration used) held at 75 °C.

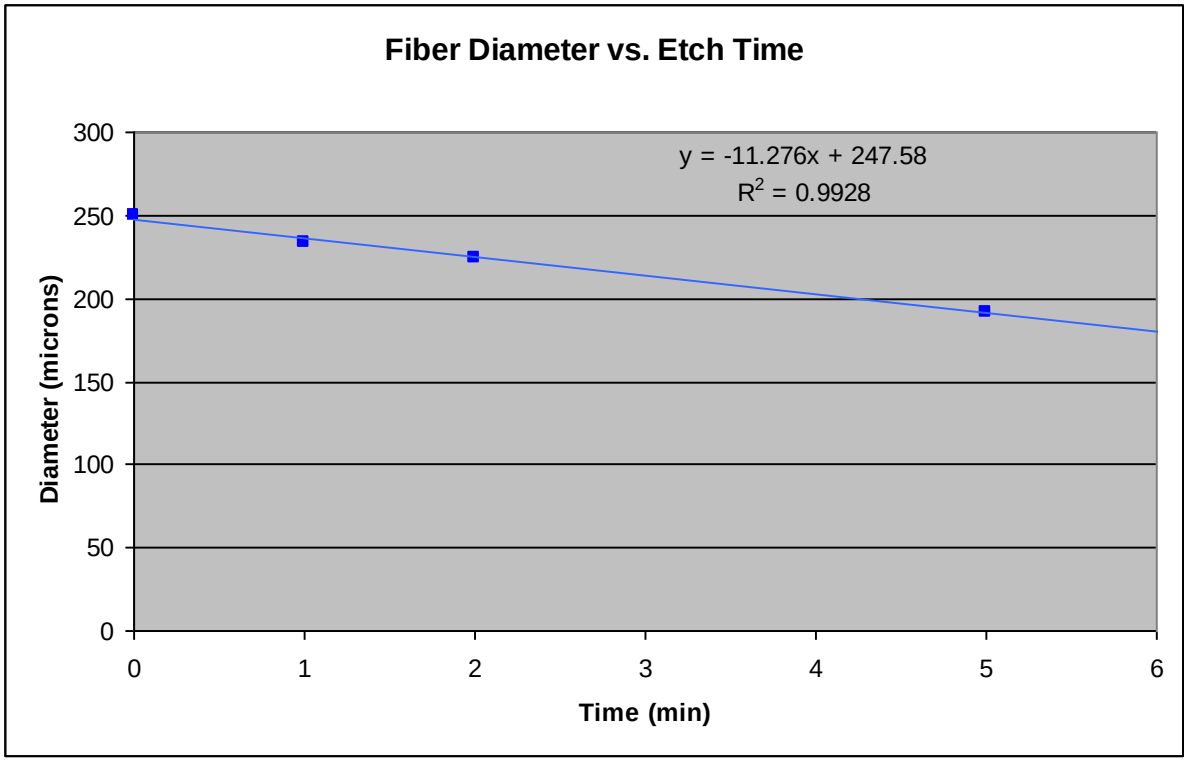

Figure 31 - Etching of GG IAG Kigre phosphate glass fibers. The etch rate was found to be 11 microns per minute of fiber exposure.

The tests showed an etch rate of roughly 11 μm per minute, which was slow enough to allow some precision in determining the amount of etched material. However, the fibers did not etch in a manner conductive to creating an optically roughened surface. The fiber surface was observed to form cracks and then peel off the fiber as it was etched, leaving a smooth surface behind. A series of photographs taken of fibers etched for differing amounts of time in 8 M KOH is displayed in Figure 32, showing the cracking and peeling of the outer surface.

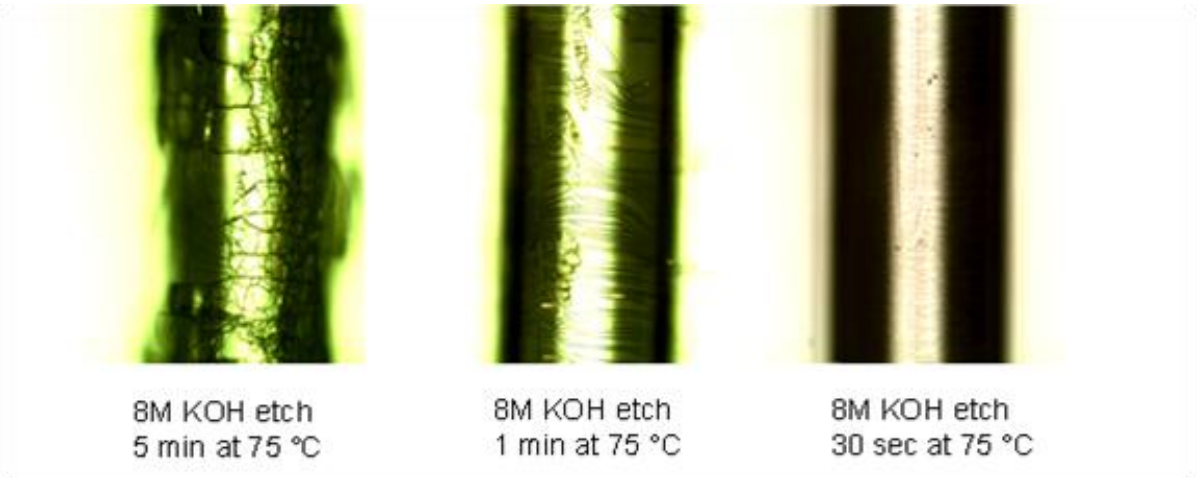

Figure 32 – Photographs of etched phosphate glass fibers. Cracking of the fiber surface was observed for all etch times. Longer etch times resulted in deeper cracks and greater pealing of the surface layer.

Attempts at changing this etching behavior by altering the etchant concentration did not affect the type of cracking seen on the fibers. Since chemical etching of the fibers proved to be inadequate for creating a roughened surface and the fibers were too physically fragile with their 0.25 mm diameter to physically abrade, the decision was made to try side pumping without roughening the outer surface of the fiber.

A 7.62 x 2.54 x 3 cm, copper block was fabricated with a water channel running lengthwise through its middle to act as a heat sink and cooling source for the side pumped fiber. V-grooves with a depth of 0.279 mm were machined in a 3.175 mm copper plate that was designed to mate to the top of the copper cooling block. This way, multiple fiber holding blocks could be used to mount fibers and be swapped in and out when needed. APPENDIX B contains the mechanical drawings for the 4 cm fiber length version of the cooling block and plate.

Fibers were cleaved with lengths of 3.1 cm so that a small portion of the fiber ends would stick out beyond the mounting plate to prevent damaging them during polishing. The small copper V-groove plate, shown in Figure 33, was then placed on a hot plate and heated above the melting point of indium.

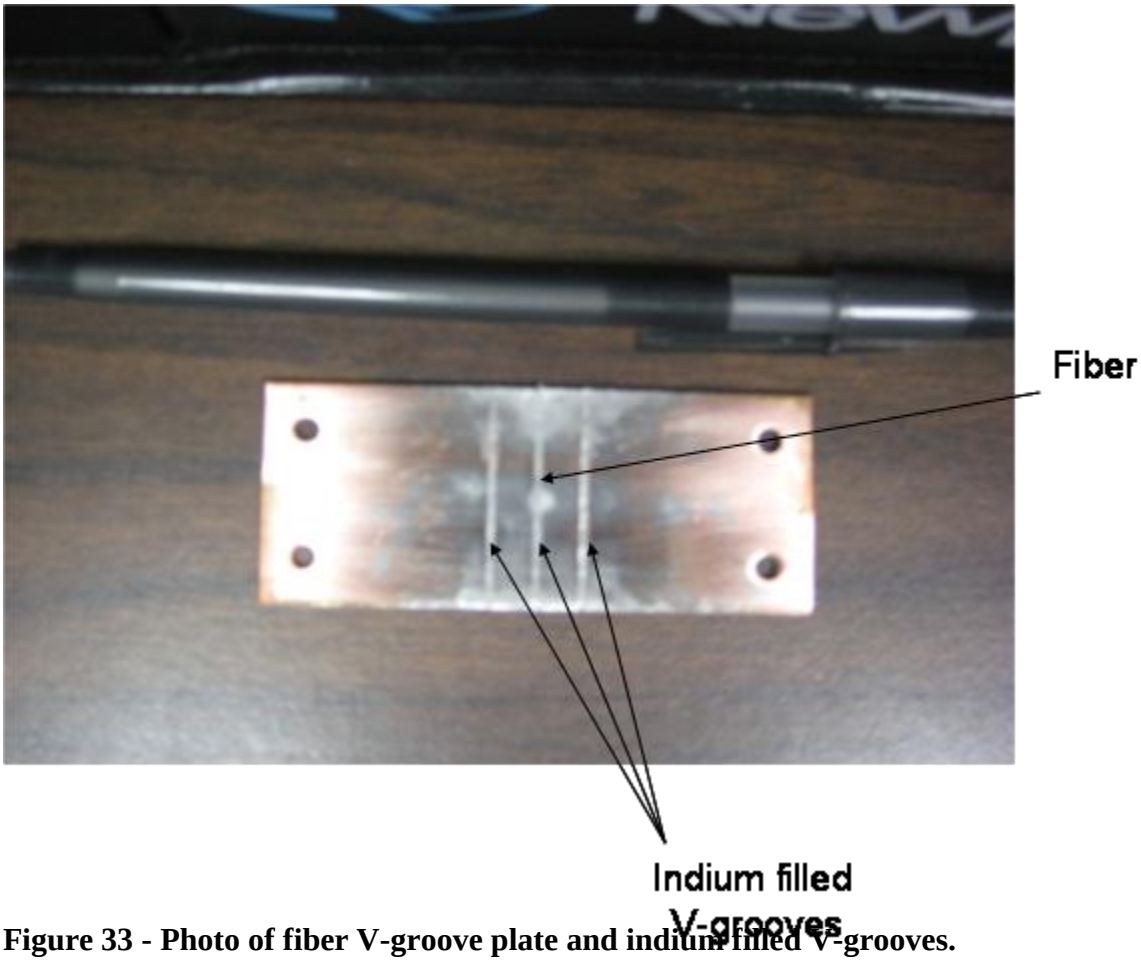

Figure 33 - Photo of fiber V-groove plate and indium filled V-grooves.

Indium wire was then placed in the V-grooves and heated until the grooves were full of molten indium. At this point, the fibers were placed in the liquid indium filled grooves and forced down with a weighted block. The entire plate was allowed to cool until the indium had reached room temperature. The plate was then polished using very fine polishing paper, starting with 50 μm grit until the exposed 'windows' of the fibers reached roughly 100 μm in width. At this point, finer and finer grit polishing paper was used to polish away the remaining depth and create a nice smooth finish to the exposed fiber pump windows. When the polishing was complete and the pump window measured at 120 μm in width, the pump window and end surface of the fiber were

cleaned and the fiber block was ready for mounting in the side pumped setup. Figure 34 contains optical microscope images of the fiber pump window and end surfaces.

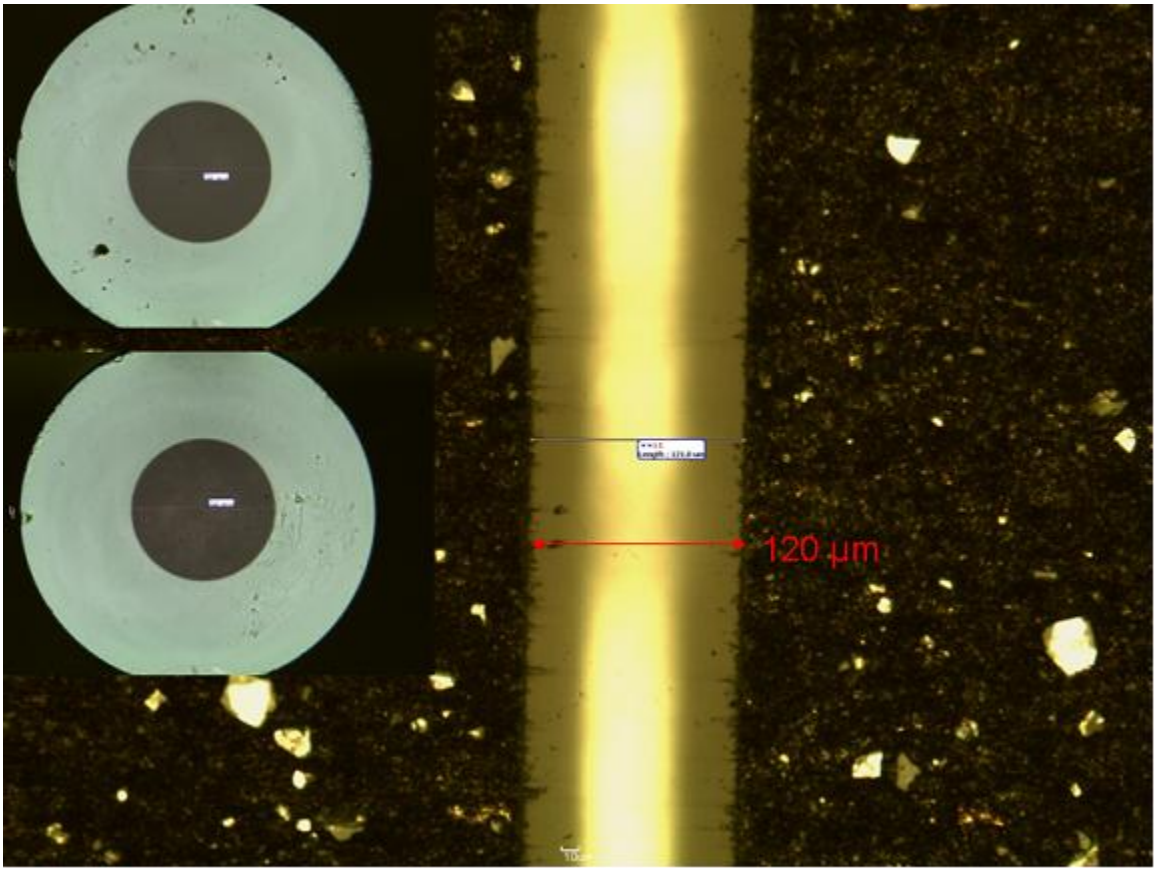

Figure 34 - Photo of the fiber pump window and inset photos of the end faces showing core and cladding. The blue bordered white rectangles seen in the photograph are distance measurements placed in the image by the optical microscope's imaging software. The pump window was measured to be 120 µm wide and the fiber core 100 µm in diameter at both fiber ends.

Experimental Setup

The initial side pump setup utilized three 50 W, CW, 808nm, micro-lensed, diode bars manufactured by Spectra-physics. These diode bars were attached to an aluminum-cooling block

that was connected to a chilled water system and were located above a 5 mm diameter, uncoated glass rod (the closest to 6 mm that was readily available). The copper cooling block and V-groove plate were held together with a layer of thermal grease spread between them to insure good thermal contact. The block was then placed on a rotation and tip/tilt stage that was in turn connected to x and y translation stages, creating the maximum number of degrees of freedom to bring the fibers into alignment with the pump beams. A flat, HR mirror at 1064 nm was placed close to one end of the fiber and an output coupler with 43% reflectivity (calculated to result in single mode operation of the laser) was placed within a few mm of the other fiber end. The mirrors were aligned to the fiber using a HeNe alignment beam that was directed through the fiber. The diodes were driven by a pulsed power supply at a rate of roughly 1 Hz with pulse duration of 3 ms. Output florescence of the fiber was monitored with a beam-imaging camera placed near the laser output coupler. The alignment of the HR mirror and output coupler was adjusted to peak up the florescence intensity until the system began to lase. A photograph of the setup is shown in Figure 35.

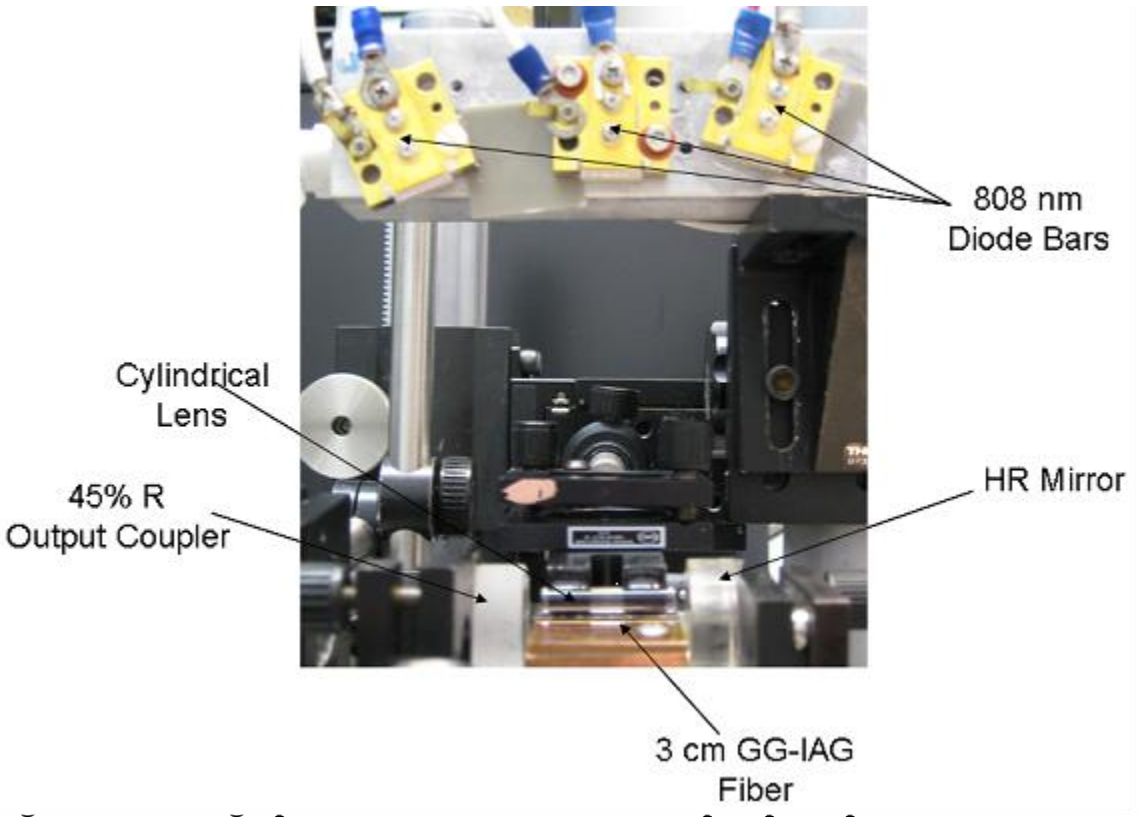

A later, improved version of the side pumped setup used a linear diode array purchased from Dilas that contained four 50 W, 808 nm, micro-lensed diode bars in a highly toleranced linear array with 1.5 mm spacing between each bar. A photograph of this improved setup is shown in Figure 36.

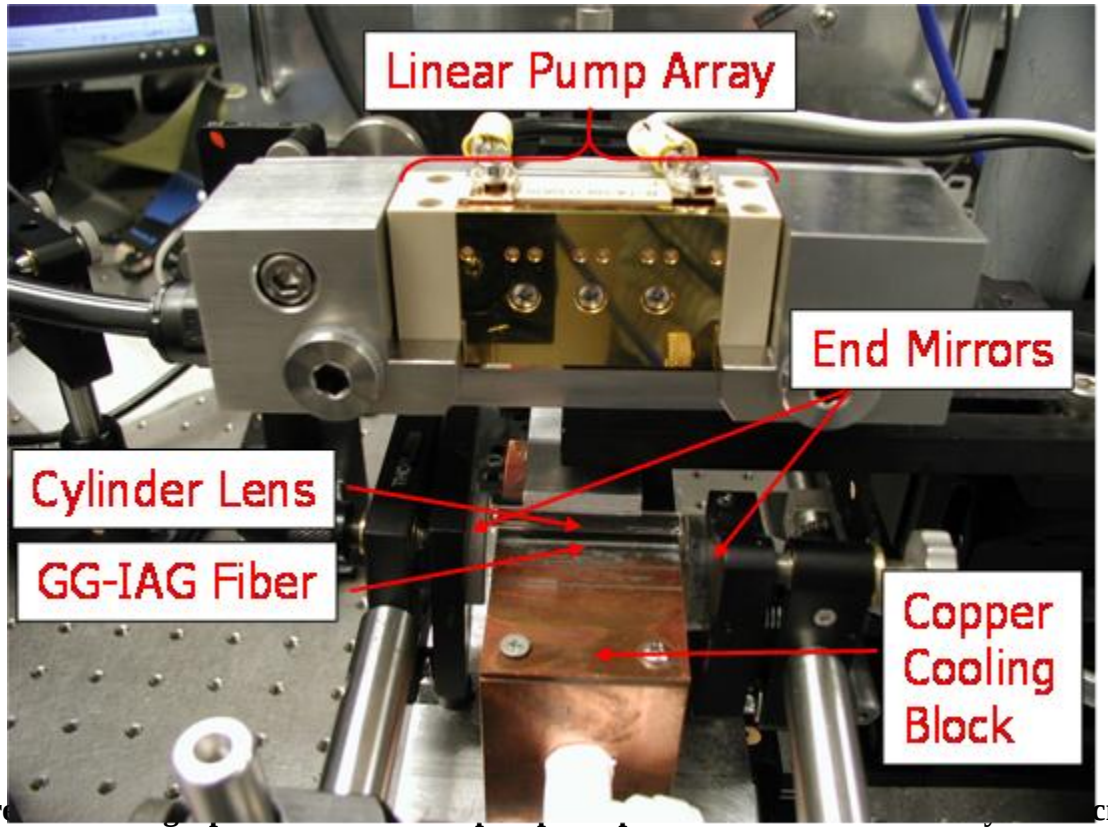

Figur cm fiber.

Measurements

The initial side pumped setup using three individual diode bars as a pump source was first made to lase with a 43% reflectivity output coupler. The beam profile was measured with a Pulnix 745 camera processed with Spiricon Laser Beam Analysis software. The image is shown in Figure 37.

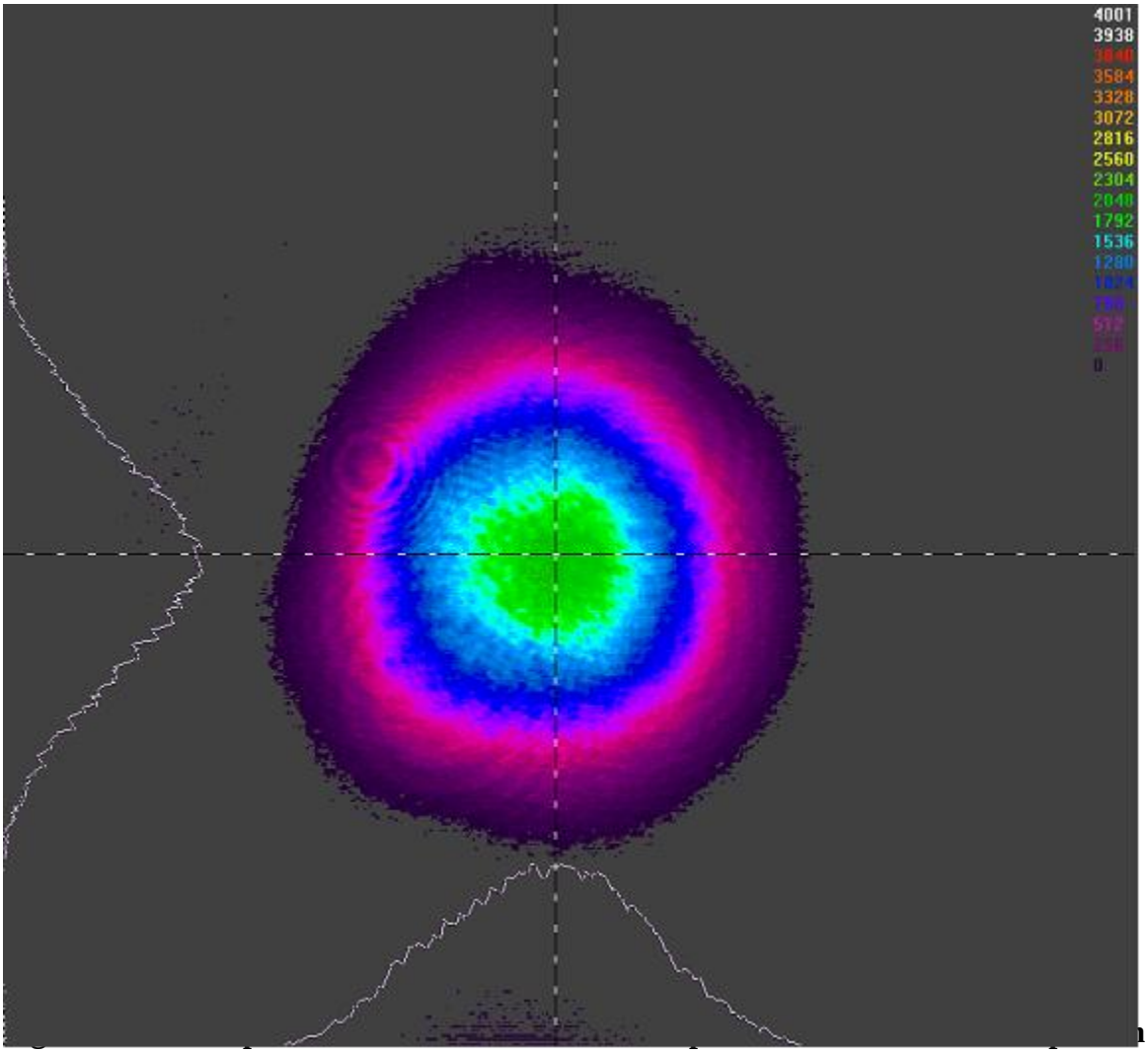

LBA-PC software and a Pulnix 745 camera. The GG IAG laser used a 43% reflectivity mirror.

The laser output was also measured using an Ophir Laserstar power/energy meter with a PE25-BB pyroelectric detector head. During these measurements, the diode source was driven at 1 Hz with 3 ms duration pulses. Figure 38 shows the output vs. input energy per pulse and enables a measurement of slope efficiency.

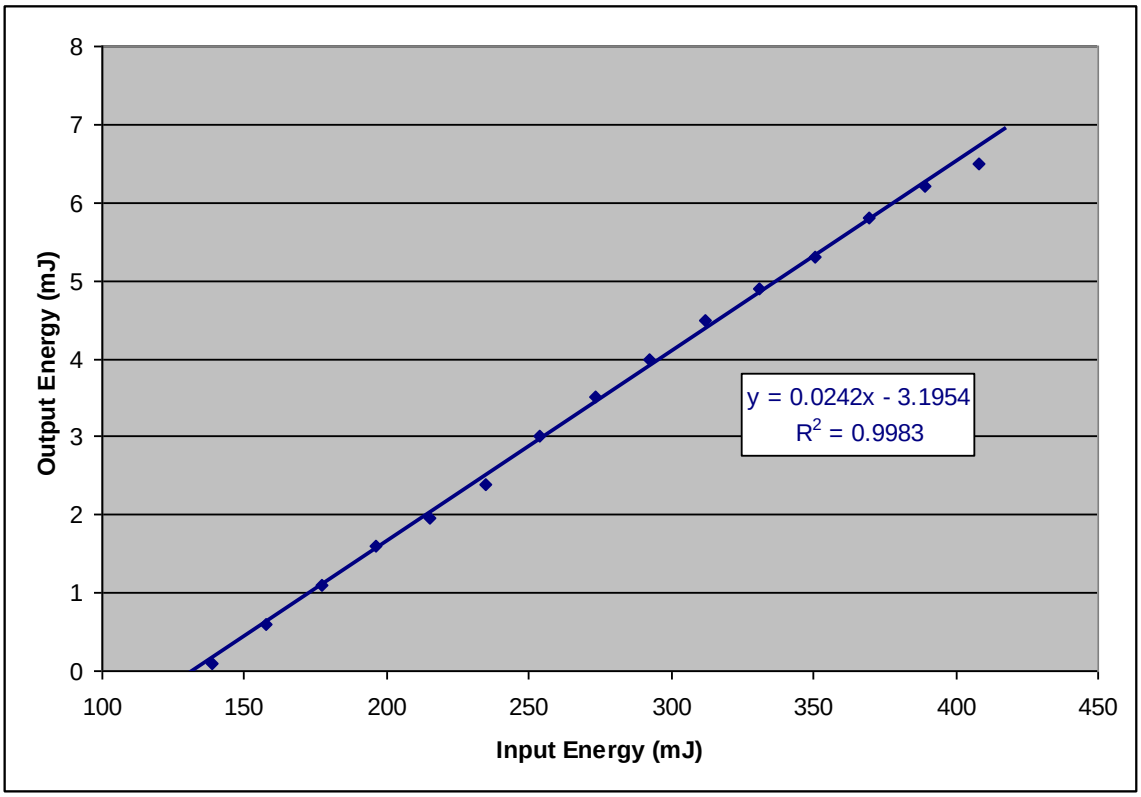

Figure 38 - Measured output vs. input energy for the GG IAG fiber laser pumped with three individual 50W diode bars, pulsed at 1Hz with 3ms pulse duration.

The resulting curve yielded a slope efficiency of 2.4% and maximum pulse energy of 6.5 mJ, corresponding to a pulsed power of 2.2W.

Additionally, the beam divergence of the GG IAG output beam was determined by measurements of the $1/e^2$ beam diameter of the beam at successive points along its path. Unfortunately, the beam was too divergent to use the Spiricon M^2-200 beam divergence and M^2 measurement tool due to the limited size of the Pulnix camera's CCD array. After only 13 cm from the fiber, the beam was too large to be accurately measured with the CCD of the camera. The hand calculated full angle beam divergence was 840 mrad. The divergence of an ideal Gaussian beam with 50 μm waist is 13.4 mrad as calculated from:

(23) $$\Theta = \frac{2\lambda}{\pi w_0}$$

This shows that the beam for the GG IAG laser is clearly multimode.

These measurements were later repeated with using a dedicated linear pump array as the pump source for a 4 cm long GG IAG fiber. The beam profile of this beam, using a 33% output coupler, is shown below.

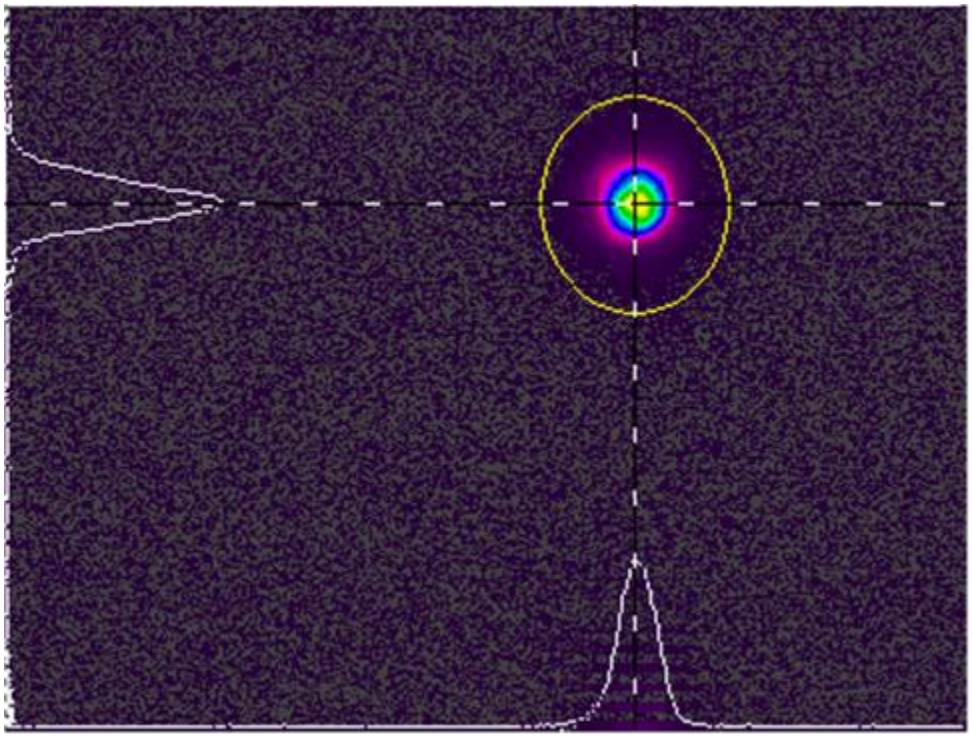

Figure 39 - Beam profile of the GG IAG laser beam pumped with a Dilas linear array. The profile was captured with Spiricon LBA-PC software and a Pulnix 745 camera.

The slope efficiency curve of laser output was again measured using an Ophir Laserstar power/energy meter with a PE25-BB pyroelectric detector head while the diode source was

driven at 1 Hz with 3 ms duration pulses. The plot of output vs. input energy per pulse is shown in Figure 40.

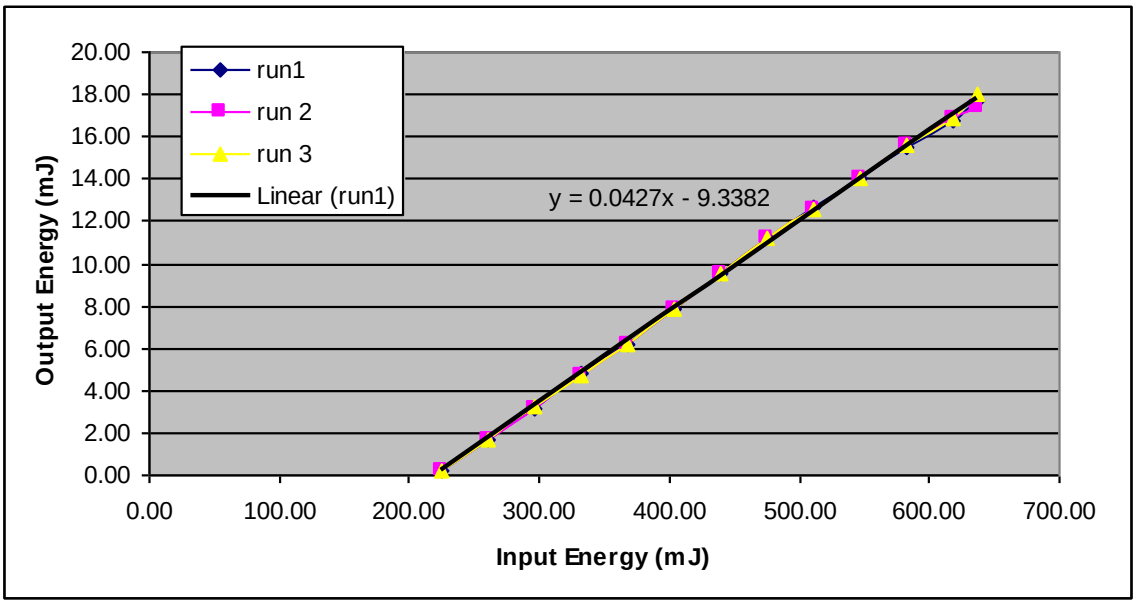

Figure 40 - Measured output vs. input energy for the 4 cm long GG IAG laser pumped with a Dilas linear array with rep rate of 1 Hz and pulse duration of 3 ms.

The resulting slope efficiency was 4.3%, or roughly double that found with the individual diode bars. Maximum output pulse energy was 18 mJ, corresponding to 6 W of pulsed power. The beam divergence was again measured and found to be greatly improved to a half angle divergence of 10 mrad. This beam had a low enough divergence that the M^2-200 could be used and the beam was determined to have an M^2 value of 1.4.

Discussion

The initial implementation of side pumping of a GG IAG fiber laser with three individual diode bars was successful in obtaining lasing from the fiber, but lacked the single mode output beam that is the primary benefit of the GG IAG concept. This was most likely due to problems with the uniformity of the pump along the length of the rod. Since each of the three diode bars were mounted separately on a single cooling block, there was little that could be done to ensure that the output beams from each bar were particularly well aligned to each other. While the GG IAG laser was running, each diode bar was blocked to see what effect it had on the overall output power of the laser. It was found that one bar in particular contributed significantly to the pump power (whenever it was blocked the laser dropped below threshold); however, another bar was found to have very little contribution to the laser output power. Blocking this second bar only dropped the output power of the laser by 10%. The third bar exhibited a contribution that was in between these extremes, with the laser dropping to just above threshold when it was blocked. Since the diode bars failed to contribute equally to the laser output power, it can be assumed that each coupled into the GG IAG fiber with significantly different efficiency, resulting in a highly variable gain distribution. Each diode pumped a different section of the fiber so that some sections of the fiber were pumped much less than others, potentially resulting in some sections of the fiber remaining below the threshold gain for single mode operation, preventing single mode operation for the fiber as a whole.

An additional factor that might have contributed to non-uniform pump along the length of the fiber was the lack of a rotational freedom of the cylinder focusing lens. This lens could be precisely aligned vertically and horizontally but could not be rotated with any accuracy.

Consequently, alignment between the pump diodes (which could only be moved in the vertical axis) and the focusing cylinder was very problematic. It can safely be assumed that the diode light was incident on the focusing cylinder at an angle slightly skewed from the axis of the cylinder. This would result in aberration in the focused spot of the pump beam and create further non-uniformity in the pump profile along the fiber length.

Table 5 contains the calculated slope efficiencies and threshold energies determined from the laser rate equation based expressions (21) and (22), using the pump efficiencies obtained from ray trace simulation for several values of the fiber-metal interface reflectivity.

% R of fiber/metal interface	Pump Efficiency (from simulation)	Calculated Slope Efficiency	Calculated Threshold Power (W)	Equivalent Threshold Energy (mJ)
10	18.30%	8.69%	8.12	24.37
20	20.20%	9.60%	7.36	22.08
30	22.10%	10.50%	6.73	20.18
40	23.90%	11.35%	6.22	18.66
50	25.90%	12.31%	5.74	17.22
60	29.60%	14.06%	5.02	15.07
70	32.50%	15.44%	4.57	13.72
80	37.20%	17.67%	4.00	11.99
90	43.50%	20.67%	3.42	10.25
100	50.10%	23.80%	2.97	8.90

Table 5 - Calculated slope efficiencies, and threshold energies based on simulated ray trace for 3 cm fiber utilizing a 43% output coupler. The measured slope efficiency of the 3 cm fiber laser was 2.4% with a threshold energy of 132 mJ.

The measured slope efficiency was almost a factor of four lower than predicted for a worst-case scenario of only 10% reflectivity at the fiber-metal interface. This lends credence to the assumption that the individual diode bars did not couple well into the fiber due to poor bar to bar alignment tolerances.

The utilization of the linear diode array as a pump source greatly increased the effectiveness of the GG IAG fiber. The output beam was found to be of high quality with an M^2 value of 1.4 (an M^2 value of 1.0 is obtained for a perfect Gaussian beam). The slope efficiency of the output was also roughly double that found for the three individual pump diodes (4.3% instead of 2.4%). Table 6 contains the calculated slope efficiencies and threshold energies for this 4 cm fiber, determined from the laser rate equation based expressions (21) and (22), using the pump efficiencies obtained from ray trace simulation for multiple values of the fiber-metal interface reflectivity.

% R of fiber/metal interface	Pump Efficiency (from simulation)	Calculated Slope Efficiency	Calculated Threshold Power (W)	Equivalent Threshold Energy (mJ)
10	18.30%	9.49%	9.40	28.21
20	20.20%	10.48%	8.52	25.56
30	22.10%	11.46%	7.79	23.36
40	23.90%	12.40%	7.20	21.60
50	25.90%	13.43%	6.64	19.93
60	29.60%	15.35%	5.81	17.44
70	32.50%	16.86%	5.30	15.89
80	37.20%	19.29%	4.63	13.88
90	43.50%	22.56%	3.96	11.87
100	50.10%	25.98%	3.44	10.31

Table 6 - Calculated slope efficiencies, and threshold energies based on simulated ray trace for 4 cm fiber utilizing a 33% output coupler. The measured slope efficiency of the 4 cm fiber laser was 4.3% with a threshold energy of 219 mJ.

While use of the linear array did increase the slope efficiency of the GG IAG laser and drastically improved the beam quality obtained from the laser, it still exhibited pump efficiency much lower than expected from the raytrace simulations. The longitudinal pump uniformity of the fiber was greatly improved, but there still appeared to be some problems with effectively coupling the light into the fiber core. Explanations for this difference in pump efficiency

between theory and experiment include the lack of rotational alignment between the pump array and the focusing cylinder, the lack of AR coating on the focusing cylinder (decreases pump efficiency by 8%), poor optical quality and uniformity of the pump window, and loss of light due to the gap between the external mirrors and the end faces of the fiber.

An ideal way to solve many of these issues is to increase the diameter of the fiber core and cladding. Figure 41 shows a plot generated in ASAP of pump efficiency vs. core size for a fiber with ratio of core diameter to total diameter of 0.4 (identical to the fiber that was tested in these reported experiments).

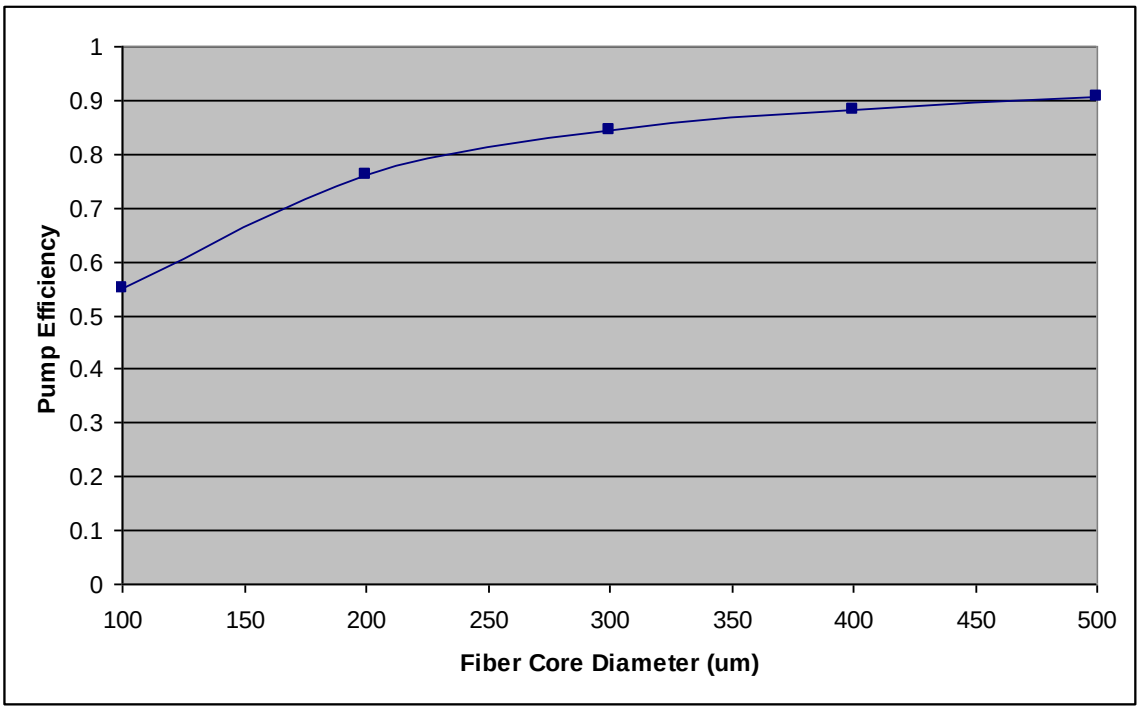

Figure 41 - Plot of pump efficiency verses fiber core size for a side pumped GG IAG fiber with core to total diameter ratio of 0.4, doped with 10% Nd^{3+}.

Increasing the size of the fiber drastically increases the pump efficiency due to the increase in the percentage of the fiber diameter that is covered in reflective material (if similar pump window sizes are used for each fiber). Additionally, the interaction length between the pump light and core material is increased for larger core sizes, increasing the total amount of energy deposited in the core each time a light ray passes through it.

Increasing the cross-sectional size of the fiber would also help with the fabrication process. Mounting and polishing the 250 μm fibers was found to be exceedingly difficult due to the fragile nature of the fibers. It was very common to snap off the fiber ends during the polishing process, and it was very difficult polishing a flat in such a small fiber. Larger fibers would be easier to hold, easier to polish, and easier to align.

One potential concern with using larger fibers would be the effect of the increased thickness of the poorly thermally conducting cladding glass on the heat distribution in the fiber. Simulations using Comsol Multiphysics FEM analysis show that there is actually no increase in core temperature with increasing fiber size if the pump efficiency stays constant. This is due to the fact that the pump power per unit length of the fiber is determined by the pump diodes and is limited to roughly 50 W/cm for a CW diode bar. For larger fibers, this same pump power is spread over a larger core area and has a much larger surface area over which to conduct to the copper cooling block, counterbalancing the longer distance it must travel through the low thermal conductivity cladding glass. Since, in a real system, the pump efficiency will increase with core size, the total power absorbed in the core will increase as well. The resulting core

temperatures for larger sized fibers are plotted in Figure 42, where the pump efficiency used in the calculation is taken from Figure 41.

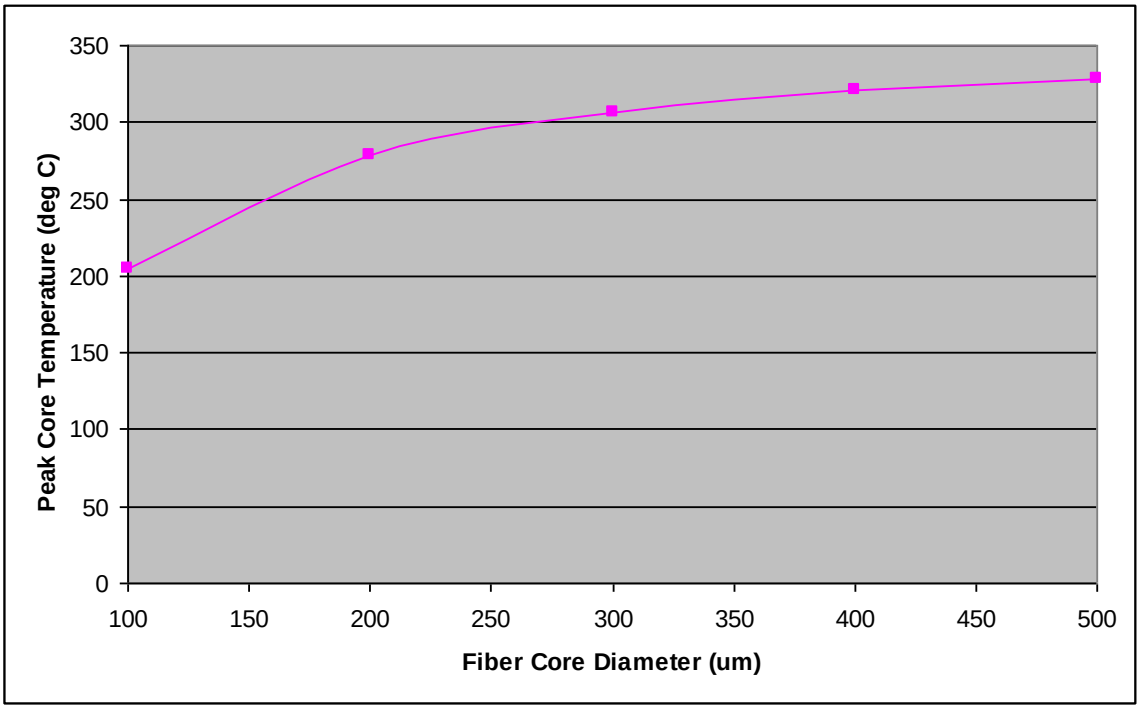

Figure 42 - Change in peak core temperature with increasing fiber core diameter (with 0.4 core to total diameter ratio) assuming increasing pump efficiency from Figure 41.

While the temperature in the core does rise significantly, it does stay well below the softening temperature for the phosphate glass of 470 °C. If thermal issues were to become a problem, the fiber could be fabricated with a relatively smaller cladding diameter or the cladding could be thinned through etching of the fiber with KOH.

Conclusions

Side pumping of GG IAG fibers for the creation of a scalable pump method with which to create low to single mode fiber laser operation was demonstrated using a linear diode bar array for a pump source and a 100 μm diameter core, 250 μm diameter cladding, index antiguided fiber doped with 10% wt. Nd^{3+}. The core glass (Kigre Q100 phosphate laser glass) index of refraction was 1.5689 and the cladding index of refraction was 1.5734 for an index difference of -0.0045. Laser slope efficiency of 4.3% was measured with a total output pulse energy (when pumped for 3 msec) of 18 mJ resulting in a pulsed power of 6 W. The beam quality was measured with a Spiricon M^2-200 and found to be 1.4, showing that the beam was indeed single mode.

The pump technology developed can be scaled to longer fiber lengths and large fiber diameters. Increased fiber core and cladding diameters have been shown through simulation to drastically increase the pump efficiency of the fiber, while not greatly affecting the temperature of the core glass. Large core/clad diameter fibers were not utilized in this study due to the present un-availability of newly drawn fibers. Future work on developing optical fiber designs for increased pump efficiency and lengths optimized to provide highly efficient laser performance with output couplers can be accomplished when new materials become available.

Additional effort can be put into increasing the pump efficiency of the present system though increasing the reflectivity of the material surrounding the fiber. This could be accomplished by applying a gold coating to the fiber before mounting the fiber in the V-groove and fabricating the pump window. Additionally, a more optimal cylindrical lens can be utilized,

with AR coating and increased freedom in angular alignment of the lens to diode bars. This would increase the amount of pump light coupled into the fiber core.

Another area of future work is the extension of the GG IAG concept to different gain materials. Of immediate interest is the use of Yb^{3+} doped glass as a fiber core for its low quantum defect that would reduce the heat load in the fiber. Additionally, the use of erbium glass in the fiber core would lead to the development of eye-safe GG IAG fiber lasers, and (with resonant pumping of erbium glass) an even more efficient fiber laser.

Finally, the development of index crossover pump technology for future GG IAG fibers offers the potential of a much simpler to implement pump for GG IAG fibers. However, a great deal of material development must first be put into the realization of a fiber with core and cladding with distinctly different dispersive properties but similar enough mechanical properties to be pulled into a fiber.

DEVELOPMENT OF PASSIVE ATHERMALIZATION

Introduction

The laser was first demonstrated in 1960 by Ted Maiman at Hughes Research Laboratory in Malibu, California [1]. From its first inception, it is well known that the laser was deemed "the solution in search of a problem". Over the last half-century, many uses have been found for the laser, from compact disk reader to surgical scalpel to generator of atomic fusion. However, most of these uses of laser systems leave them in the comfortable, temperature controlled, indoor environment of a laboratory or workplace. Many issues arise when laser systems are called on to be used in rugged, unforgiving environments that typically arise outside the comfortable confines of a laboratory. Chief among these are the system's ability to withstand shock and vibration, contamination from both the outside environment or from within a sealed laser system, and thermal issues arising from a highly varying ambient temperature of use.

Thermal effects in laser systems and their effective management are a crucial subject in the field of laser engineering. While it is an often-ignored subject in introductory laser courses and texts, thermal management is of great concern in the operation of a laser system outside the safe confines of a controlled laboratory environment. There are two general types of thermal effect in a laser system: problems arising from changes in system alignment due to the changing temperature of the mechanical structure of the laser, and problems created by the changes induced in the optical properties of elements in laser resonator and subsequent beam path. Each of these basic types can be further divided into effects deriving from thermal gradients induced

in the laser due to its operation, and effects relating to the overall system temperature that is driven by the ambient environment.

Thermal Effects in Laser Systems

Optomechanical engineers have spent a great deal of effort in the years since the inception of the laser attempting to make optical housings and mounts that will not misalign due to thermal expansion and contraction of the constituent materials. Engineers often rely on the use of structural materials with low coefficients of thermal expansion, such as Invar (a nickel-steel alloy with a coefficient of thermal expansion less than a fifth that of ordinary steel) and ZERODUR® (a glass with very low thermal expansion created by Schott). Optomechanical engineers often use clever design tricks to counterbalance thermal expansion in a laser system so that there is no net effect on system alignment. These techniques can be implemented fairly easily for situations where the temperature of the laser changes as a uniform whole, such as one would expect to arise from changes in the ambient temperature of the system's working environment.

The situation becomes much more difficult when dealing with temperature gradients induced across sections of the laser housing or across individual optical mounts due to the waste heat deposited in the laser from system operation. Due to the fundamental quantum defect that must exist in a laser system and unavoidable inefficiencies in the pump process, all lasers will generate waste heat. Control of where this heat goes and how quickly it is removed is a vital part of the optomechanical design of all except the lowest power laser systems. Thus, the thermal misalignment (and thermo-optical effects) due to waste heat induced thermal gradients are most effectively controlled through proper design of heat sinking and active thermal management.

The second primary manifestation of thermal effects in laser performance is due to the temperature dependent properties of the optical elements in the laser resonator and associated optical system. There are many thermally dependent optical properties of optical elements used in laser systems. These thermo-optical properties of materials are most frequently studied in cases of thermal gradients across a given material. The most commonly thought of and measured thermo-optical property is the temperature-induced change of the refractive index (n) of an optical material (dn/dT). Variation in the refractive index of optical materials leads to changes in the phase of light passing though them. Gradients or inhomogeneities in the refractive index of an optical material directly result in changes to the wave front of light passing through the material. This can lead to wave front distortion, or (in the case of a radial temperature distribution in the optical material) thermal lensing. Many studies have been conducted on thermal lensing in laser systems and other alterations to the optical wave front that are caused by dn/dT [52, 53]. These effects can be minimized as mentioned previously, through proper mechanical design to allow for proper heat flow out of the laser system through heat sinking and active cooling techniques. The residual wave front error that cannot be removed from the system through proper mechanical design can often be corrected with adaptive optics [54].

While a great deal of attention has been paid to thermo-optical effects produced from waste heat induced temperature inhomogeneities in a laser system, little work appears to have been done relating to the mitigation of thermo-optical effects arising from the changing temperature of a laser system as a uniform whole. While this thermal issue is readily apparent

and can be a significant contributor to the variability of laser system performance over a range of operating temperatures, very little has been published about it [55, 56, 57].

This dissertation section will discuss experimental methods for athermalizing the output of laser systems with respect to fluctuations in overall system temperature and technologies related to them. Most importantly, the possibility of athermalizing laser systems through the use of passive elements in the laser resonator will be discussed. At present, the temperature dependent variation in the performance of laser systems is negated through active means such as stabilizing the temperature of the laser through use of conductive or convective cooling. This requirement of active temperature stabilization can greatly increase the weight, cost, and energy consumption of a fielded laser system. For this reason, the development of a passive technique or techniques to athermalize the output of solid state laser systems would be of great benefit, especially in portable, fielded laser systems that experience the full mil spec range of temperatures (-50 °C to 50 °C) while remaining as light and reliable as possible.

Active Athermalization of Solid State Lasers

The most obvious, and widely used, technique for ridding a laser system of temperature effects is to actively regulate the temperature of the system through cooling/heating. Many systems that involve significant pump power employ active cooling of system components such as the pump source and gain material. Active cooling helps mitigate thermal gradients in the system and also can be used to keep the system operating at a set temperature, removing any effect of the ambient environment.

However, active thermal management systems, such as the circulation of cooling water, can be bulky, add a great deal of weight to a laser system, and need power to run. In applications where lasers need to be light, portable, and utilize battery power, active thermal management systems can become highly impractical. For this reason, there is another potential method of active thermal management. An active control system could be implemented that monitors the temperature of the laser system and actively adjusts the amount of pump power/energy so that constant output energy is maintained. The basic premise of this method can be derived from the simple model for laser output is given in [50] describing the output power/energy of a laser as the product of a slope efficiency and the difference between the input power/energy and the threshold power/energy.

$$(24) \qquad P_{out} = \eta_{slope}(P_{in} - P_{th}) \qquad \text{or} \qquad E_{out} = \eta_{slope}(E_{in} - E_{th})$$

Differentiating this equation with respect to temperature (assuming that η_{slope}, E_{in}, and E_{out} are temperature dependent variables) results in the following equation.

$$(25) \qquad \frac{dE_{out}}{dT} = \frac{d\eta_{slope}}{dT}\left(E_{in} - E_{th}\right) + \eta_{slope}\frac{dE_{in}}{dT} - \eta_{slope}\frac{dE_{th}}{dT}$$

If the variation in output energy (E_{out}) is set to zero, the following condition for the rate of change in input energy (E_{in}) with respect to temperature (T) can be found.

(26) $$\frac{dE_{in}}{dT} = \frac{dE_{th}}{dT} - \frac{1}{\eta_{slope}} \frac{d\eta_{slope}}{dT} \left(E_{in} - E_{th} \right)$$

This shows that if the values of E_{th}, η_{slope}, and their temperature derivatives can be calculated or empirically measured for a laser system, a controlled change in the input energy with a given change in temperature can athermalize the output energy of the system.

Theoretical Techniques for the Passive Athermalization of Solid State Lasers

Two techniques have been proposed in the literature for passively athermalizing the output of a laser system. Both techniques are predicated on the use of Volume Bragg gratings (VBGs) as an element in the laser resonator. Before discussing the techniques in any detail, it is important to first discuss the properties and applications of VBGs.

Introduction to Volume Bragg Gratings

Volume Bragg gratings (VBGs) have become a valuable tool in the optics community in recent years. VBGs are holographic phase gratings written in bulk glass. A system of periodic planes exhibiting refractive index that is altered from the bulk value of the glass is created inside the bulk glass, resulting in diffraction of incident radiation. VBGs are typically used in a transmissive (TBG) or reflective (RBG) configuration. In the transmissive configuration, light passes though the VBG with some of the light diffracted out of the transmitted beam path. In the reflective configuration, light incident on the grating is diffracted at greater than 90 degrees to

the input direction, resulting in a diffracted beam that appears to be reflected from the grating. Figure 43 shows a diagram of both VBG configurations.

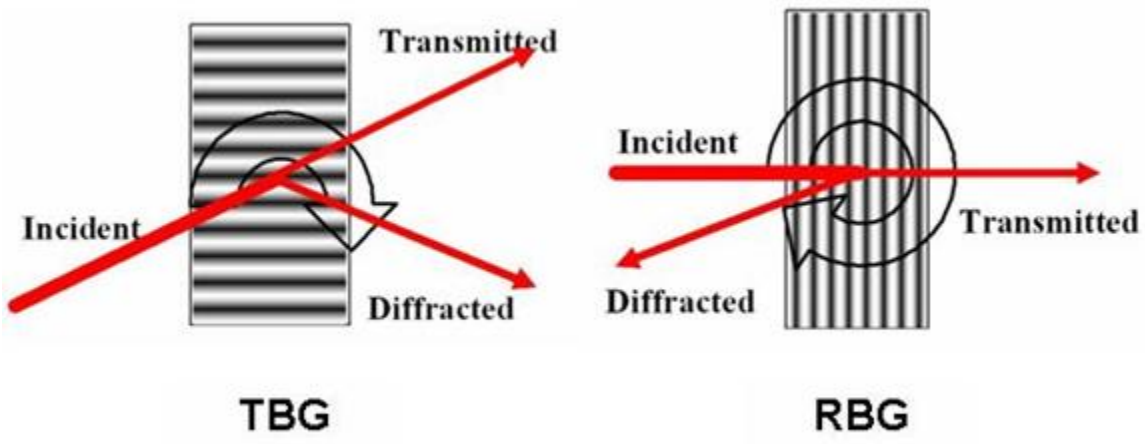

Figure 43 – Volume Bragg gratings can be configured for transmissive (TBG) or reflective (RBG) use. This figure is taken from Optigrate, Inc [59].

VBGs work on the same basic principle of diffraction and interference as that Sir William Lawrence Bragg discovered for X-rays due to crystal planes in 1912. Light incident on the planes of alternating refractive index inside of the bulk glass result in diffraction effects just as that described in a standard phase grating [60]. Diffraction is greatest when the grating and incident light hold to the Bragg condition:

$$\vec{K} = \vec{k}_f - \vec{k}_i \tag{27}$$

Where K is the grating vector, k_f is the final (diffracted) wave vector and k_i is the incident wave vector. Light with wavelength and direction satisfying the Bragg condition for a given grating will experience diffraction by the VBG. Since the VBG contains a sinusoidal phase grating, all diffracted energy is into the first diffracted order of the grating. \

VBGs are created by first exposing a special type of glass, known as photo-thermal refractive (PTR) glass, to UV radiation. By interfering two UV laser sources, a series of plane parallel interference fringes can be created inside the PTR glass. These areas of high intensity cause ionization of doped cerium in the glass. This results in the freeing of electrons, which are captured by doped silver ions. This causes the silver ions to become neutral silver atoms. When developed through heating, the neutral silver atoms diffuse rapidly, leading to the formation of microscopic silver crystals in the exposed areas of the glass. Under heating, the silver crystals act as nucleation centers for sodium and fluoride ions that then form NaF crystals. The presence of these crystals leads to a slight change in the local refractive index of the PTR glass. The net result is the formation of alternating index Bragg planes inside the developed glass. These features have been found to be stable under a variety of incident radiation and at temperatures up to 400 °C [61].

VBGs have many highly useful properties. They are much more physically rugged than standard diffraction gratings, making them highly desirable from a system-engineering standpoint. Since the gratings are bulk glass, they also have very high damage thresholds, bordering on that of fused silica optics [62]. The gratings can also be developed with multiple internal sets of grating planes, placed a various angles to each other [63, 64]. Diffraction efficiency in the gratings can be very high, with production gratings having diffraction

efficiencies higher than 99%, with very low absorption and internal scattering [65]. The high spatial resolution of the gratings results in very sharp spectral resolution, with FWHM of the diffracted order of only 0.25 nm or less [59].

The properties of VBGs make them highly desirable for many uses in the optics community. When used as a simple end reflector in a solid state laser cavity, they can lead to significant reduction in the linewidth of the laser radiation, and can even be used to select specific longitudinal modes for lasing [66]. Due to their high damage threshold, they also have been considered for potential use in spectral beam combining of high power laser systems [62]. They also have been used to tune broadband laser systems and have even been used as temperature tuned variable reflectors for laser systems.

Passive Athermalization through Narrow-Band Selection of Emission Wavelength

The first proposed technique for passively athermalizing a solid state laser system was proposed in a paper by Koroshetz et. al. [56]. Spectroscopy has shown that the stimulated emission cross-section curve of erbium doped glass when viewed at multiple temperatures, displays specific wavelengths where the cross section value does not change with temperature. Previous research [55] showed that the driving variable in the temperature dependence of the output of neodymium doped lasers was the temperature dependence of the stimulated emission cross section. It stands to reason that if an Er:glass laser were constrained to lase at one of the newfound temperature independent points in the cross section curve by implementing a reflective VBG as a cavity end

mirror, the laser output can be athermalized. This technique also has the potential to be extended to other gain materials that exhibit similar behavior of their stimulated emission cross-section.

The following sections detail the specifics of erbium glass and its use as a gain material, as well as developing the mathematic theory behind this type of proposed passive athermalization technique.

Introduction to Erbium Glass

Erbium doped glass lasers are highly useful due to their direct emission in the 1550 nm "eye-safe" radiation band. This band corresponds to absorption bands in the vitreous humor of the human eye, greatly reducing the amount of laser radiation incident on the eye that reaches the eye's sensitive retinal tissue [67]. For this reason, "eye-safe" lasers are highly desirable for open beam applications where the potential exists for unintended exposure of unprotected eyes. This includes applications such as range finders, target designators, and LIDAR [68, 69]. Its direct emission in the "eye-safe" band (> 1.4 μm) gives erbium doped glass an efficiency advantage over lasers with output converted to this band through use of OPO's or Raman cells. However, one potential shortcoming of these lasers is a large variation in output power of the laser with change in the temperature of the glass host material. This makes it difficult for a manufactured laser to meet a customer's output specification over a wide range of ambient temperatures without the use of temperature stabilization of the gain medium. While this problem is known within the laser engineering community, little research has been done on the effects that the variation of the temperature of a gain medium and surrounding components has on a laser's output power [86].

Erbium Glass as a Gain Material

The first lasing of the Er^{3+} ion was reported by Kiss et. al. [70] in 1962 when their group at RCA Laboratories measured "Optical Maser Action in Erbium Doped Calcium Tungstate ($CaWO_4$)", a tetragonal crystal once used for imitation diamond jewelry. The Er^{3+} ion is normally considered to be a three-level system in terms of laser action, meaning that the laser transition is between an excited state and the ground state of the ion. These systems typically have high threshold energies due to the requirement of exciting greater than half of the ions out of the ground state in order to reach the threshold condition.

Since erbium has little absorption of optical flashlamp pump energy, the Kiss group needed to cool the Er^{3+}:$CaWO_4$ to liquid nitrogen temperatures (77K) to deplete the upper stark levels of the ground state and create what is effectively a four-level system (known as a quasi-three level system) by lasing from the excited state to the thermally unoccupied upper level of the ground state manifold (375 cm^{-1} above the lowest energy ground state). This resulted in laser output at 1.61 μm. Due to the small number of available pump lines and the resulting need to greatly cool the system to obtain lasing, the system was not considered to be of great potential for future use.

In 1965, a significant change in the pump methodology allowed Snitzer and Woodcock [71] to demonstrate lasing of Er^{3+} ions in a silicate glass at room temperature. Their glass used Yb^{3+} ions as a co-dopant, creating a strong absorption at around 970 nm, corresponding to the $^2F_{7/2}$ to $^2F_{5/2}$ transition in Yb. The excited Yb ions could then transfer energy to the $^4F_{11/2}$ level of

Er^{3+} which would then relax to the long lived $^4F_{13/2}$ state, allowing for creation of a population inversion between the $^4F_{13/2}$ and $^4F_{15/2}$ Er^{3+} states. Figure 44 shows a simplified energy level diagram of the Yb^{3+} - Er^{3+} system.

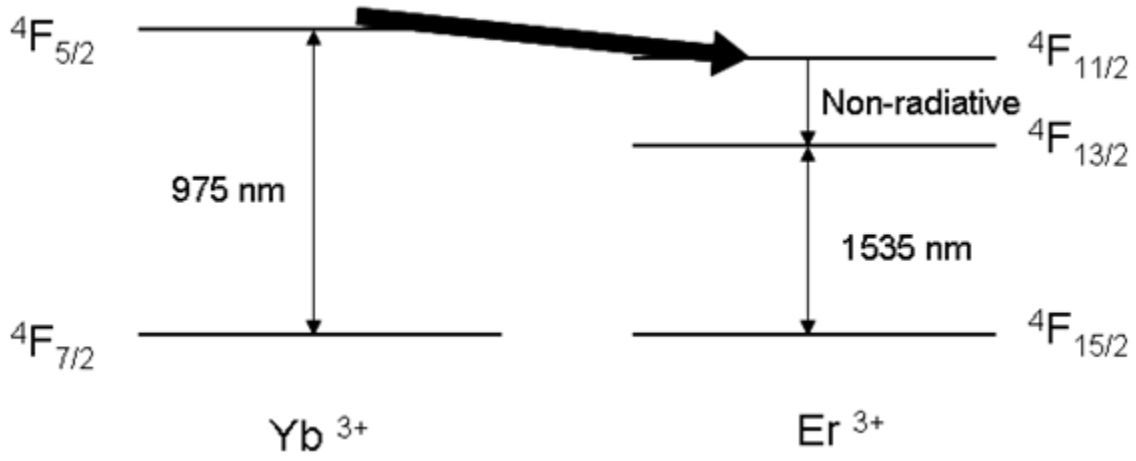

Figure 44 - Simplified Energy Level Diagram of Yb^{3+} - Er^{3+} Glass

While the co-doping of Erbium and Ytterbium in glass resulted in increased pump efficiency (allowing for flashlamp pumped, room temperature lasing), there were still problems with the Yb^{3+} - Er^{3+} pump scheme. While suitable for the more recent advent of diode pumping [72], the ytterbium absorption at 975 nm still has little overlap with the broad-band, blackbody-like, spectrum produced with flashlamp pumping. Additional development of Er:glass gain material from Snitzer's experiment has been in two primary areas: improvement in emission cross-section and mechanical properties of the glass and addition of sensitizing elements to the glass to increase flashlamp pump efficiency.

The emission cross-section in Yb^{3+} - Er^{3+} glasses has been increased and mechanical properties have been improved through the use of phosphate glasses instead of the older silicate glasses as ion host materials [73]. One inherent problem with recent generations of phosphate glasses has been the water solubility of the glass. While the glasses are not highly soluble in water, they do slowly dissolve when kept in extended contact with water (losing 0.08 percent of weight in one hour of exposure to 100 °C water per Kigre's data sheet). This has made water cooling of the materials somewhat problematic with long term operation. Newly developed glasses (Kigre QX glasses) reduce this water solubility by a factor of two [74] allowing for greater leeway in pump cavity design.

To combat the small overlap between the optical pump spectrum of a typical Xenon flashlamp and the absorption band of Yb^{3+}, sensitizing elements can be added to the glass to increase the pump absorption. The most typical of these are Nd^{3+} (used in Kigre QE-7 glass) and Cr^{3+} (used in QE-7S glass) [75]. The introduction of chromium in particular introduces broad absorption bands in the visible wavelengths, greatly increasing the overall pump absorption. Figure 45 shows the absorption cross-section curve for Kigre QE-7S glass and Figure 46 shows a simplified energy level diagram of a Cr^{3+}- Yb^{3+} - Er^{3+} glass system.

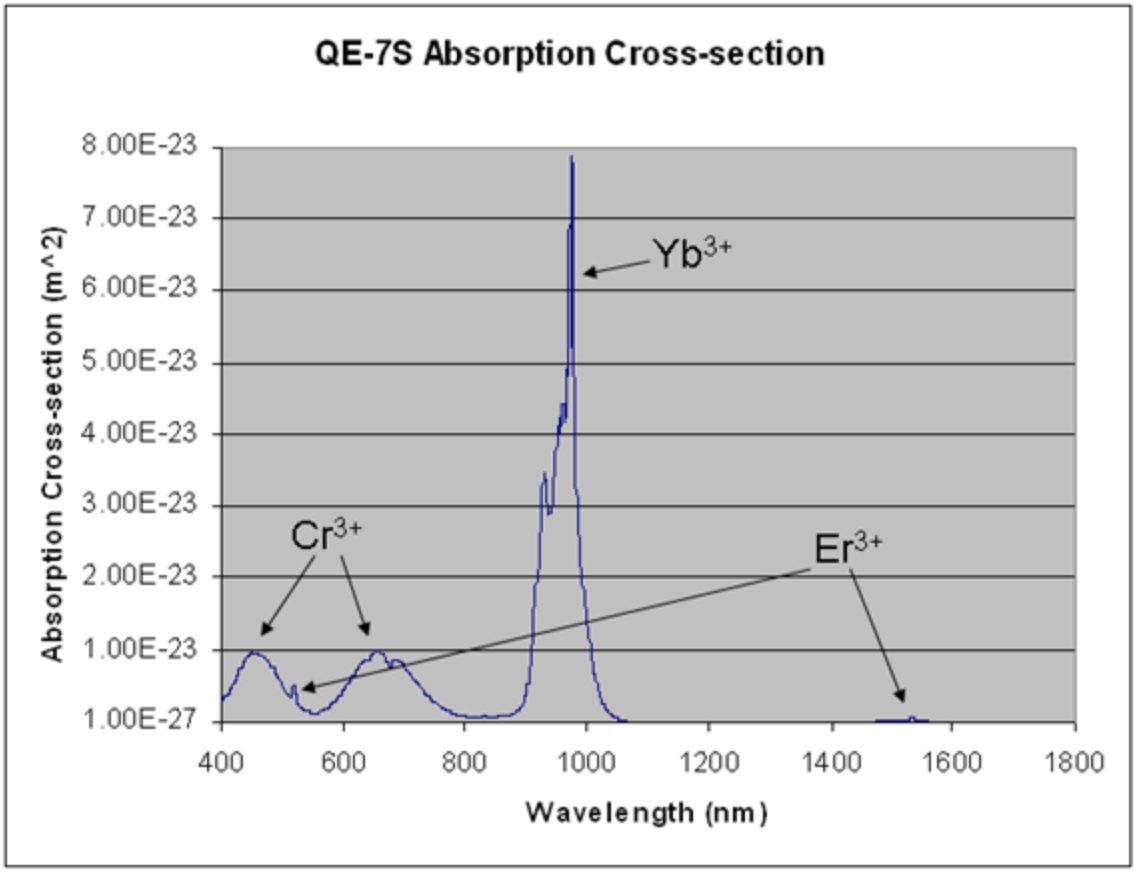

Figure 45 – Absorption Cross-section of Kigre QE-7S glass (data supplied by Kigre, Inc.)

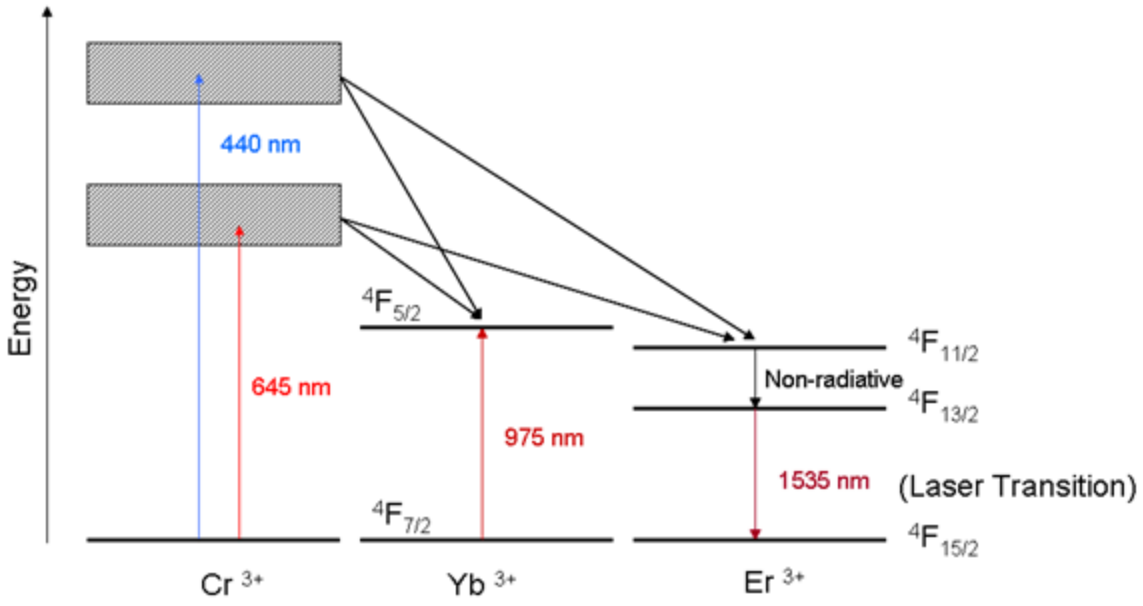

Figure 46 - Simplified Energy Level Diagram of Cr,Yb,Er:glass

Quasi 3-Level Nature of Er:glass systems

Erbium is by nature a three-level system, lasing between the $^4F_{13/2}$ excited state and the $^4F_{15/2}$ ground state. However, in reality, these levels are each split into manifolds of sub-states that can interact thermally. Studies of the Stark level splitting have been conducted in several glass types [76, 77, 78]. These studies show that the variability seen in the emission cross-section of Er:glass is due to the relative thermal population and transition probabilities of transitions from the multiple Stark levels in the excited state to the manifold of Stark levels in the ground state. Figure 47 shows a diagram of the Stark levels discussed in [76]. In addition, the resulting temperature dependent emission cross-section curves are shown in Figure 48.

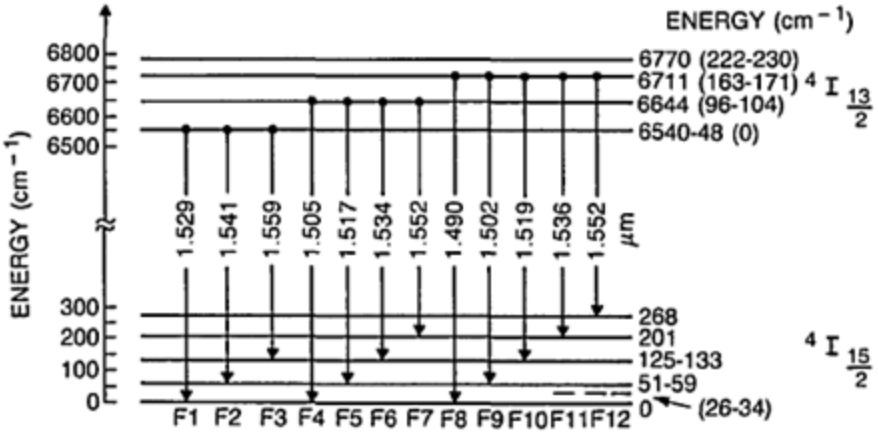

Figure 47 - Stark Level Splitting in Er:glass (from [76])

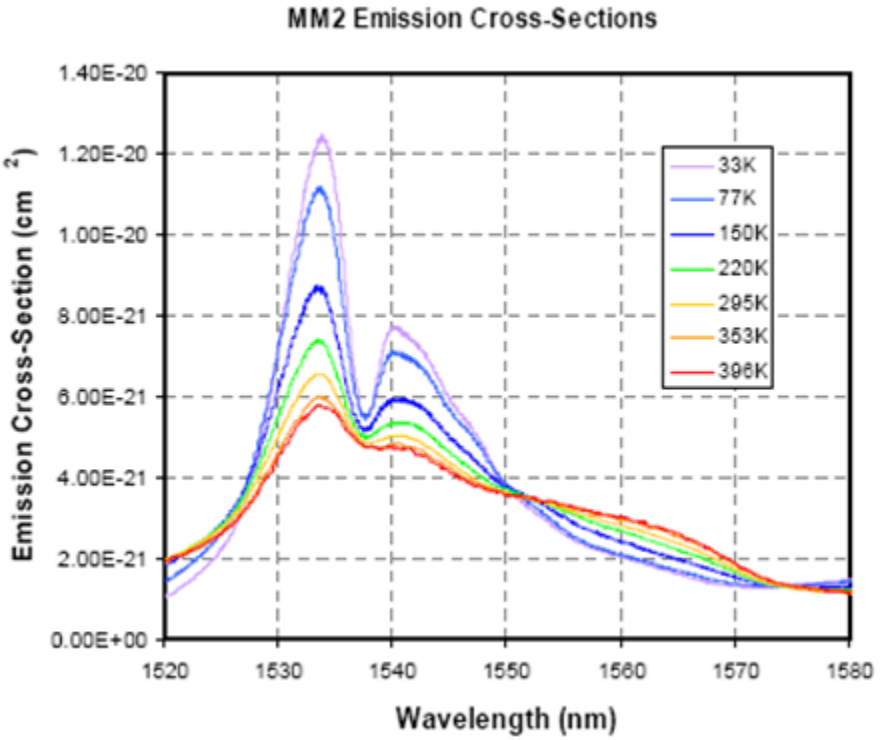

Figure 48 - Temperature Variability in Emission Cross Section Driven by Thermal Population of Ground and Excited State Stark Levels (From ref [56])

At very cold temperatures, the upper energy levels of the ground state (and excited state) become thermally depopulated. This allows for easy population inversion from the lower, highly populated, excited state Stark levels, to the upper, un-populated, ground state Stark levels. The result is a quasi-three level system, which behaves much like a four-level system with an un-populated lower level involved in the laser transition, but still technically lasing to the ground state as in a three-level system.

Development of CW Output Expressions from 3 and 4 Level Rate Equations

The most basic place to start in any analysis of laser performance is with the laser rate equations [50]. In a solid state laser system, a population inversion must be created by exciting ions in the gain material from an initial energy state (E_0) to more energetic excited states (E_{pump}). These ions then relax into a long-lived excited state (E_2). A population inversion exists when the population of E_2 becomes greater than the population of a lower energy state (E_1) with an allowed optical transition from E_2 to E_1. A laser is deemed to be a three-level system if the lower energy state is in fact the initial ground state. A system is considered to be a four-level system if the E_1 state is separate from the ground state and with much shorter lifetime than E_2, yielding a bottom state in the optical transition which remains effectively unpopulated. The term "quasi three-level" is often used to denote a system in which the lower energy state of the transition is a state or manifold of states that are close in energy to the ground state and can become thermally populated with ground state electrons. Equation (28) is the standard rate equation for the population density of the upper state of the transition.

(28) $$\frac{dn_2}{dt} = \phi\, c\sigma_{21} n_1 \left(g_2 / g_1 \right) + W_{pump} n_0 - \phi\, c\sigma_{21} n_2 - n_2 / \tau$$

Here n_2 and n_1 are the population densities of the upper and lower states of the transition, φ is the photon density in the mode at the lasing wavelength, g_2 and g_1 are the degeneracies of the upper and lower states, W_{pump} is the pump rate from the ground state to the pump band due to external pumping, σ_{21} is the emission cross section of the gain material at the lasing wavelength, τ is the lifetime of the upper state, and c is the velocity of light in the gain medium. Equations (29) and (30) give the total ion density of the gain medium and the population inversion in the medium, respectively.

(29) $$n_{tot} = n_0 + n_1 + n_2$$

(30) $$n = n_2 - n_1 \left(g_2 / g_1 \right)$$

By substituting equations (29) and (30) into equation (28), an expression can be found for the equilibrium population inversion (corresponding to when equation (28) is equal to zero and the state populations remain fixed in a CW output regime). In a four level system n_1 can be considered zero for low pump levels and in a 3 level system $n_1 \equiv n_0$ (thus changing (29) to equation (31), shown below).

(31) $$n_{tot} = n_1 + n_2$$

This results in the population inversion relations for three level systems (32) and four level systems (33).

(32) $$n = n_{tot}\frac{W_{pump} - (\gamma - 1)\frac{1}{\tau}}{W_{pump} + \gamma\phi\, c\sigma_{21} + \frac{1}{\tau}}$$ (three level)

(33) $$n = n_0\frac{W_{pump}}{\phi\, c\sigma_{21} + \frac{1}{\tau}}$$ (four level)

The variable γ is used to represent the quantity $(1+g_2/g_1)$. An expression for the population inversion can also be obtained from looking at the equilibrium between gain and loss in the laser resonator. It can be readily seen that the output of a laser will remain in equilibrium when the round trip loss in the laser resonator is equal to the round trip gain. Expressions for loss and gain are given in equations (34) and (35).

(34) $$loss = L - \ln(R) = \ln\left(e^{2\alpha l}(1-R)\right)$$

(35) $$gain = \ln(e^{2\sigma_{21}nl}) = 2\sigma_{21}nl$$

Here α is the single pass loss coefficient in the resonator due to absorption, scatter, and Fresnel losses at surfaces, R is the reflectivity of the output mirror, and l is the length of the gain medium. Solving for n produces equation (36).

(36) $$n = \frac{L - \ln(R)}{2\sigma_{21} l}$$

Equating (36) with either (32) or (33), the expressions for output power for three and four-level systems are:

(37) $$P_{out} = \frac{(1-R)}{(1+R)} \frac{2(1-L_N)\eta}{(L-\ln(R))\gamma} \left[P_{in} - \frac{h\nu}{\eta\tau} \left(\frac{L_N + (\gamma - 1)}{1 - L_N} \right) \right]$$ (three-level)

(38) $$P_{out} = \frac{(1-R)}{(1+R)} \frac{2\eta}{(L-\ln(R))} \left[P_{in} - \frac{L_N N_{tot} h\nu}{\eta\tau} \right]$$ (four-level)

In these expressions, ν is the frequency of laser oscillation, N_{tot} is the total number of ions in the mode volume, η is a unit-less factor related to the pump efficiency of the system, and L_N is a unit-less ratio of the resonator loss to the un-pumped double pass absorption of the gain material at the lasing wavelength as shown in equation (39).

(39) $$L_N = \frac{L - \ln(R)}{2\sigma_{21} n_{tot} l}$$

Both of the equations for output power can be written in the form of equation (40).

(40) $$P_{out} = \eta_{slope}(P_{in} - P_{th})$$

The slope efficiency of a three-level system is then given in equation (41) and a four-level system in equation (42). For a long pulse laser where the output energy is simply the output power multiplied by the time duration of the pulse (t_{pulse}), the threshold energies for three and four-level systems are given by equations (43) and (44), respectively.

(41) $$\eta_{slope} = \frac{(1-R)}{(1+R)} \frac{2(1-L_N)\eta}{(L-\ln(R))\gamma}$$ (three level)

(42) $$\eta_{slope} = \frac{(1-R)}{(1+R)} \frac{2\eta}{(L-\ln(R))}$$ (four level)

(43) $$E_{th} = \frac{t_{pulse} h\nu}{\eta\tau} \left(\frac{L_N + (\gamma - 1)}{1 - L_N} \right)$$ (three level)

(44) $$E_{th} = \frac{t_{pulse} L_N N_{tot} h\nu}{\eta\tau}$$ (four level)

Temperature Dependence of Output Variables

The rate of change of the output energy of a system with respect to temperature can be readily calculated by taking the derivative of the output expressions derived in the previous section with respect to temperature. While this is a straightforward mathematical step, care must be taken in determining which variables in the output expressions are functions of temperature. Prior research [55], examining the temperature dependence of flashlamp pumped, Nd^{3+} doped material, found that the only variable with significant temperature dependence was the emission cross section of the gain material (σ_{21}). Furthermore, only the threshold energy (not the slope efficiency) was a temperature dependent term (assuming the pump efficiency is constant over temperature due to the broadband blackbody spectrum of the flashlamp pump source). Thus, the temperature derivative of (40) (multiplied by the pulse duration to convert to pulse energy) is given by:

$$\frac{dE_{out}}{dT} = -\eta_{slope}\frac{dE_{th}}{dT} = \frac{\eta_{slope}E_{th}}{\sigma(T)}\frac{d\sigma}{dT} \tag{45}$$

Equation (45) implies that if a system can be found that has a constant emission cross section with respect to the temperature of the gain material, the system can by expected to have an athermal output. However, this might hold true only for a four-level system. In a three-level system, especially a quasi-three level system such as Er:glass, the thermal behavior of the output energy may become more complex. For a three-level system, the slope efficiency (not just the threshold energy) is also a function of emission cross section. In addition, for a three-level

system, both slope efficiency and threshold energy are a function of the degeneracy factor γ. In a quasi three-level system, the ground state is made of a manifold of levels with slightly differing energies. At high temperatures, these levels may be considered to be equally populated and the degeneracy of the ground state can be considered equal to the total number of sub-states in the ground state manifold. However, decreasing the temperature will actually decrease the effective degeneracy of the ground state as higher energy states in the manifold begin to lose their thermal connection to the ground state. Thus, the temperature derivative of (40) becomes much more complicated, resulting in:

$$\frac{dE_{out}}{dT} = \left[\frac{d\eta_{slope}}{d\sigma}\frac{d\sigma}{dT} + \frac{d\eta_{slope}}{d\gamma}\frac{d\gamma}{dT}\right]\left(E_{in} - E_{th}\right) - \eta_{slope}\left[\frac{dE_{th}}{d\sigma}\frac{d\sigma}{dT} + \frac{dE_{th}}{d\gamma}\frac{d\gamma}{dT}\right] \tag{46}$$

In the three-level case, having dσ/dT of zero is not necessarily sufficient to athermalize the output. However, there is a possibility that selecting a value of dσ/dT resulting in the dσ/dT terms in (46) having a sign opposite to the dγ/dT terms could result in a net cancellation of terms. Thus, the potential for temperature independent output energy exists even when other variables such as gamma exhibit temperature dependence in addition to the already known temperature dependence of emission cross-section.

Passive Athermalization through use of VBGs as variable reflectivity mirrors

The second technique for passively athermalizing a laser system was proposed by Chung et al [57]. This paper looks at the temperature dependence of the reflectivity of VBGs and uses this as

a motivation for theoretically determining what form of temperature dependent reflectivity is needed to produce an athermal output given the temperature dependence of the emission cross section of Nd:YAG. Since Nd:YAG is a four-level system, with simple temperature behavior of its emission cross-section (i.e. a narrow line spectrum and monotonic temperature dependence), the technique outlined previously will not work in this case.

Temperature Dependent Reflectivity of VBGs

In an earlier paper [79], Chung created a Ti:Sapphire laser using a reflective VBG for each end mirror in a standard X cavity. Heating one of the VBGs independently of the other caused a change in output reflectivity that can be understood by looking at the reflectivity curve of a reflecting VBG and the effect of temperature on the VBG structure.

The reflectivity of a VBG can be represented by the simple model of an ideal Bragg reflector. The diffraction efficiency of an ideal Bragg reflector (hence its effective reflectivity) can be calculated from the following system of equations:

$$R = \frac{(\kappa d)^2 \tanh^2 \sqrt{(\kappa d)^2 - (\delta d)^2}}{(\kappa d)^2 - (\delta d)^2 + (\delta d)^2 \tanh^2 \sqrt{(\kappa d)^2 - (\delta d)^2}} \tag{47}$$

$$\kappa = \frac{\pi \Delta n}{\lambda_0 \cos \theta_g} \tag{48}$$

(49) $$\delta = \frac{\pi}{\Lambda}\left(1 - \frac{\lambda_0}{2n_g \Lambda \cos\theta_g}\right)$$

Where R is the reflectivity of the grating, d is the length of the grating, Δn is the index difference induced by the holographic planes, n_g is the refractive index of the bulk glass, θ_g is the angle between the k-vector on the incident light and the normal to the Bragg planes after refraction into the glass, λ_0 is the wavelength of incident light in vacuum, and Λ is the wavelength of the grating structure. Figure 49 shows a plot of a typical Bragg grating reflectivity curve.

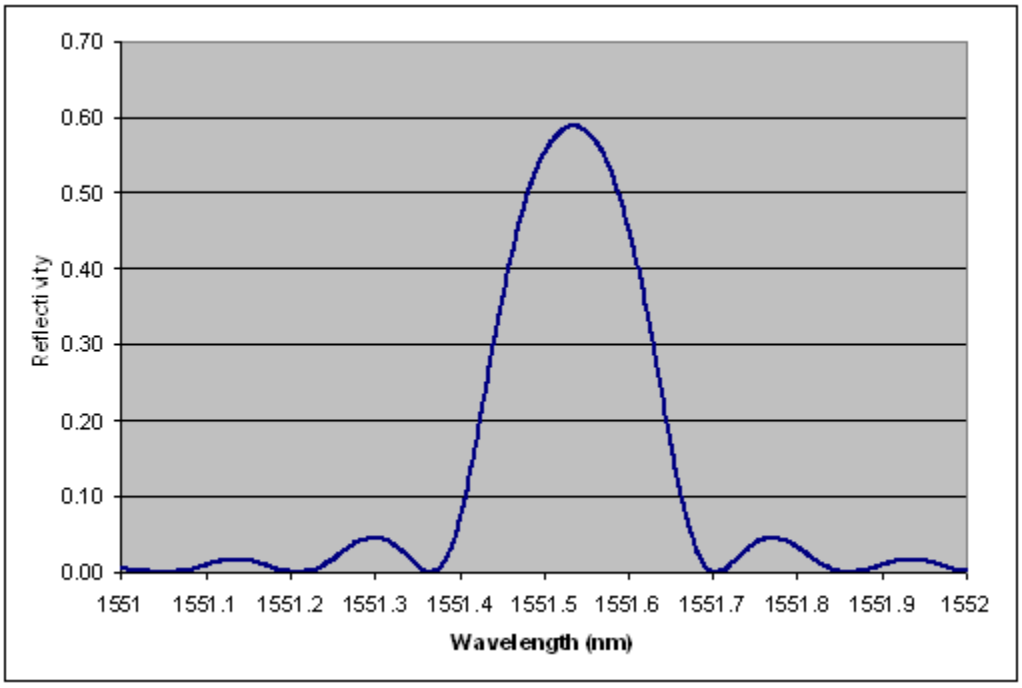

Figure 49 - Typical Bragg grating reflectivity curve arbitrarily centered at 1551.535 nm

As a VBG is heated, it undergoes thermal expansion as well as slight changes in refractive index due to dn/dT. Thermal expansion results in the plane-to-plane spacing of the

grating structure increasing, resulting in an increased Λ. This causes a shift in the center wavelength of the grating reflectivity curve to longer wavelengths when heated and shorter wavelengths when cooled. A series of calculated VBG reflectivity curves is shown for various temperatures in Figure 50.

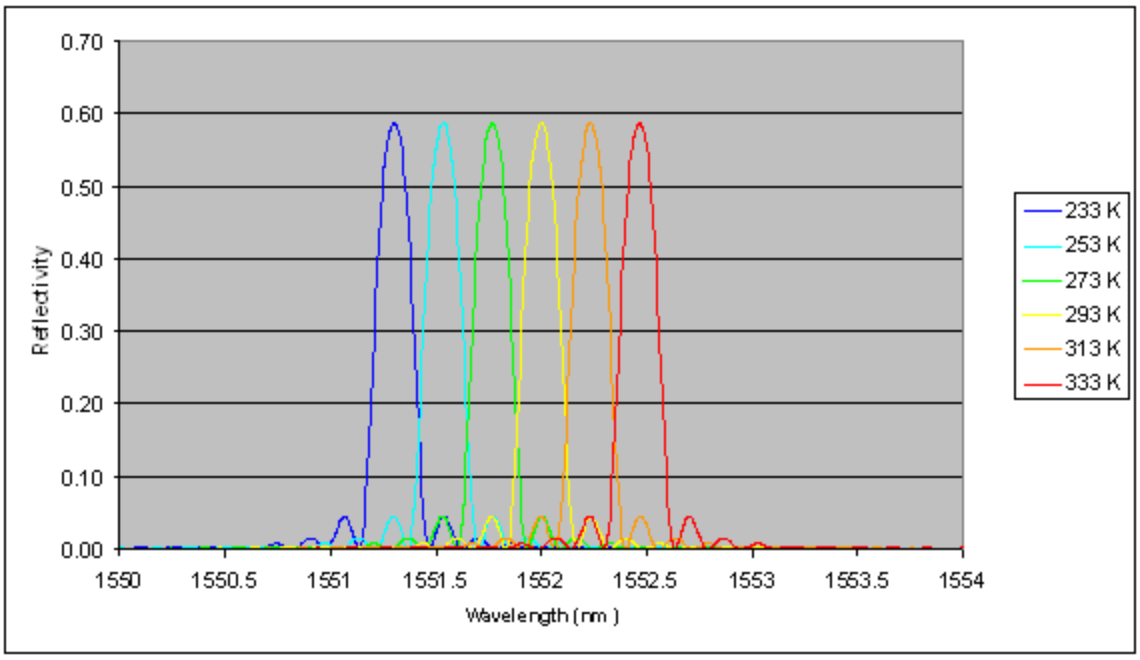

Figure 50 - Shift of VBG reflectivity curve with 20 C increments in temperature

By shifting the reflectivity of one grating with respect to that of another grating through temperature effects, the effective output coupling reflectivity of the system can be made to increase or decrease with increasing temperature based upon the initial relative spectral position of the two Bragg grating reflectivity curves. This is shown in Figure 51.

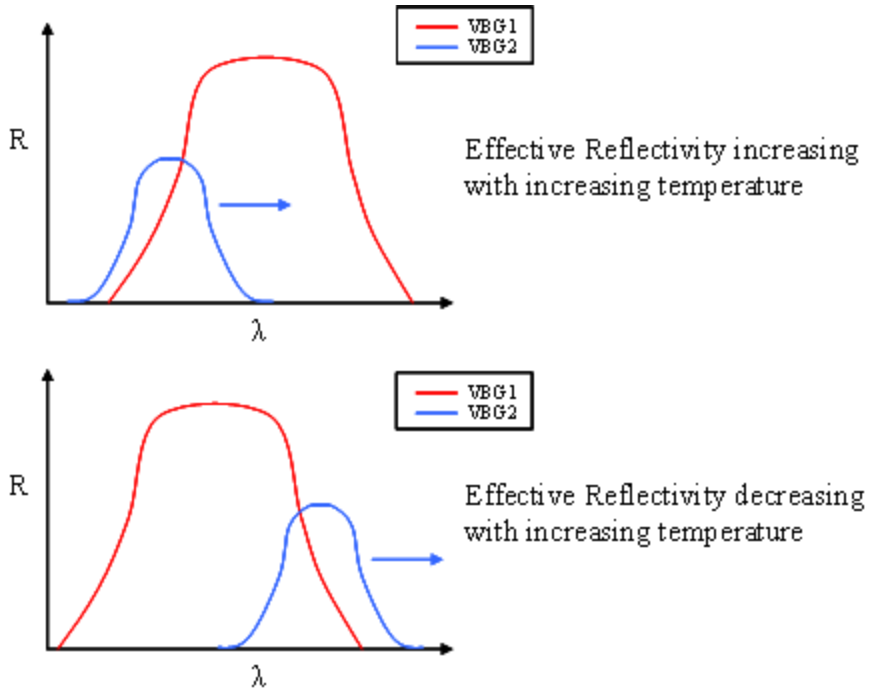

Figure 51 - Two VBGs resulting in shifting of effective reflectivity as VBG 2 shifts relative to VBG 1

Calculation of Needed Reflectivity Curves

By differentiating the laser output equation for a four-level laser derived earlier in this paper (38) with respect to temperature and assuming that only emission cross-section and output mirror reflectivity are temperature dependent variables, Chung et. al [78] created a plot, shown in Figure 52, of desired temperature-dependent reflectivity to athermalize different types of Nd:YAG lasers.

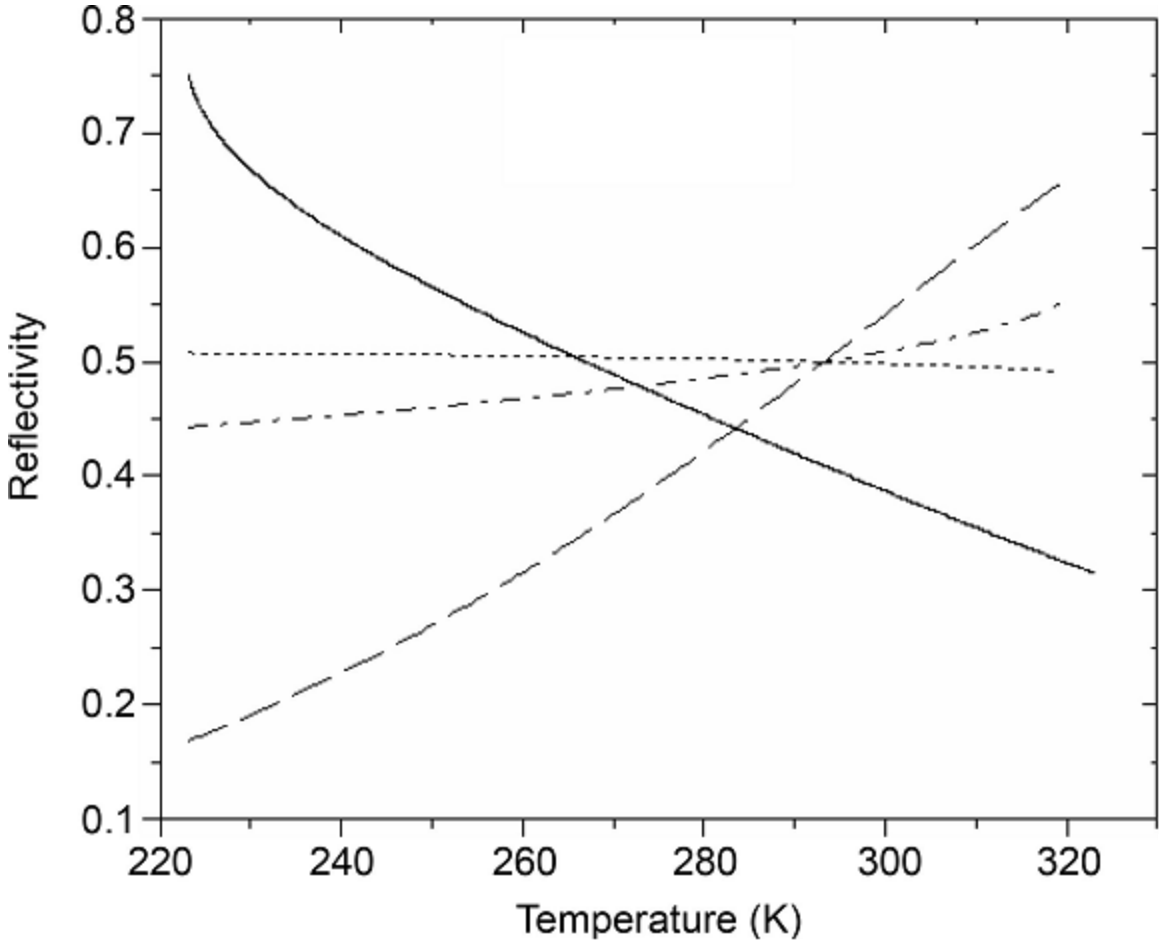

Figure 52 - Reflectivity needed to athermalize Nd:YAG laser. The dashed–dotted curve is for the case of long pulse operation, the dotted curve is for the case of an actively Q-switched laser with constant pump energy, the dashed curve is for the case of the actively Q-switched laser pumped to the ASE limit, and the solid curve is for the case of the Cr:YAG passively Q-switched laser. From [79]

Care must be taken to create Bragg gratings with a reflectivity curve shape that when shifted relative to each other the result is the needed reflectivity behavior.

Potential Problems and Solutions using this Technique

One potential hardship in implementing this athermalization method is in creating the needed shift of the reflectivity curve of one grating relative to another. In Chung's experiment, one grating was heated separately from the other to create this shift. However, in a real system both gratings will experience the same ambient temperature and the center wavelength of their reflectivity curves would move in lock step with each other. One potential solution to this problem is to create the gratings in slightly different PTR glasses with differing thermal expansion properties. This would need to be explored with grating manufacturers such as Optigrate, Inc.

Another potential idea is to use a single VBG and place the center of its reflectivity curve at a wavelength where the stimulated emission cross-section of the laser material varies rapidly with wavelength. While this would not affect the reflectivity of the VBG, it would result in a temperature dependent selection of emission cross-section at the allowed lasing wavelength. By using this induced temperature dependence in cross-section to counter the natural temperature dependent change in cross-section, a net temperature independent stimulated emission cross section could be achieved.

Experiment and Modeling

Initial Breadboard Testing

To test the emission wavelength selection technique of passive athermalization, an experimental breadboard setup was constructed. This breadboard consisted of a water cooled, flashlamp pumped, pump cavity containing a 80 mm long, 3 mm diameter laser rod of Kigre QE-7S laser glass (Cr,Yb,Er:glass). The rod was pumped by a 7.62 cm arc length xenon flashlamp with 450 Torr fill pressure. The pump chamber was connected to a variable temperature water chiller which controlled the temperature of the laser rod. Cavity end mirrors were mounted such that they were physically isolated from the pump cavity. This prevented the temperature variation of the rod and pump cavity from potentially causing a shift in the temperature of the mirror mounts and potential thermal misalignment of the laser resonator. Figure 53 below shows a diagram of this test setup.

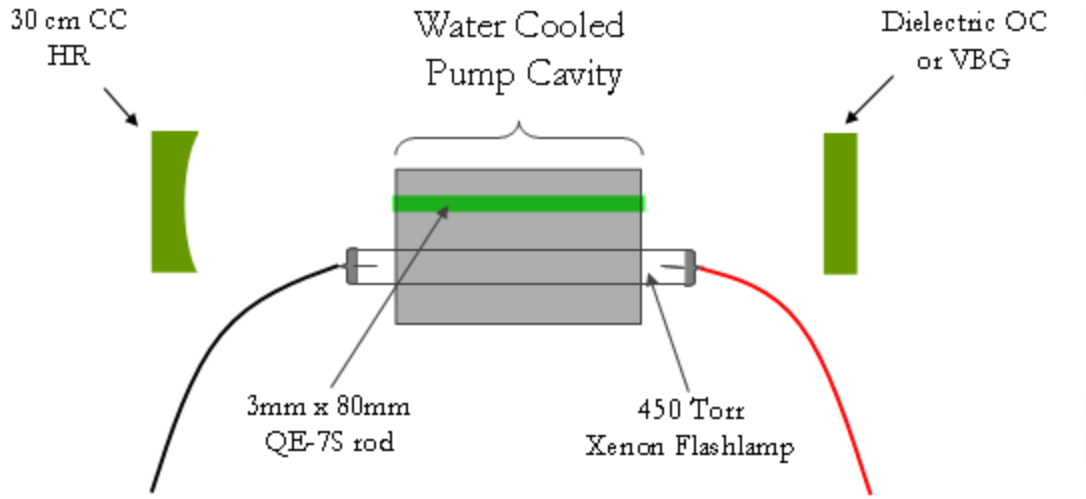

Figure 53 - Diagram of Temperature Testing Breadboard

The end mirrors of the cavity consisted of a 30 cm center of curvature high reflectivity dielectric coated mirror at one end and a series of flat interchangeable partial reflectivity output couplers at the other. The output couplers used in the initial testing were 99%, 98%, 95%, and 90% reflective dielectric coated mirrors, as well as a VBG centered at 1552.75 nm with a reflectivity of 98.9% [59]. Using this experimental setup, the temperature of the laser rod was varied from 10 °C to 30 °C in 5 °C increments through use of the programmable chiller. The output vs. input energy data for the system was measured at each temperature for each output coupler. The flashlamp was driven with a variable pulsewidth pulse forming network (PFN) set to its maximum possible pump duration of 800 μs and fired at a rep rate of only 0.02 Hz in order to assure that the rod remained in thermal equilibrium with the cooling water. The alignment of the system was checked prior to beginning any series of temperature increments and again when

the total temperature shift was completed in order to verify that no thermal misalignment occurred as the rod was cooled. The results are shown in Figure 54.

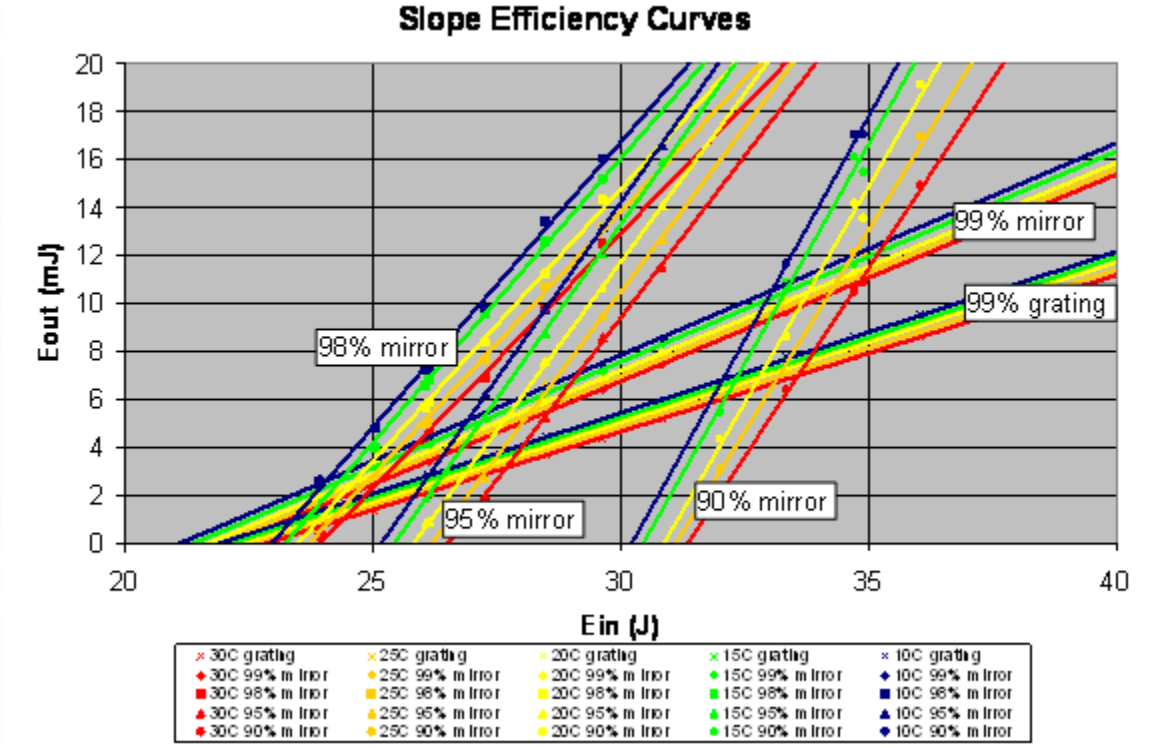

Figure 54 - Slope Efficiency curves for the long pulsed Cr,Yb,Er:glass laser using dielectric coated output couplers as well as a VBG. The output curve for each coupler was taken with rod temperatures of 10, 15, 20, 25, and 30 degrees Celsius.

Each set of lines in Figure 54 represents data taken for a given output coupler reflectivity. The blue lines represent a rod temperature of 10 °C and the red lines indicated a rod temperature of 30 °C, with the other colors representing 5 °C increments between the two extremes. As would normally be expected with a typical long pulsed solid state laser, the output performance of the laser improves as the temperature is decreased. All sets of lines regardless of output

coupler indicate a steady decrease in threshold energy with decreasing temperature. Interestingly, at lower reflectivities, a temperature dependent shift in slope efficiency can also be seen due to the three level nature of the Er^{3+} laser and the inclusion of emission cross section in the slope efficiency term.

The use of the VBG tuned to a temperature independent point in the stimulated emission cross section did not significantly change the temperature dependent variation in output energy as compared to that resulting from a dielectric mirror output coupler of equal reflectivity, as illustrated in Figure 54. However, lowering the reflectivity of the output coupler greatly increased the temperature variation in output energy seen for a fixed input energy. This is primarily due to the significance of the slope efficiency of the laser output in determining the temperature dependent variation in output. For a series of lines with a given spread in threshold energy, the range of output energies for a fixed input energy will increase as the slope of the set of curves increases. This concept is shown in Figure 55 below where a set of three bars of equal width are given differing slopes. As the slope of the bar increases, so does the spread in output energies that correspond to a vertical slice through the bar.

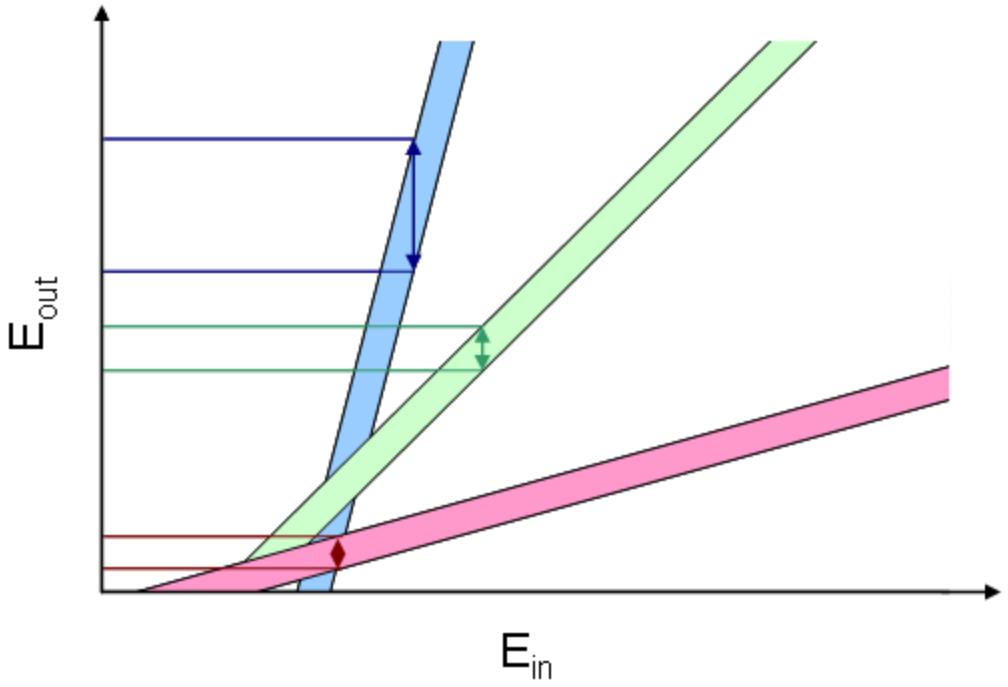

Figure 55 - Increase in output energy spread with increasing slope

Figure 56 is a plot of the rate of change in laser output energy with respect to temperature plotted versus slope efficiency. In this plot, a roughly linear relationship between slope efficiency and the temperature dependent change in output energy is observed. Thus, reducing the slope efficiency by a factor of two will result in halving the output variation as well.

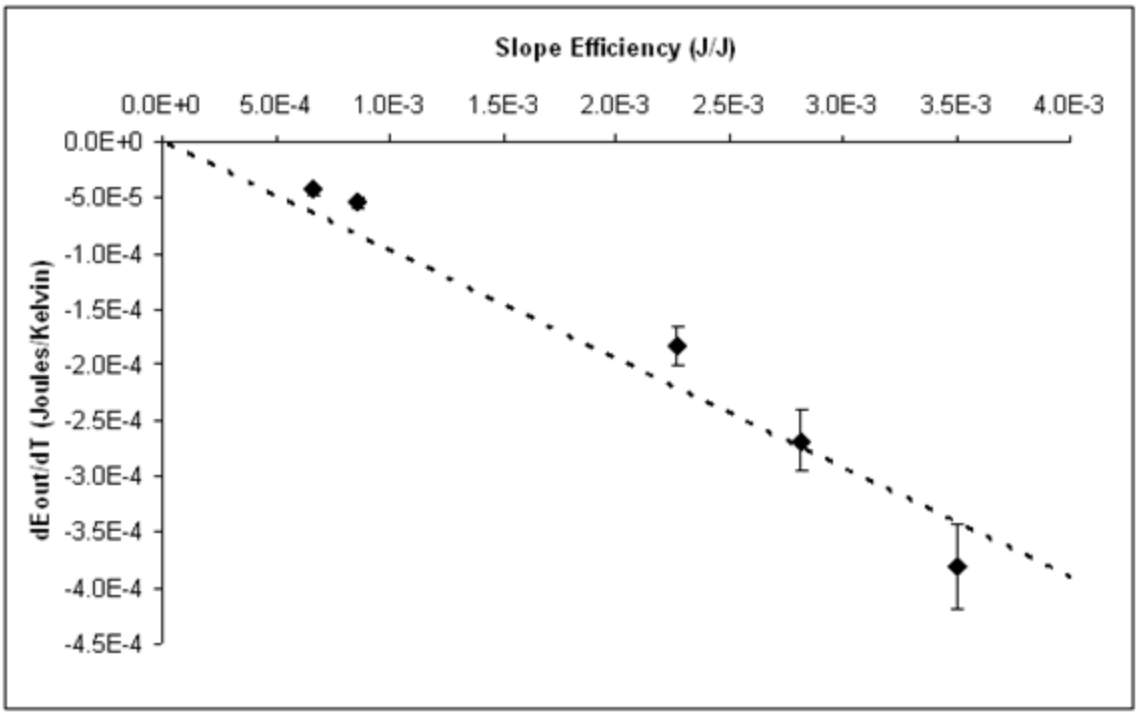

Figure 56 - Temperature Dependent Change in Output Energy vs. Slope Efficiency

This effect of slope efficiency on the temperature dependent output variation of the laser system can potentially be used to trade off laser efficiency for temperature stability. Figure 57 shows a plot of the input energy needed to produce an output pulse of 10 mJ at 20 °C (a rough measure of efficiency), as well as the full output variation seen over the temperature range of 10 - 30 °C for each output coupler used.

An example of a tradeoff can be seen by first looking at the 98% output coupler which exhibits the highest efficiency (the least input energy needed to produce 10 mJ of output). This coupler exhibited an output variation of a little more than 3 mJ when the temperature was varied from 10 – 30 °C. If a 99% output coupler were used instead, the energy needed to produce a 10

mJ output pulse would increase by approximately 18% (from 28 to 33 mJ). However, the output variation would decrease by a factor of 3 (from 3 mJ to 1 mJ), providing a potentially valuable increase in output temperature stability for a modest reduction in system efficiency.

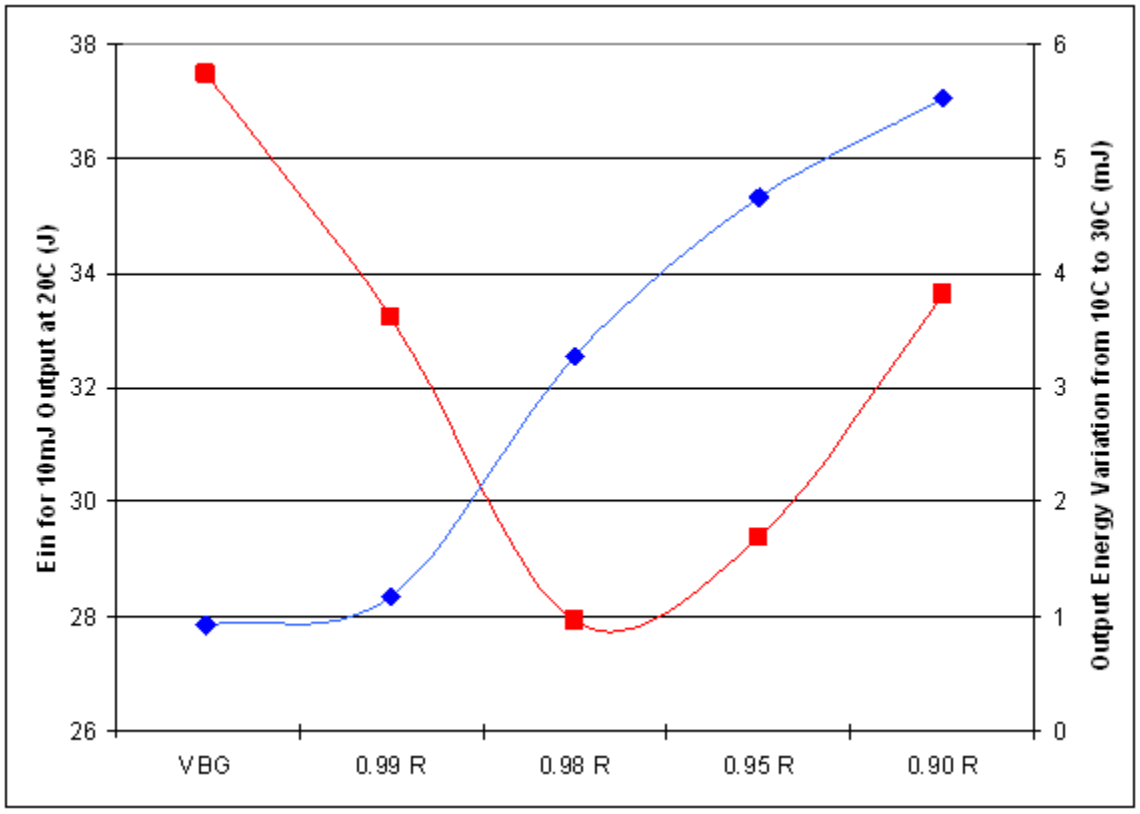

Figure 57 - Input energy needed to produce a 10 mJ output pulse at 20 °C from the Er:glass laser and the output variation due to temperature changing from 10 °C to 30 °C plotted versus the output coupler reflectivity.

Further Characterization of the Laser System

While tradeoffs made by altering the slope efficiency of the laser system can be useful, it is more desirable to create a truly athermal laser system. To more fully characterize the temperature variation in the laser system the long pulsed testbed was utilized in a new configuration, with the 99% diffraction efficiency Volume Bragg Grating (VBG) as a high reflectivity end mirror. This allowed the system to be held to an emission wavelength shown to correspond to a temperature invariant point in the emission cross section curve. A series of two meter radius of curvature output couplers with reflectivities of 99, 98, 95, and 90 % were used as the other cavity end mirror and the slope efficiency and threshold energy for each configuration was again measured. This data (plotted in Figure 58) again clearly showed that the temperature dependence of the system was not eliminated by the constraint of the emission wavelength to an athermal point of emission cross-section. The question remained as to what could be causing this temperature variation.

The pump efficiency (η_{pump}) of the system is expected to remain constant over the range of operating temperatures due to the fact that the broad black body spectrum of pump light produced by the flashlamp would negate any temperature induced spectral narrowing or shifting of the chromium pump bands in the gain medium. This was indeed the case in the Bass et. al [55] investigation of the temperature dependent output behavior of Cr,Nd:GSGG lasers.

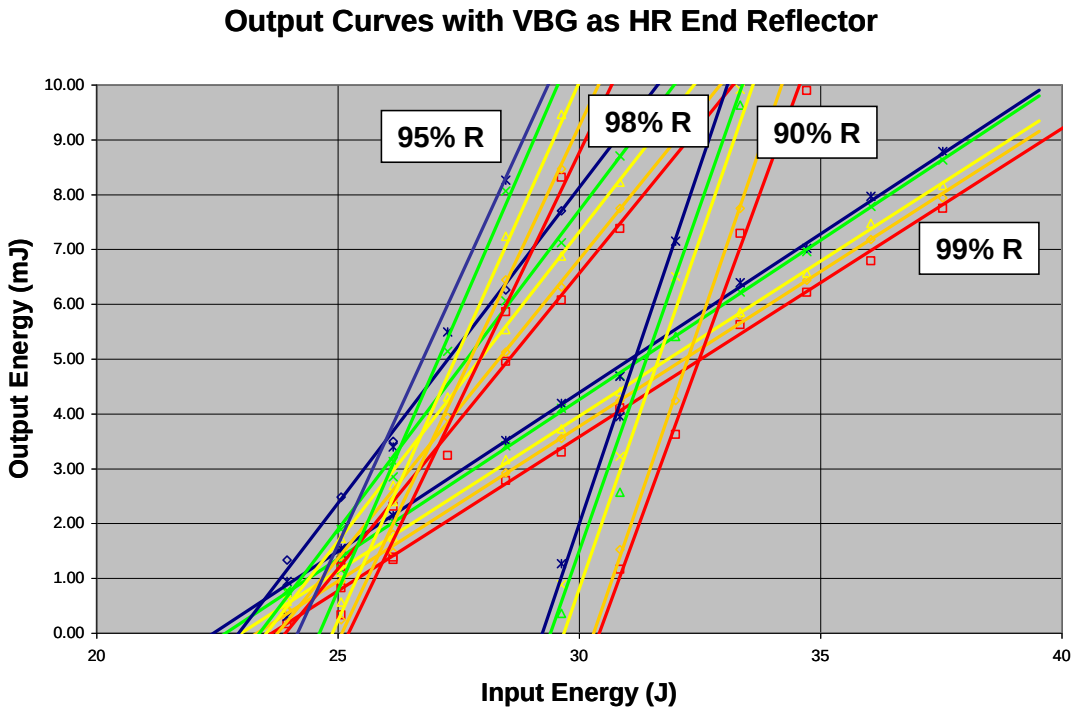

Figure 58 - Laser output curves generated using VBG as HR end reflector and varying dielectric output coupler reflectivity.

Attempts to determine the source of temperature dependence when the temperature dependent change in emission cross section had supposedly been eliminated proved problematic. Using equations (41-45) and the results from testing, the degeneracy factor (γ) and pump efficiency (η_{pump}) were calculated for each output coupler used. Figure 59 shows a plot of these results. For each output coupler reflectivity, two curves were plotted. One curve corresponding to the relation between pump efficiency and the degeneracy factor obtained through the equation derived for threshold energy (eq. 43), and the other to the relation between pump efficiency and the degeneracy factor obtained though the equation derived for slope efficiency (eq. 41). The

solution, corresponding to the intersection of the curves, is marked by a colored dot for each output coupler.

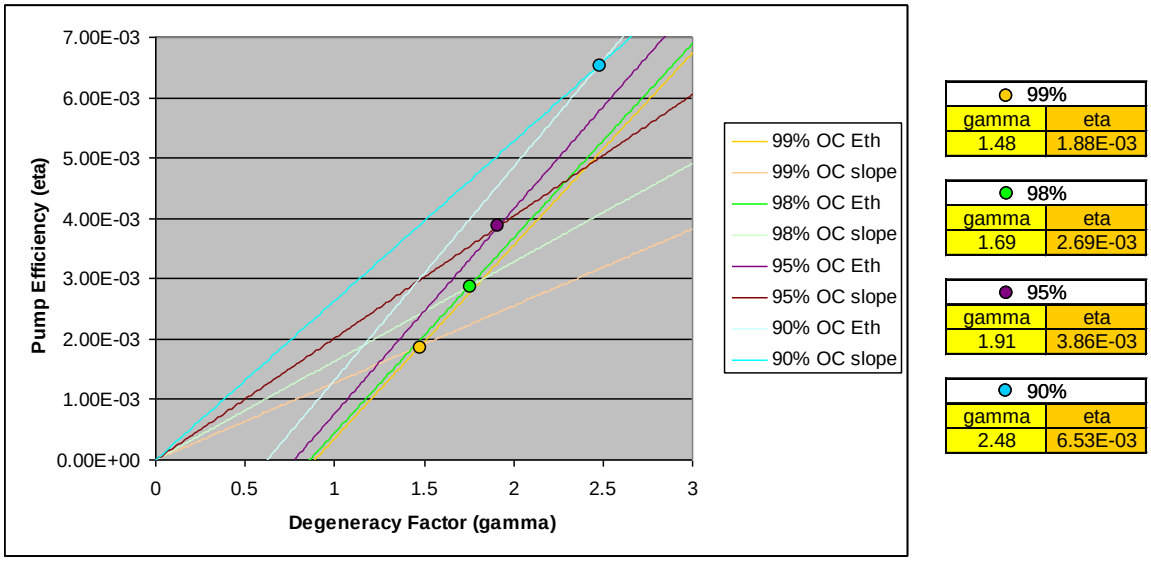

Figure 59 - Calculated pump efficiency and degeneracy factor for each output coupler reflectivity.

Theoretically, the output coupler reflectivity should not influence the results of these calculations since the effects of reflectivity are included in equations (41 and 43) that were used in the calculation. However, it can be clearly seen in Figure 59 that the results of these calculations show a systematic change in pump efficiency and degeneracy factor with output coupler reflectivity, even to the point of indicating a degeneracy factor greater than 2 which would not be expected. This strongly suggests that the explicit equations for a three-level system developed from the laser rate equations and shown in the theory section of this report are not fully valid for the laser system being tested.

Development of Time Dependent Rate Equation Model

Since the long pulse model, based on steady state laser operation, was not correctly modeling the experimental data, the temporal profile of the pump and laser pulses were explored. A silicon pin diode was used to monitor the flashlamp pulse and a InGaAs diode was used to monitor the output pulse of the laser. The resulting output was displayed on a digital oscilloscope and an example is shown in Figure 60.

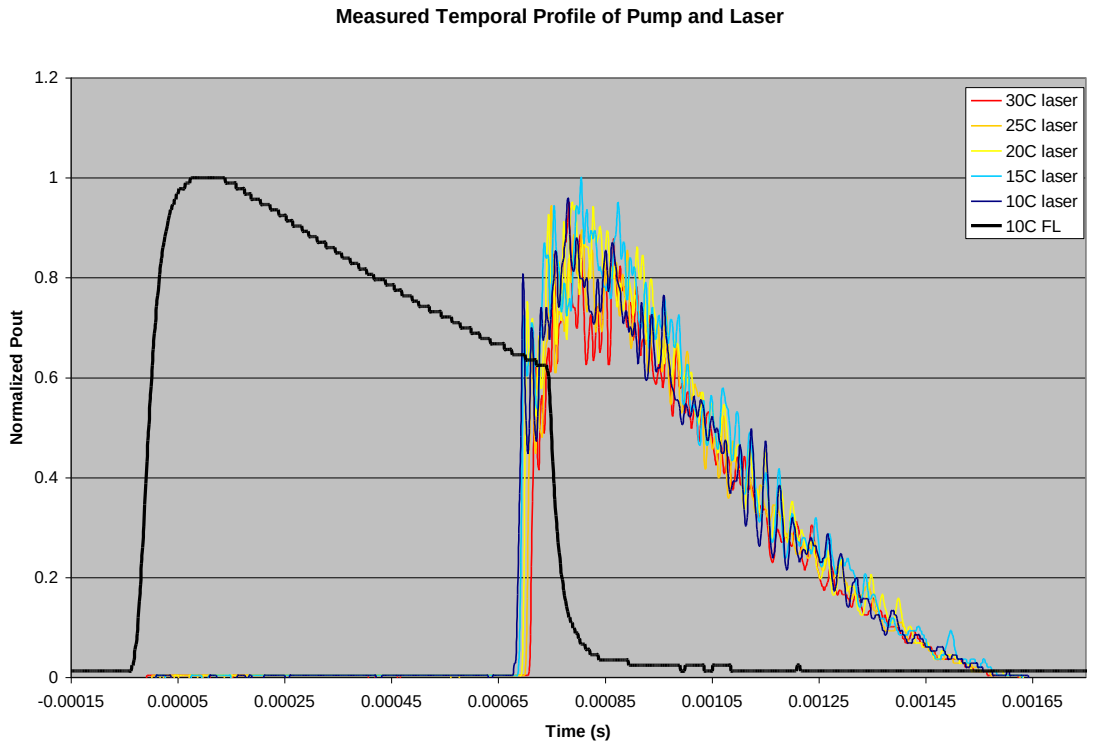

Figure 60 - Temporal profile of pump pulse and Er:glass laser output. The black line is the pump pulse and colored lines are laser output at several rod temperatures. This data was taken with a VBG with 99 % reflectivity at 1552.75 nm HR and a 99 % reflective, 2m CC, dielectric coated output coupler.

As shown in Figure 60 a substantial delay can be seen between the timing of the pump pulse and the onset of laser output. The laser output never reaches a stable output power and thus the laser is clearly not reaching steady state operation. For this reason, the steady state/long pulsed model for the laser output is invalid. This is likely caused by the short duration of the pump pulse (800 μs) as compared to the florescent lifetime of the erbium transition (8 ms). The laser never truly reaches steady state operation before the end of the pump pulse, rendering the basic assumptions behind the development of the equations for output energy invalid. Figure 61 shows the normalized temporal profile of the pump pulse and the output pulse power of the system for each of the four output couplers used.

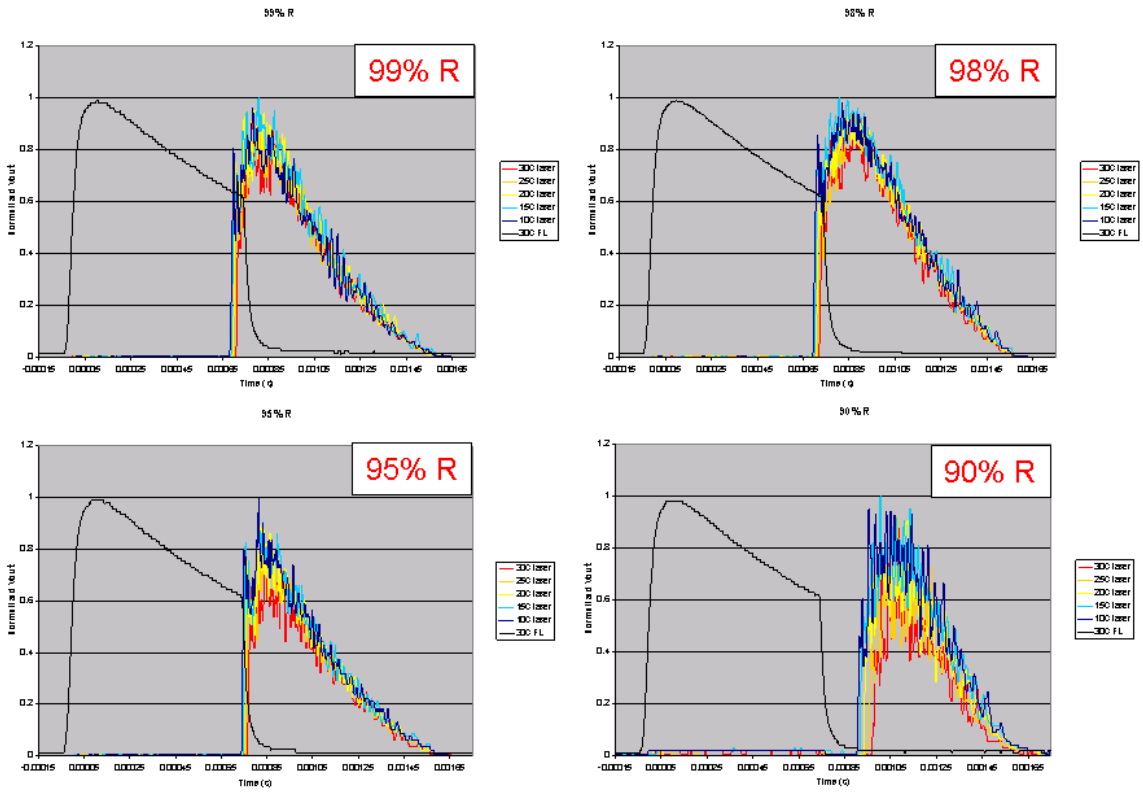

Figure 61 - Measured temporal profile of pump power and laser output power for 99, 98, 95, and 90 % reflectivity output couplers

The plots in Figure 61 show a substantial delay between the onset of the pump pulse and the beginning of laser action in the system. In the 90 % reflectivity case, the output pulse does not even begin to appear until after the pump is turned off. This is due to the combined effect of a pump level that is not a great deal above the threshold for lasing causing a long build up time before a large enough inversion is reached and the long energy transfer time from flashlamp pumped chromium^{3+} ions to the erbium^{3+} ions that participate in lasing. In addition to the overall delay in laser onset, the onset of lasing increases with increasing rod temperature while the end time of the pulse decreases. This causes a net decrease in output energy that acts in addition to temperature driven changes in the peak output power and the effect appears to become stronger

as the output coupler reflectivity is decreased. This reflectivity driven mechanism of change in output energy could explain the inconsistencies seen when using the steady state rate equation approach to modeling the system.

Rate Equation Integration Model

Due to the non-steady state operation in the laser system, a new approach was needed to accurately model the temperature dependence of the flashlamp pumped Er:glass laser. Rather than rely on explicit equations developed with the steady state assumption, computer algorithms were written in MATLAB to directly numerically integrate the laser rate equations governing the laser system and produce a theoretical model that could be used to test methods of output athermalization.

Kigre QE-7S is triply doped with Cr, Yb, and Er ions and a simplified energy level diagram was shown previously in Figure 4. Flashlamps primarily pump the chromium bands which, in turn, transfer energy to the ytterbium and, eventually, to the erbium ions. The actual mechanism of energy transfer from one ion to another in the triply doped glass is quite complicated and may involve multiple channels. Since only the net path from chromium to erbium is of concern, the transfer can be simplified by using a single, measureable, characteristic transfer time (τ_{trans}) from the chromium bands to the $^4F_{13/2}$ upper laser level in erbium. The resulting rate equations derived for the system are as follows:

(50) $$\frac{dn_3}{dt} = W_{pump} n_0 - n_3/\tau_{30} - n_3/\tau_{tran} \qquad n_3(t=0) = 0$$

(51) $$\frac{dn_2}{dt} = \phi\, c\sigma_{21} n_1 \left(g_2/g_1 \right) + n_3/\tau_{tran} - \phi\, c\sigma_{21} n_2 - n_2/\tau_{21} \qquad n_2(t=0) = 0$$

(52) $$\frac{dn_1}{dt} = -\frac{dn_2}{dt} \qquad n_1(t=0) = n_{totEr}$$

(53) $$\frac{dn_0}{dt} = -\frac{dn_3}{dt} \qquad n_0(t=0) = n_{totCr}$$

(54) $$\frac{dn}{dt} = \frac{dn_2}{dt} - \frac{dn_1}{dt}(\gamma - 1) \qquad n(t=0) = n_{totEr}(\gamma - 1)$$

(55) $$\frac{d\phi}{dt} = \phi\, c\sigma_{21}\left(\frac{l}{l'}\right) n - \phi\frac{\varepsilon}{\tau_{cavity}} + \frac{n_2}{\tau_{21}}\Omega\left(\frac{l}{l'}\right) \qquad \phi(t=0) = 1/V$$

In these equations, n_3 and n_0 are the excited and ground state populations of the chromium ions, n_2 and n_1 are the excited and ground state populations of the erbium ions, ε is the single pass loss, τ_{cavity} is the lifetime of the laser resonator, l is the length of the rod, l' is the length of the resonator, and Ω is the solid angle over which a spontaneously emitted photon will be captured and oscillate in the resonator.

Transfer Lifetime

To properly model the laser system, the transfer time (τ_{trans}) needed to be experimentally measured and its variation with material temperature quantified. This was accomplished by pumping the chromium bands in a test sample of QE-7S glass with a Q-switched pulse from a MOPO system in the laboratory and watching the rise and decay of the resulting erbium emission. Figure 62 displays the shape of the curves resulting from the simplified model of the expected change in upper state population density (directly related to florescence) of erbium and chromium as the energy transfer from one ion to the other takes place.

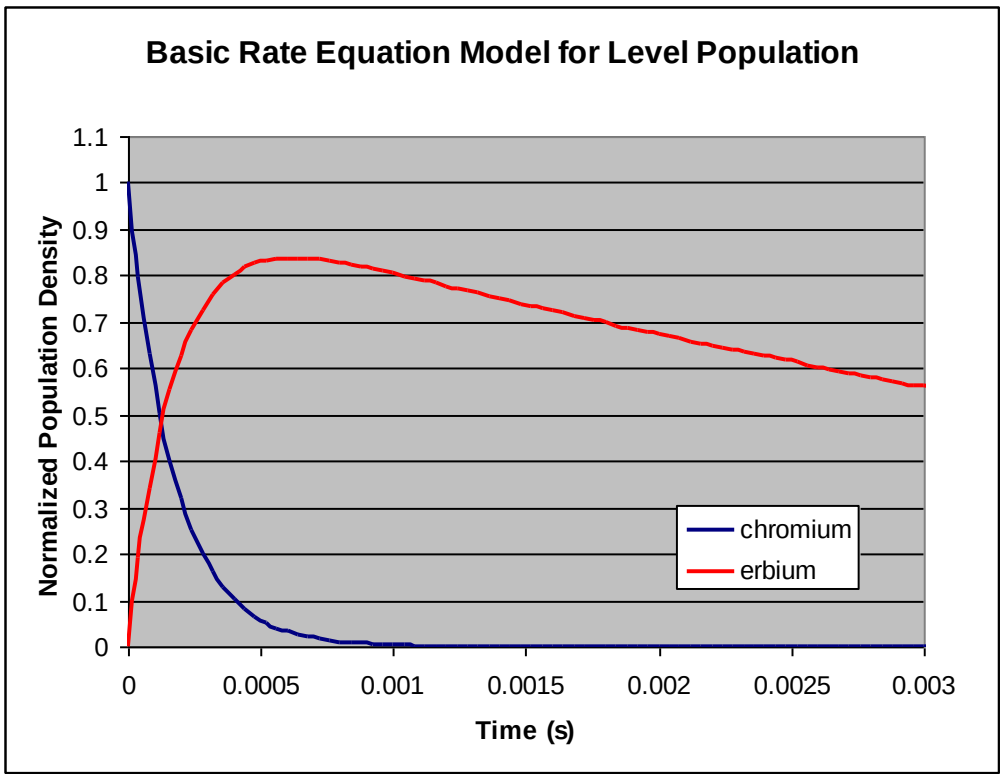

Figure 62 - Form of expected rise and decay in erbium and chromium level population due to energy transfer.

Figure 63 shows the experimentally measured florescence coming from the erbium ions when the chromium bands were pumped with a few nsec duration pulse. Data was taken at 35, 100, 200, 220, 250, and 295 K. The black curve is a fit using the curve shape determined from the simplified transfer model, which fit the data to a high degree of accuracy. A slight shift in the transfer time results as the temperature of the sample is increased.

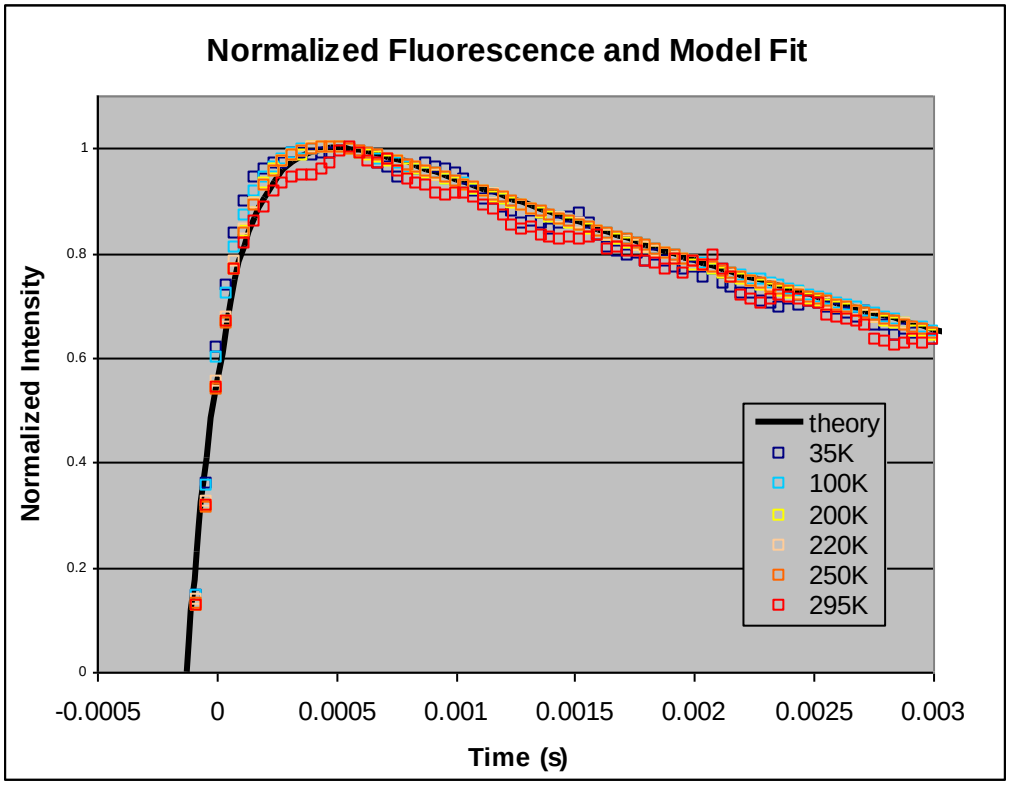

Figure 63 - Experimental data from transfer time measurement.

The transfer lifetime as function of temperature is plotted in Figure 64. A linear fit was conducted on the data and is plotted on the chart. The resulting value of the rate of change in

transfer lifetime with respect to temperature is 71 ns/K. This is only 7% of the value it would need if its variation were to solely account for the temperature variation seen in laser output, making it only a small contributor to the temperature dependent variation in the long pulse laser output energy.

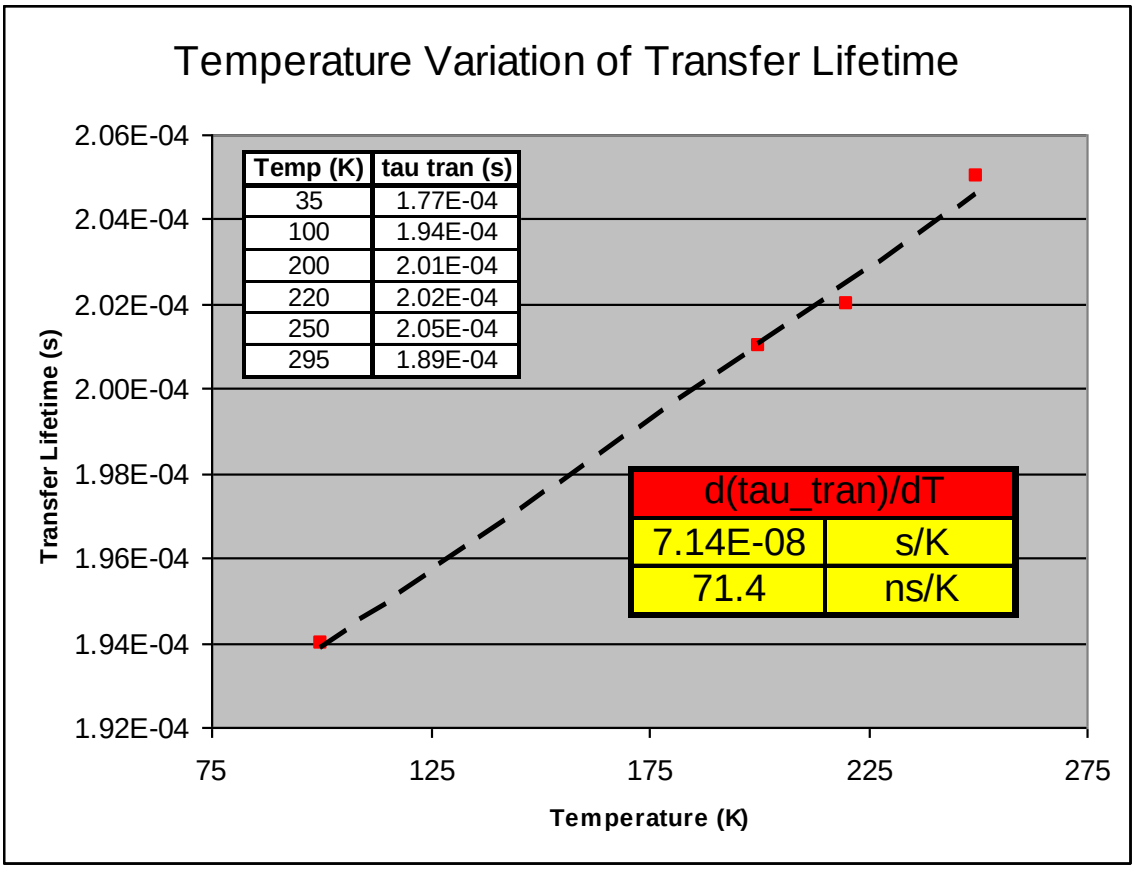

Figure 64 - Temperature dependence of the transfer lifetime from chromium to erbium in QE-7S glass. Data is shown from 100 to 250 K as well as a linear fit and resulting slope of 71.4 ns/K.

This measured transfer lifetime was then used as an input to the rate equation integration model. This model was then used to fit to experimental data and test potential sources of

temperature dependence in the system. APPENDIX C contains the MATLAB code used in the rate equation model. Figure 65 shows a temporal plot of experimental data and data generated using the new rate equation model. The output generated by integrating the rate equations has been convolved with the impulse response of the photodiode used in the experimental measurement to create a similar curve shape, suppressing the appearance of relaxation oscillations that appear in the model-generated data.

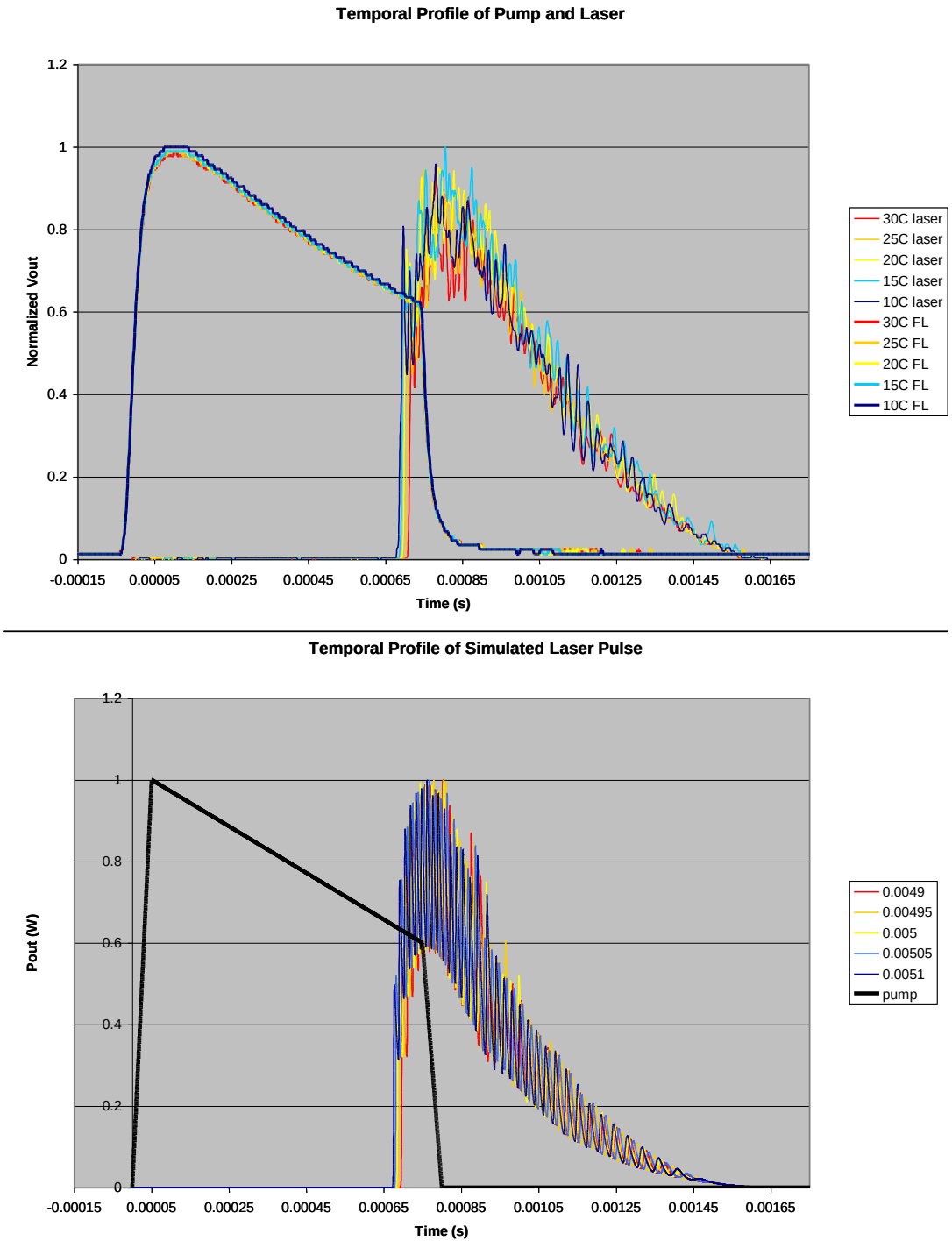

Figure 65 - Comparison of measured data for 99 % OC (top) and simulated data using measured temperature change in transfer time and assumed change in pump efficiency (bottom).

The Importance of the Absorption Cross Section

Another area where the initial model of the Cr,Yb,Er:glass system was inaccurate was in the assumption that the stimulated emission cross section of erbium (σ_{21}) is equal to the absorption cross section of erbium (σ_{12}). In the initial calculations, assuming $\sigma_{21} = \sigma_{12} = \sigma$, the small signal gain of the laser could be written as:

$$g = 2\sigma\ nl = 2\sigma(n_2 - \frac{g_2}{g_1} n_1)l \tag{56}$$

However, the values of σ_{21} and σ_{12} are actually connected though the reciprocity relation:

$$\sigma_{12} = \sigma_{21} \exp(-\frac{\left(\frac{hc}{\lambda_0}\right) - \left(\frac{hc}{\lambda}\right)}{kT}) \tag{57}$$

In this relation λ_0 is the zero phonon line of the emission (1535 nm in the present case) and λ is the wavelength of interest. Due to the inclusion of a Boltzmann factor in this relation, there is a temperature dependent relationship between the two cross sections. The small signal gain must actually be written as:

$$g = 2(\sigma_{21}(T)n_2 - \frac{g_2}{g_1}\sigma_{12}(T)n_1)l \tag{58}$$

This implies that because σ_{21} and σ_{12} have different curve shapes in wavelength space, the shape of the small signal gain in wavelength space will depend on the relative population densities of the upper and lower states n_1 and n_2. Thus, when the material is highly inverted (i.e. $n_2 >> n_1$), the gain curve will look much like the stimulated emission cross section, while at lower inversion levels ($n_2 \approx n_1$) it might look quite different. Figure 66 shows sample absorption and emission cross section curves for high and low temperatures.

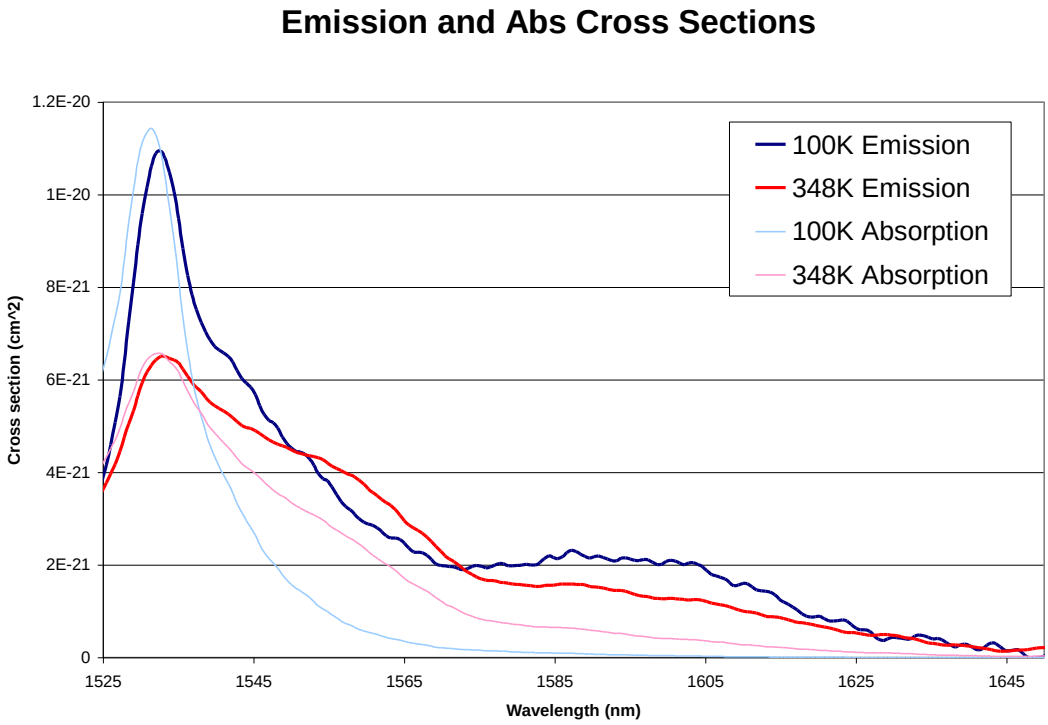

Figure 66 - Comparison of emission and absorption cross sections at high (348K) and low (100K) temperatures

The amount of inversion present in the laser system can easily be controlled through the choice of the reflectivity of the output coupler. Since the threshold is reached when gain (eq. 58) is equal to the system loss (eq. 35), higher system loss will create the need for a higher level of

gain in order to reach the lasing threshold. Thus, decreasing the reflectivity of the output coupler will drive the system to a greater level of inversion before lasing can begin.

Using measured values of the stimulated emission cross section of erbium at multiple temperatures, the corresponding absorption cross section was calculated. This then allowed the creation of a calculated gain vs. wavelength profile of the laser at any given temperature. In addition, the variation of the gain with temperature could be calculated as well. Figure 67 shows a plot of both the gain profile at room temperature and the net change in gain from 100 to 348 K for many different output couplers. A line is drawn for each gain curve to show the wavelength corresponding to maximum gain (and thus the wavelength at which unconstrained laser action will occur when broadband reflectors are used as end mirrors).

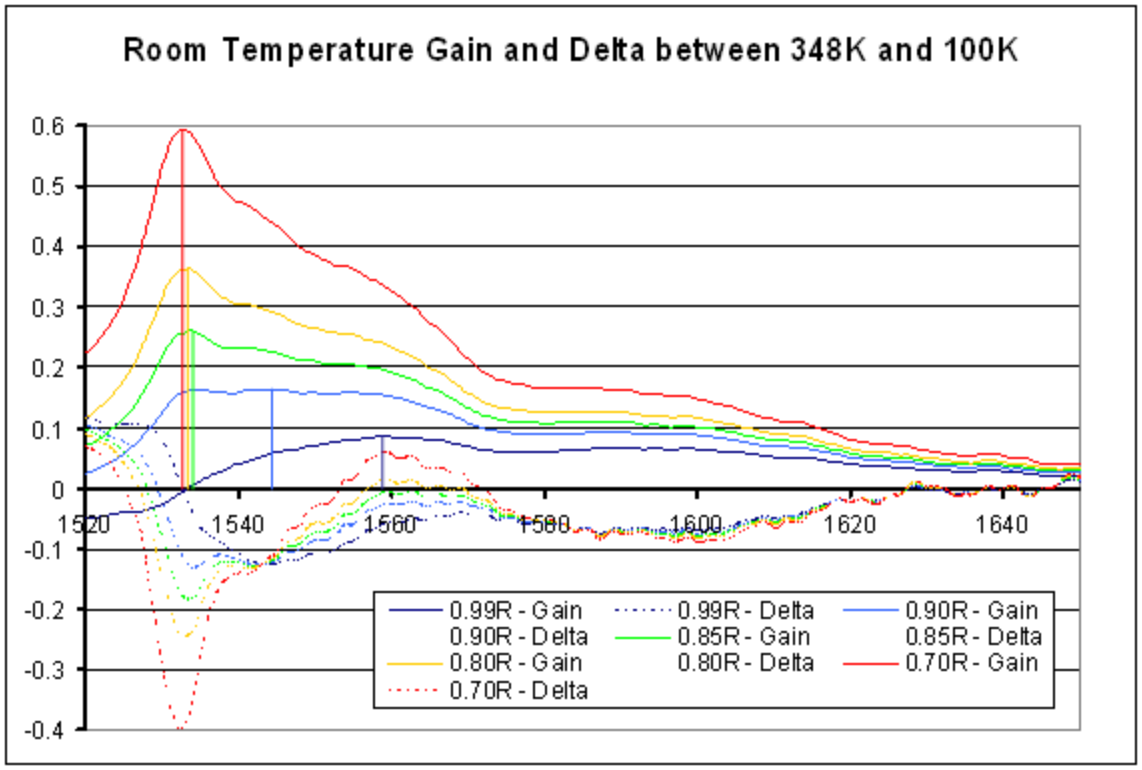

Figure 67 – Small signal gain (solid curves), and Delta (dotted curves) for the erbium laser transition wavelengths. Delta is defined as the total change in small signal gain over the temperature range from 348 to 100 K. Gain and Delta are plotted for a series of output coupler reflectivities ranging from 70 to 99%.

Of particular interest in Figure 67 is the fact that there is no point at which the change in gain with variation in temperature reaches zero for output coupler reflectivities above 85%. Thus, in order to truly create a system with temperature independent gain, a lower reflectivity mirror must be used. In addition, the wavelength of temperature independent gain changes with reflectivity.

For the initial experiment conducted with output coupler reflectivities of 90% and above, there is no wavelength at which gain is independent of temperature. In fact, at these high reflectivities the wavelength of maximum gain is actually quite near the VBG constrained

wavelength of 1552.75 nm. This would explain why switching from a dielectric mirror (which would result in lasing at the wavelength of maximum gain) to the VBG resulted in very little change in the observed output behavior in the initial experiments. According to the calculations plotted in Figure 67, in order for wavelengths exhibiting temperature independent gain to appear an 85% (or less) reflectivity mirror must be used and a VBG chosen with a proper center wavelength for that specific output coupler.

An experimental test of this expected shifting of the gain curves was conducted by measuring the laser emission wavelength when using dielectric mirrors of low (70% R) and high (90% R) reflectivity. Figure 68 shows a plot of the emission spectrum of the QE-7S laser while configured with a 90 and 70% R output coupler. These spectra were taken using an Ocean Optics NIR spectrometer with 7 nm resolution.

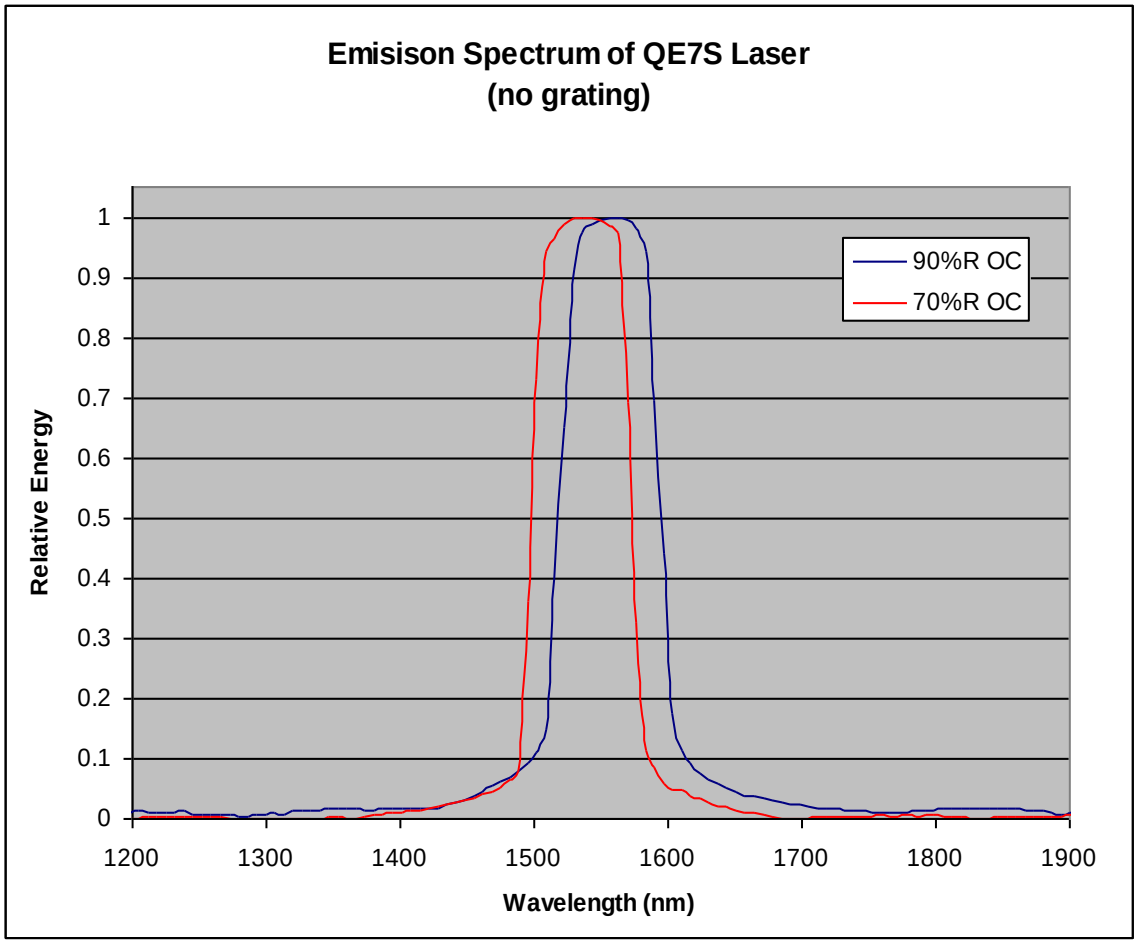

Figure 68 - Output spectra of QE-7S laser when using 90 and 70% R output couplers. Emission shifts to shorter wavelengths as predicted when reflectivity is decreased.

Table 7 contains information about the measured and calculated emission wavelengths for the two output coupler reflectivities. Two measured values are reported: the peak wavelength of the spectra and the center wavelength of the measured distribution calculated as the center of half max spread. The average of these two measurements is compared to the theoretically expected lasing wavelength (the wavelength of maximum gain from the corresponding curve in Figure 67).

	90%	70%
FWHM (nm)	103.2	98.5
Center Wavelength (nm)	1557.1	1536.4
Peak Wavelength (nm)	1556.2	1529.2
Theoretical Peak (nm)	1554.8	1533.2
Error	0.12%	-0.03%

Table 7 - Summary of calculated and measured values of emission wavelength of QE-7S laser with 90% R and 70% R output couplers

The experimental values matched the predicted values to within well less than a percent, indicating that the changes in the gain curves are real and significant and caused by differences in inversion level arising from different curve shapes for stimulated emission and absorption for the laser transition.

Re-constraining the Er:glass system to operate with athermal gain

A VBG with Bragg wavelength of 1558 nm (0.25 nm FWHM), and 99 % diffraction efficiency was purchased from Optigrate to constrain the laser oscillation to the predicted point of zero gain change seen in Figure 67 for 70 and 80% reflectivity output couplers. The slope efficiency curves were again measured using the long pulsed laser testbed with the VBG used as a high reflectivity end reflector and two different 2 m radius of curvature dielectric output couplers with reflectivities of 70 and 80%. Since the VBG center wavelength was matched to the athermal gain point for laser operation with an inversion level that corresponded only to a system with output coupling reflectivity in this range, other output coupler reflectivities were not explored. When using the 70 % output coupler and VBG as end mirror, the laser could not be pumped hard

enough to reach threshold with the flashlamp pump system that was in use. With the 80 % reflectivity output coupler in the system, the laser did reach threshold. Slope efficiency data was collected and is plotted in Figure 69 for rod temperatures of 10, 15, 20, 25 and 30 °C.

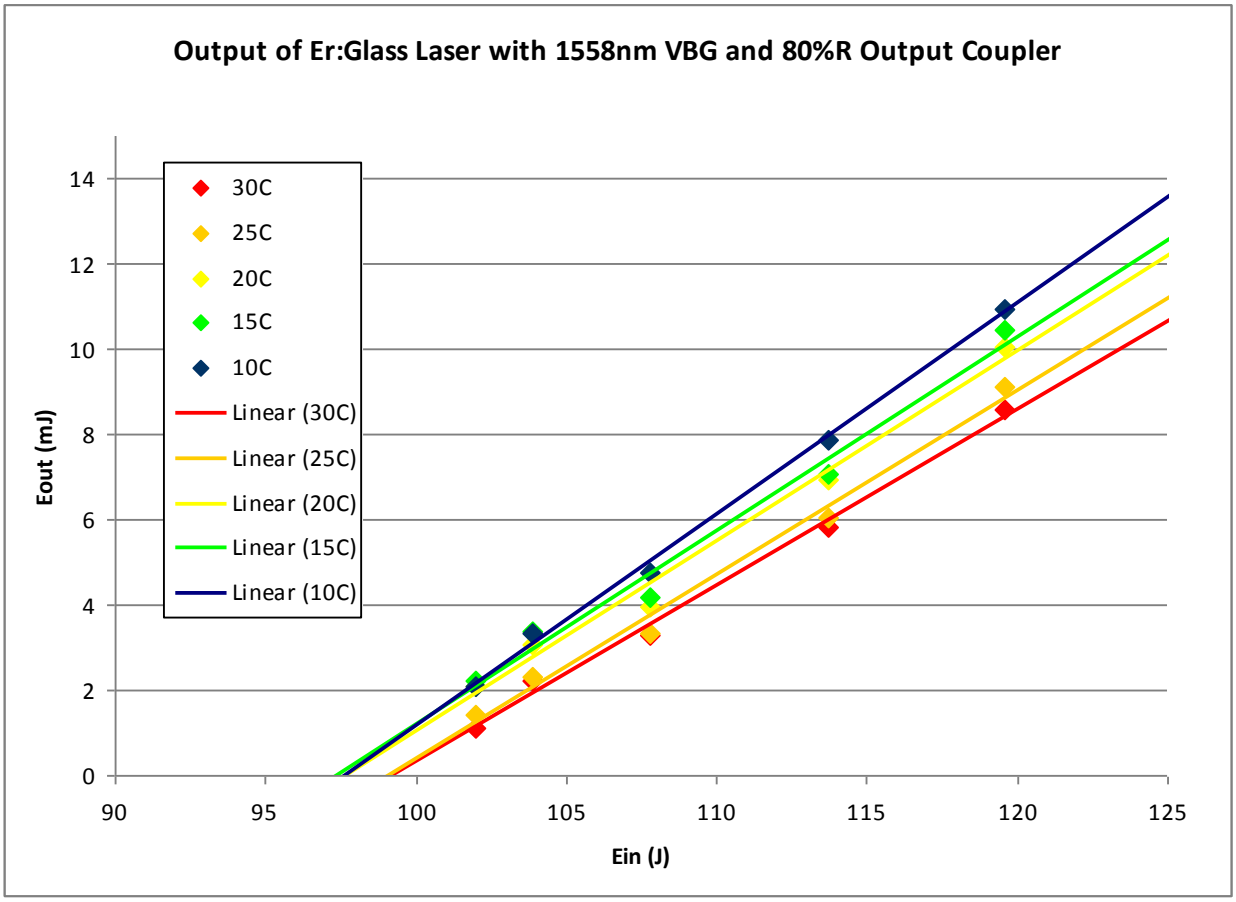

Figure 69 - Measured output vs. input energy taken from the longpulsed Er:glass laser testbed utilizing a 99 % R VBG centered at 1558 nm and an 80% R dielectric mirror with 2 m radius of curvature.

The system still clearly exhibits strong temperature dependence in its output power, with slope efficiency varying by 17% and threshold energy varying by 1.5% over a 20 °C change in rod temperature. Simulations with the long pulsed rate equation software model indicate no expected change in output energy over this temperature range. This indicates that the source of

the output variation with change in rod temperature is not related to inherent changes rooted in the stimulated emission and absorption cross-sections, but most likely from temperature induced changes in the pump efficiency of the laser.

Passive Q-switched operation

Since the laser system is pumped by a broadband emitting flashlamp, the temperature induced changes in the absorption cross sections of the chromium and ytterbium pump bands should not affect the pump efficiency of the laser. Thermal changes in cross section involve a redistribution of the pump absorption across the pump band, but the total absorption (area under the cross-section curve) remains the same for a given pump band as temperature changes. Since the flashlamp pumps the entire pump band relatively evenly across wavelength, the total amount of absorbed pump power should not change with variation in the peak cross-section value as the temperature of the gain medium changes. For this reason, the changing pump efficiency most likely results from another process such as a change in the energy transfer between the pumped ions and the upper laser level in erbium.

One method of reducing the effect of pump energy on the output of a laser system is the use of passive q-switching. Passive Q-switching uses an intra-cavity saturable absorber to alter the loss in the laser cavity through passive means. The saturable absorber starts with an initial amount of absorption that provides loss in the laser resonator and prevents laser oscillation from occurring as inversion is built in the gain medium. Eventually the saturable absorber reaches saturation and it becomes optically transparent (or at least more transparent than in its

unsaturated state). This suddenly increases the cavity Q with the system already pumped to a level of gain well above the new low loss threshold level, resulting in the emission of a q-switched pulse. The first passive q-switched laser was developed in 1964, just two years after the invention of the q-switch itself [80], using a cryptocyanine dye [81]. One of the best saturable absorbers for 1.5 μm emission is Co^{2+}:Mg_2AlO_4, commonly referred to as Co:Spinel [82-84].

The onset of photo-bleaching of a saturable absorber happens when the laser medium reaches an inversion level such that the gain in the laser begins to overcome the loss of the passive q-switch, resulting in the rapid 'opening' of the switch and production of a q-switched pulse. The properties of the output pulse are entirely set by the inversion at the onset of saturation and the gain of the laser material for given level of inversion (the stimulated emission and absorption cross-sections of the gain material). The pump efficiency of the laser has no effect on the power and duration of the output q-switched pulse. Once the laser is pumped to the proper inversion level for saturation to begin, the q-switch fires and the laser pulse proceeds without regard to how much total pump energy was needed to start the process. For this reason, a passive q-switch is the perfect instrument for eliminating the effect of small changes in pump efficiency on a laser system. The only effect that change in pump power or efficiency can have is the production of multiple q-switch pulses if there is enough pump energy to drive the laser back to saturation inversion [35] after the initial q-switched pulse. Another potential effect is the sudden ceasing of q-switched output if loss of pump power or efficiency drops the pumped inversion level below that needed for initial saturation of the saturable absorber.

The Er:glass laser testbed used in previous experiments was modified by placing a saturable absorber (Co:spinel) in the laser resonator to induce passive q-switched operation. Initially, the attempt at passive q-switched operation utilized a 5 % (unsaturated) loss Co:spinel absorber in the laser cavity with a 1558 nm VBG end reflector and 90 % reflectivity output coupler. The resulting system began to exhibit passive q-switched output when pumped with 61.4J of electrical energy. However, after about a half dozen shots, the pulse energy degraded from 12 mJ to no longer firing. Damage was later observed on the passive q-switch, and new q-switches were ordered. A second attempt at passive q-switching was later attempted with a 70 % output coupler (to reduce intra cavity fluence) and an 8 % (unsaturated) loss Co:spinel q-switch, utilizing a dielectric 99 % R end mirror. This test with the lower output coupler reflectivity was successful in producing a consistent q-switched pulse without damage occurring to any of the system's optical coatings. The laser was pumped with 127.5J (electrical energy) at 30 °C and the temperature of the rod was lowered to 25, 20, 15, and 10°C. As the rod temperature was lowered, the system began to experience multiple pulsing due to the increase in pump efficiency with temperature. Whenever multiple pulsing occurred, the input energy was lowered until a single output pulse was again observed. Figure 70 contains a plot of the output energy of the single pulse output across the observed temperature range and compares it to a plot of output energy variation using the same experimental setup without the passive q-switch.

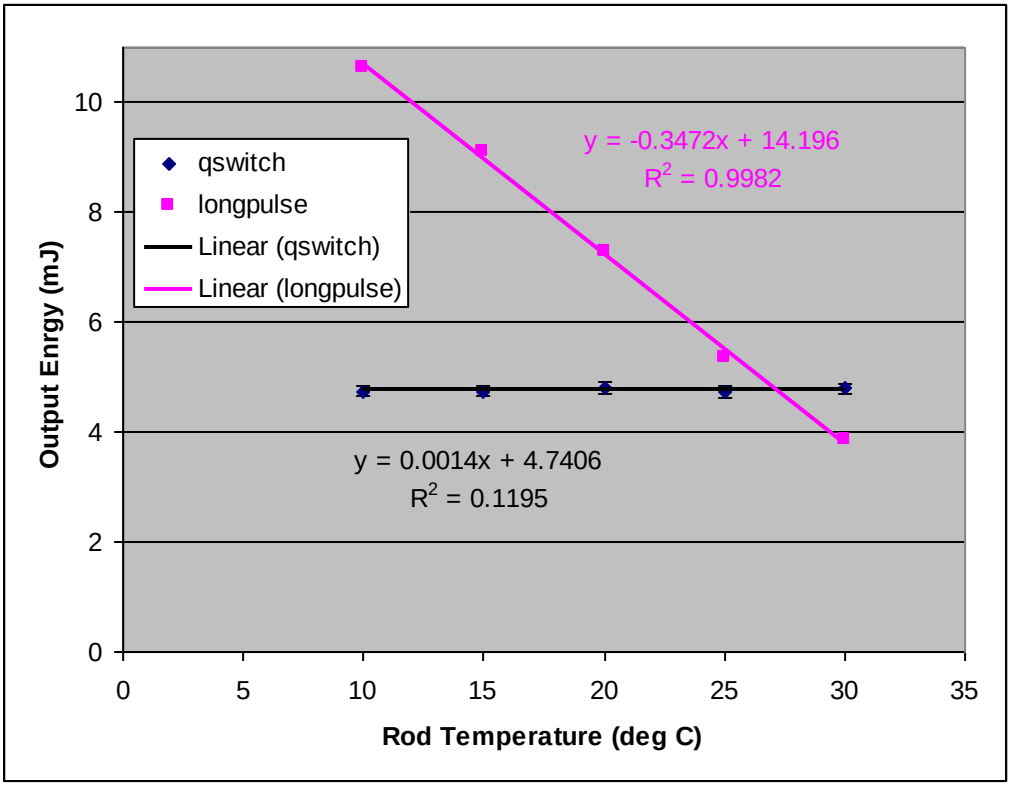

Figure 70 - Plot of output energy vs. temperature for single pulse operation of the passively q-switched Er:glass laser and for the same laser without the passive q-switch.

The use of the passive q-switch reduced the output variation seen from over 100% to less than the experimental accuracy of the energy measurement (roughly 0.1 mJ). However, this measurement did not mean that the system had been truly athermalized. The input energy of the laser had to be adjusted to prevent multiple pulses from occurring, requiring active control of the pump energy.

Controlling the temperature dependent change in pump efficiency

The lack of change in the output energy of the single q-switched pulse indicated that the change in stimulated emission cross section (and resulting change in absorption cross section) were insignificant factors in the temperature variation seen in the Er:glass system. The fact that the output remained athermal for single pulse operation, without the use of a VBG to control the system gain, indicates that this control mechanism is not needed for passive q-switched Er:glass systems. While there is no need to control for changes in laser gain, some mechanism must be used to control the temperature dependent change in pump efficiency that was driving the multiple pulse behavior as the rod temperature was reduced.

A literature search for Co:spinel passive q-switches turned up a conference presentation at ASSL in 1998 [87] where the thermal properties of Kigre QE-7S chromium, ytterbium, and erbium doped glass was investigated. A considerable variation was reported in the effective pump efficiency of the system with changes in rod temperature and attributed to temperature dependent quenching of the transfer of energy from the chromium bands to the ytterbium bands and thus to the erbium ions. A 50 % change in transfer efficiency was observed over a 125 °C change in the glass temperature. This would correspond to an 8 % change in pump efficiency over the 20 °C range of temperatures observed in the measurements. Additionally, it was shown that the use of other sensitizing ions (neodymium instead of chromium) to improve flashlamp pump efficiency removed this large thermal shift in pump efficiency.

The 8 % change in pump efficiency fully accounts for the changes in output energy seen in the measurements previously presented. Simulation using the change in pump efficiency to

generate the measured changes in output behavior required a 7 % change in pump efficiency to match experimental data. This value is consistent with that found in [87].

Attempts to further athermalize the system through the use of more optically dense passive q-switches were attempted. A more optically dense q-switch would require a greater buildup of inversion in the rod after the initial q-switch pulse before secondary pulses would be created. These attempts were unsuccessful due to the limited amount of pump power the test bed could deliver (a pump energy of greater than 200J was utilized without reaching laser threshold). When the 9 % loss q-switched used for previous testing was switched with a 15 % loss q-switch, the system could not be brought to threshold.

Conclusions

Many important uses for laser systems demand operation of the laser over a wide range of temperatures. A lightweight, passive solution for athermalizing laser output would provide great benefit to laser systems where weight, volume, and power requirements are critical. The recent advent of the volume Bragg grating has provided a unique tool that might make these solutions a reality. Paths forward exist for using VBGs as wavelength selective devices to select proper operating wavelengths where laser system output becomes athermal.

Athermalization of solid state laser systems has proven to be a quite complicated subject. This research has shown that while the emission cross-section of many types of three-level laser systems might exhibit a crossover point where the emission cross-section does not change with changes in the temperature of the gain material, constraint of the laser emission to this

wavelength is not a sufficient condition to athermalize the output of the laser system. This is primarily due to the difference between stimulated emission cross section and absorption cross section in three-level laser systems. These values are related through a reciprocity formula and interact is such a way that both effect the gain spectrum of the laser. The overall shape of the gain spectrum of the laser changes due to the changes in the inversion level of the laser, which can be determined by the reflectivity of the laser's output coupling mirror. Changing output reflectivity of a three-level laser can shift the unconstrained wavelength of laser oscillation as the wavelength of peak gain changes with changing inversion level. Any attempt at constraining the temperature dependence of laser gain must take into account the reflectivity used in the laser resonator of interest.

Additionally, care must be taken when attempting to model the behavior of long florescence lifetime materials. Laser behavior when the input pump pulse duration is less than the florescence lifetime of the material never reaches a steady state operating condition. It must be modeled temporally and does not adhere to the typical solid state laser output equations (37) and (38).

The potential use of the temperature dependent shift in VBG reflectivity remains of interest for use in both three- and four- level laser systems. While its effectiveness might be limited by an inability to completely match the temperature dependent wavelength shift of the VBG to temperature dependent changes in the gain of a laser, it is well worth pursuing. Exploring possibilities for passive athermalization of laser systems will be of great interest to the laser engineering community not only in the development of new design techniques, but in

furthering the understanding of the true drivers for temperature related output variation in solid state laser systems.

APPENDIX A – ASAP RAY TRACE MODELING CODE

```
SYSTEM NEW
RESET

!! Define system units and wavelengths

UNITS MILLIMETERS 'Watts'
WAVELENGTH 808 NM

CORED=.1
CLADD=.25
FLENGTH=35
FLATPOS=-.110
BAR_P=-35

!! Define coatings

COATING PROPERTIES
 0 1 'TRANSMIT'
 1 0 'REFLECT'
 0 0 'ABSORB'

!! Define Media

MEDIA
 1.5689 ABSORB 2.8 'CORE'
 1.5734 'CLAD'

FRESNEL AVG
SPLIT 1
ARROWS OFF

ANGLE=45  !!  Gaussian model for ground rod surface
A=SIN[ANGLE]^2  !! Scale factor
$FCN GDIS1 GAUS(SQRT(_1/A))
MODEL 1
 USERBSDF GDIS1

 !!GEOMETRY DEFINITIONS BEGIN HERE
SURFACE
 PLANE Y (FLATPOS) RECT 40 40

EDGES
 ELLIPSE X 0 (CORED/2) (CORED/2) 16
SMOOTH
 ELLIPSE X 0 (CLADD/2) (CLADD/2) 16
SMOOTH
OBJECT
 .2 .1 'CLAD.FRONT'
 BOUNDS .3
INTERFACE COATING BARE AIR CLAD

EDGES
 ELLIPSE X (FLENGTH) (CORED/2) (CORED/2) 16
SMOOTH
 ELLIPSE X (FLENGTH) (CLADD/2) (CLADD/2) 16
SMOOTH
OBJECT
 .2 .1 'CLAD.BACK'
 BOUNDS .5
INTERFACE COATING BARE AIR CLAD

SURFACE
 PLANE X 0 ELLIPSE (CORED/2) (CORED/2)
```

```
OBJECT 'CORE.FRONT'
INTERFACE COATING BARE AIR CORE

SURFACE
  PLANE X (FLENGTH) ELLIPSE (CORED/2) (CORED/2)
OBJECT 'CORE.BACK'
INTERFACE COATING BARE AIR CORE

SURFACE
  TUBE X 0 (CORED/2) (CORED/2) (FLENGTH) (CORED/2) (CORED/2)
OBJECT 'CORE.SIDE'
INTERFACE COATING BARE CORE CLAD

EDGE
  ELLIPSE X 0 (CLADD/2) (CLADD/2) 64
SURFACE
  PLANE X 0 2 2
  PLANE X (FLENGTH) 2 2
  PLANE Y (FLATPOS) RECT .5 40
OBJECT 'CLAD.FLAT'
BOUNDS -.4 .3 -.2
INTERFACE COATING BARE AIR CLAD
FACETS 64 11

SURFACE
  TUBE X 0 (CLADD/2) (CLADD/2) (FLENGTH) (CLADD/2) (CLADD/2)
OBJECT 'CLAD.SIDE'
BOUNDS .2
INTERFACE COATING REFLECT AIR CLAD
!!ROUGHNESS  MODEL 1
SCATTER RANDOM 1 1

SURFACE
  TUBE X 0 3 3 (FLENGTH) 3 3
OBJECT 'LENS'
INTERFACE COATING TRANSMIT AIR BK7
SHIFT Y -6.15

SURFACE
  PLANE Y (BAR_P-.1) RECT .001 (FLENGTH/2)
OBJECT 'TESTPLANE'
INTERFACE COATING ABSORB AIR AIR
SHIFT X (FLENGTH/2)

!!SOURCE DEFINITIONS BEGIN HERE

  BAR_LENGTH=.09;  BAR_WIDTH=0.001

  NRAYS=10000;
  ESPACING=.133
  DIVERGENCE_FAST=45;!!HALF ANGLE
  DIVERGENCE_SLOW=45;
  FWHM_X=10 !! SLOW AXIS
  FWHM_Z=1  !! FAST AXIS
$FCN GDIS GAUS(SQRT((LOG(2)*_1^2/(SIN[FWHM_Z/2])^2)+(LOG(2)*_2^2/(SIN[FWHM_X/2])^2)))
!!$FCN GDIS  EXP(-1*((_1*((LOG(2))^(1/8))/(SIN[FWHM_Z/2]))^4+(_2*SQRT(LOG(2))/(SIN[FWHM_X/2]))^2))
!!$FCN GDIS  EXP(-1*((_2*SQRT(LOG(2))/(SIN[FWHM_X/2]))^2)+(_1*((LOG(2))^(1/8))/(SIN[FWHM_Z/2]))^4)

!!$FCN GDIS GAUS[SQRT((TAN[22]/TAN[5])^2*_2^2+(TAN[22]/TAN[20])^2*_1^2)] !! gaussian hand fit
 USERAPOD DIR GDIS

  BAR1POS=2
EMITTING RECT Y (BAR_P) (BAR_WIDTH/2) (BAR_LENGTH/2) (NRAYS) (DIVERGENCE_FAST) (DIVERGENCE_SLOW)      ISO
SHIFT X (BAR1POS)+0*(ESPACING)
EMITTING RECT Y (BAR_P) (BAR_WIDTH/2) (BAR_LENGTH/2) (NRAYS) (DIVERGENCE_FAST) (DIVERGENCE_SLOW)      ISO
SHIFT X (BAR1POS)+1*(ESPACING)
```

EMITTING RECT Y (BAR_P) (BAR_WIDTH/2) (BAR_LENGTH/2) (NRAYS) (DIVERGENCE_FAST) (DIVERGENCE_SLOW) ISO SHIFT X (BAR1POS)+2*(ESPACING)
EMITTING RECT Y (BAR_P) (BAR_WIDTH/2) (BAR_LENGTH/2) (NRAYS) (DIVERGENCE_FAST) (DIVERGENCE_SLOW) ISO SHIFT X (BAR1POS)+3*(ESPACING)
EMITTING RECT Y (BAR_P) (BAR_WIDTH/2) (BAR_LENGTH/2) (NRAYS) (DIVERGENCE_FAST) (DIVERGENCE_SLOW) ISO SHIFT X (BAR1POS)+4*(ESPACING)
EMITTING RECT Y (BAR_P) (BAR_WIDTH/2) (BAR_LENGTH/2) (NRAYS) (DIVERGENCE_FAST) (DIVERGENCE_SLOW) ISO SHIFT X (BAR1POS)+5*(ESPACING)
EMITTING RECT Y (BAR_P) (BAR_WIDTH/2) (BAR_LENGTH/2) (NRAYS) (DIVERGENCE_FAST) (DIVERGENCE_SLOW) ISO SHIFT X (BAR1POS)+6*(ESPACING)
EMITTING RECT Y (BAR_P) (BAR_WIDTH/2) (BAR_LENGTH/2) (NRAYS) (DIVERGENCE_FAST) (DIVERGENCE_SLOW) ISO SHIFT X (BAR1POS)+7*(ESPACING)
EMITTING RECT Y (BAR_P) (BAR_WIDTH/2) (BAR_LENGTH/2) (NRAYS) (DIVERGENCE_FAST) (DIVERGENCE_SLOW) ISO SHIFT X (BAR1POS)+8*(ESPACING)
EMITTING RECT Y (BAR_P) (BAR_WIDTH/2) (BAR_LENGTH/2) (NRAYS) (DIVERGENCE_FAST) (DIVERGENCE_SLOW) ISO SHIFT X (BAR1POS)+9*(ESPACING)
EMITTING RECT Y (BAR_P) (BAR_WIDTH/2) (BAR_LENGTH/2) (NRAYS) (DIVERGENCE_FAST) (DIVERGENCE_SLOW) ISO SHIFT X (BAR1POS)+10*(ESPACING)
EMITTING RECT Y (BAR_P) (BAR_WIDTH/2) (BAR_LENGTH/2) (NRAYS) (DIVERGENCE_FAST) (DIVERGENCE_SLOW) ISO SHIFT X (BAR1POS)+11*(ESPACING)
EMITTING RECT Y (BAR_P) (BAR_WIDTH/2) (BAR_LENGTH/2) (NRAYS) (DIVERGENCE_FAST) (DIVERGENCE_SLOW) ISO SHIFT X (BAR1POS)+12*(ESPACING)
EMITTING RECT Y (BAR_P) (BAR_WIDTH/2) (BAR_LENGTH/2) (NRAYS) (DIVERGENCE_FAST) (DIVERGENCE_SLOW) ISO SHIFT X (BAR1POS)+13*(ESPACING)
EMITTING RECT Y (BAR_P) (BAR_WIDTH/2) (BAR_LENGTH/2) (NRAYS) (DIVERGENCE_FAST) (DIVERGENCE_SLOW) ISO SHIFT X (BAR1POS)+14*(ESPACING)
EMITTING RECT Y (BAR_P) (BAR_WIDTH/2) (BAR_LENGTH/2) (NRAYS) (DIVERGENCE_FAST) (DIVERGENCE_SLOW) ISO SHIFT X (BAR1POS)+15*(ESPACING)
EMITTING RECT Y (BAR_P) (BAR_WIDTH/2) (BAR_LENGTH/2) (NRAYS) (DIVERGENCE_FAST) (DIVERGENCE_SLOW) ISO SHIFT X (BAR1POS)+16*(ESPACING)
EMITTING RECT Y (BAR_P) (BAR_WIDTH/2) (BAR_LENGTH/2) (NRAYS) (DIVERGENCE_FAST) (DIVERGENCE_SLOW) ISO SHIFT X (BAR1POS)+17*(ESPACING)
EMITTING RECT Y (BAR_P) (BAR_WIDTH/2) (BAR_LENGTH/2) (NRAYS) (DIVERGENCE_FAST) (DIVERGENCE_SLOW) ISO SHIFT X (BAR1POS)+18*(ESPACING)
EMITTING RECT Y (BAR_P) (BAR_WIDTH/2) (BAR_LENGTH/2) (NRAYS) (DIVERGENCE_FAST) (DIVERGENCE_SLOW) ISO SHIFT X (BAR1POS)+19*(ESPACING)
EMITTING RECT Y (BAR_P) (BAR_WIDTH/2) (BAR_LENGTH/2) (NRAYS) (DIVERGENCE_FAST) (DIVERGENCE_SLOW) ISO SHIFT X (BAR1POS)+20*(ESPACING)
EMITTING RECT Y (BAR_P) (BAR_WIDTH/2) (BAR_LENGTH/2) (NRAYS) (DIVERGENCE_FAST) (DIVERGENCE_SLOW) ISO SHIFT X (BAR1POS)+21*(ESPACING)
EMITTING RECT Y (BAR_P) (BAR_WIDTH/2) (BAR_LENGTH/2) (NRAYS) (DIVERGENCE_FAST) (DIVERGENCE_SLOW) ISO SHIFT X (BAR1POS)+22*(ESPACING)
EMITTING RECT Y (BAR_P) (BAR_WIDTH/2) (BAR_LENGTH/2) (NRAYS) (DIVERGENCE_FAST) (DIVERGENCE_SLOW) ISO SHIFT X (BAR1POS)+23*(ESPACING)
EMITTING RECT Y (BAR_P) (BAR_WIDTH/2) (BAR_LENGTH/2) (NRAYS) (DIVERGENCE_FAST) (DIVERGENCE_SLOW) ISO SHIFT X (BAR1POS)+24*(ESPACING)
EMITTING RECT Y (BAR_P) (BAR_WIDTH/2) (BAR_LENGTH/2) (NRAYS) (DIVERGENCE_FAST) (DIVERGENCE_SLOW) ISO SHIFT X (BAR1POS)+25*(ESPACING)
EMITTING RECT Y (BAR_P) (BAR_WIDTH/2) (BAR_LENGTH/2) (NRAYS) (DIVERGENCE_FAST) (DIVERGENCE_SLOW) ISO SHIFT X (BAR1POS)+26*(ESPACING)
EMITTING RECT Y (BAR_P) (BAR_WIDTH/2) (BAR_LENGTH/2) (NRAYS) (DIVERGENCE_FAST) (DIVERGENCE_SLOW) ISO SHIFT X (BAR1POS)+27*(ESPACING)
EMITTING RECT Y (BAR_P) (BAR_WIDTH/2) (BAR_LENGTH/2) (NRAYS) (DIVERGENCE_FAST) (DIVERGENCE_SLOW) ISO SHIFT X (BAR1POS)+28*(ESPACING)
EMITTING RECT Y (BAR_P) (BAR_WIDTH/2) (BAR_LENGTH/2) (NRAYS) (DIVERGENCE_FAST) (DIVERGENCE_SLOW) ISO SHIFT X (BAR1POS)+29*(ESPACING)
EMITTING RECT Y (BAR_P) (BAR_WIDTH/2) (BAR_LENGTH/2) (NRAYS) (DIVERGENCE_FAST) (DIVERGENCE_SLOW) ISO SHIFT X (BAR1POS)+30*(ESPACING)
EMITTING RECT Y (BAR_P) (BAR_WIDTH/2) (BAR_LENGTH/2) (NRAYS) (DIVERGENCE_FAST) (DIVERGENCE_SLOW) ISO SHIFT X (BAR1POS)+31*(ESPACING)
EMITTING RECT Y (BAR_P) (BAR_WIDTH/2) (BAR_LENGTH/2) (NRAYS) (DIVERGENCE_FAST) (DIVERGENCE_SLOW) ISO SHIFT X (BAR1POS)+32*(ESPACING)
EMITTING RECT Y (BAR_P) (BAR_WIDTH/2) (BAR_LENGTH/2) (NRAYS) (DIVERGENCE_FAST) (DIVERGENCE_SLOW) ISO SHIFT X (BAR1POS)+33*(ESPACING)
EMITTING RECT Y (BAR_P) (BAR_WIDTH/2) (BAR_LENGTH/2) (NRAYS) (DIVERGENCE_FAST) (DIVERGENCE_SLOW) ISO SHIFT X (BAR1POS)+34*(ESPACING)

EMITTING RECT Y (BAR_P) (BAR_WIDTH/2) (BAR_LENGTH/2) (NRAYS) (DIVERGENCE_FAST) (DIVERGENCE_SLOW) ISO SHIFT X (BAR1POS)+35*(ESPACING)
EMITTING RECT Y (BAR_P) (BAR_WIDTH/2) (BAR_LENGTH/2) (NRAYS) (DIVERGENCE_FAST) (DIVERGENCE_SLOW) ISO SHIFT X (BAR1POS)+36*(ESPACING)
EMITTING RECT Y (BAR_P) (BAR_WIDTH/2) (BAR_LENGTH/2) (NRAYS) (DIVERGENCE_FAST) (DIVERGENCE_SLOW) ISO SHIFT X (BAR1POS)+37*(ESPACING)
EMITTING RECT Y (BAR_P) (BAR_WIDTH/2) (BAR_LENGTH/2) (NRAYS) (DIVERGENCE_FAST) (DIVERGENCE_SLOW) ISO SHIFT X (BAR1POS)+38*(ESPACING)
EMITTING RECT Y (BAR_P) (BAR_WIDTH/2) (BAR_LENGTH/2) (NRAYS) (DIVERGENCE_FAST) (DIVERGENCE_SLOW) ISO SHIFT X (BAR1POS)+39*(ESPACING)
EMITTING RECT Y (BAR_P) (BAR_WIDTH/2) (BAR_LENGTH/2) (NRAYS) (DIVERGENCE_FAST) (DIVERGENCE_SLOW) ISO SHIFT X (BAR1POS)+40*(ESPACING)
EMITTING RECT Y (BAR_P) (BAR_WIDTH/2) (BAR_LENGTH/2) (NRAYS) (DIVERGENCE_FAST) (DIVERGENCE_SLOW) ISO SHIFT X (BAR1POS)+41*(ESPACING)
EMITTING RECT Y (BAR_P) (BAR_WIDTH/2) (BAR_LENGTH/2) (NRAYS) (DIVERGENCE_FAST) (DIVERGENCE_SLOW) ISO SHIFT X (BAR1POS)+42*(ESPACING)
EMITTING RECT Y (BAR_P) (BAR_WIDTH/2) (BAR_LENGTH/2) (NRAYS) (DIVERGENCE_FAST) (DIVERGENCE_SLOW) ISO SHIFT X (BAR1POS)+43*(ESPACING)
EMITTING RECT Y (BAR_P) (BAR_WIDTH/2) (BAR_LENGTH/2) (NRAYS) (DIVERGENCE_FAST) (DIVERGENCE_SLOW) ISO SHIFT X (BAR1POS)+44*(ESPACING)
EMITTING RECT Y (BAR_P) (BAR_WIDTH/2) (BAR_LENGTH/2) (NRAYS) (DIVERGENCE_FAST) (DIVERGENCE_SLOW) ISO SHIFT X (BAR1POS)+45*(ESPACING)
EMITTING RECT Y (BAR_P) (BAR_WIDTH/2) (BAR_LENGTH/2) (NRAYS) (DIVERGENCE_FAST) (DIVERGENCE_SLOW) ISO SHIFT X (BAR1POS)+46*(ESPACING)
EMITTING RECT Y (BAR_P) (BAR_WIDTH/2) (BAR_LENGTH/2) (NRAYS) (DIVERGENCE_FAST) (DIVERGENCE_SLOW) ISO SHIFT X (BAR1POS)+47*(ESPACING)
EMITTING RECT Y (BAR_P) (BAR_WIDTH/2) (BAR_LENGTH/2) (NRAYS) (DIVERGENCE_FAST) (DIVERGENCE_SLOW) ISO SHIFT X (BAR1POS)+48*(ESPACING)
EMITTING RECT Y (BAR_P) (BAR_WIDTH/2) (BAR_LENGTH/2) (NRAYS) (DIVERGENCE_FAST) (DIVERGENCE_SLOW) ISO SHIFT X (BAR1POS)+49*(ESPACING)
EMITTING RECT Y (BAR_P) (BAR_WIDTH/2) (BAR_LENGTH/2) (NRAYS) (DIVERGENCE_FAST) (DIVERGENCE_SLOW) ISO SHIFT X (BAR1POS)+50*(ESPACING)
EMITTING RECT Y (BAR_P) (BAR_WIDTH/2) (BAR_LENGTH/2) (NRAYS) (DIVERGENCE_FAST) (DIVERGENCE_SLOW) ISO SHIFT X (BAR1POS)+51*(ESPACING)
EMITTING RECT Y (BAR_P) (BAR_WIDTH/2) (BAR_LENGTH/2) (NRAYS) (DIVERGENCE_FAST) (DIVERGENCE_SLOW) ISO SHIFT X (BAR1POS)+52*(ESPACING)
EMITTING RECT Y (BAR_P) (BAR_WIDTH/2) (BAR_LENGTH/2) (NRAYS) (DIVERGENCE_FAST) (DIVERGENCE_SLOW) ISO SHIFT X (BAR1POS)+53*(ESPACING)
EMITTING RECT Y (BAR_P) (BAR_WIDTH/2) (BAR_LENGTH/2) (NRAYS) (DIVERGENCE_FAST) (DIVERGENCE_SLOW) ISO SHIFT X (BAR1POS)+54*(ESPACING)
EMITTING RECT Y (BAR_P) (BAR_WIDTH/2) (BAR_LENGTH/2) (NRAYS) (DIVERGENCE_FAST) (DIVERGENCE_SLOW) ISO SHIFT X (BAR1POS)+55*(ESPACING)
EMITTING RECT Y (BAR_P) (BAR_WIDTH/2) (BAR_LENGTH/2) (NRAYS) (DIVERGENCE_FAST) (DIVERGENCE_SLOW) ISO SHIFT X (BAR1POS)+56*(ESPACING)
EMITTING RECT Y (BAR_P) (BAR_WIDTH/2) (BAR_LENGTH/2) (NRAYS) (DIVERGENCE_FAST) (DIVERGENCE_SLOW) ISO SHIFT X (BAR1POS)+57*(ESPACING)
EMITTING RECT Y (BAR_P) (BAR_WIDTH/2) (BAR_LENGTH/2) (NRAYS) (DIVERGENCE_FAST) (DIVERGENCE_SLOW) ISO SHIFT X (BAR1POS)+58*(ESPACING)
EMITTING RECT Y (BAR_P) (BAR_WIDTH/2) (BAR_LENGTH/2) (NRAYS) (DIVERGENCE_FAST) (DIVERGENCE_SLOW) ISO SHIFT X (BAR1POS)+59*(ESPACING)
EMITTING RECT Y (BAR_P) (BAR_WIDTH/2) (BAR_LENGTH/2) (NRAYS) (DIVERGENCE_FAST) (DIVERGENCE_SLOW) ISO SHIFT X (BAR1POS)+60*(ESPACING)
EMITTING RECT Y (BAR_P) (BAR_WIDTH/2) (BAR_LENGTH/2) (NRAYS) (DIVERGENCE_FAST) (DIVERGENCE_SLOW) ISO SHIFT X (BAR1POS)+61*(ESPACING)
EMITTING RECT Y (BAR_P) (BAR_WIDTH/2) (BAR_LENGTH/2) (NRAYS) (DIVERGENCE_FAST) (DIVERGENCE_SLOW) ISO SHIFT X (BAR1POS)+62*(ESPACING)
EMITTING RECT Y (BAR_P) (BAR_WIDTH/2) (BAR_LENGTH/2) (NRAYS) (DIVERGENCE_FAST) (DIVERGENCE_SLOW) ISO SHIFT X (BAR1POS)+63*(ESPACING)
EMITTING RECT Y (BAR_P) (BAR_WIDTH/2) (BAR_LENGTH/2) (NRAYS) (DIVERGENCE_FAST) (DIVERGENCE_SLOW) ISO SHIFT X (BAR1POS)+64*(ESPACING)
EMITTING RECT Y (BAR_P) (BAR_WIDTH/2) (BAR_LENGTH/2) (NRAYS) (DIVERGENCE_FAST) (DIVERGENCE_SLOW) ISO SHIFT X (BAR1POS)+65*(ESPACING)
EMITTING RECT Y (BAR_P) (BAR_WIDTH/2) (BAR_LENGTH/2) (NRAYS) (DIVERGENCE_FAST) (DIVERGENCE_SLOW) ISO SHIFT X (BAR1POS)+66*(ESPACING)
EMITTING RECT Y (BAR_P) (BAR_WIDTH/2) (BAR_LENGTH/2) (NRAYS) (DIVERGENCE_FAST) (DIVERGENCE_SLOW) ISO SHIFT X (BAR1POS)+67*(ESPACING)

EMITTING RECT Y (BAR_P) (BAR_WIDTH/2) (BAR_LENGTH/2) (NRAYS) (DIVERGENCE_FAST) (DIVERGENCE_SLOW) ISO SHIFT X (BAR1POS)+68*(ESPACING)

BAR2POS=(BAR1POS)+68*(ESPACING)+.5
EMITTING RECT Y (BAR_P) (BAR_WIDTH/2) (BAR_LENGTH/2) (NRAYS) (DIVERGENCE_FAST) (DIVERGENCE_SLOW) ISO SHIFT X (BAR2POS)+0*(ESPACING)
EMITTING RECT Y (BAR_P) (BAR_WIDTH/2) (BAR_LENGTH/2) (NRAYS) (DIVERGENCE_FAST) (DIVERGENCE_SLOW) ISO SHIFT X (BAR2POS)+1*(ESPACING)
EMITTING RECT Y (BAR_P) (BAR_WIDTH/2) (BAR_LENGTH/2) (NRAYS) (DIVERGENCE_FAST) (DIVERGENCE_SLOW) ISO SHIFT X (BAR2POS)+2*(ESPACING)
EMITTING RECT Y (BAR_P) (BAR_WIDTH/2) (BAR_LENGTH/2) (NRAYS) (DIVERGENCE_FAST) (DIVERGENCE_SLOW) ISO SHIFT X (BAR2POS)+3*(ESPACING)
EMITTING RECT Y (BAR_P) (BAR_WIDTH/2) (BAR_LENGTH/2) (NRAYS) (DIVERGENCE_FAST) (DIVERGENCE_SLOW) ISO SHIFT X (BAR2POS)+4*(ESPACING)
EMITTING RECT Y (BAR_P) (BAR_WIDTH/2) (BAR_LENGTH/2) (NRAYS) (DIVERGENCE_FAST) (DIVERGENCE_SLOW) ISO SHIFT X (BAR2POS)+5*(ESPACING)
EMITTING RECT Y (BAR_P) (BAR_WIDTH/2) (BAR_LENGTH/2) (NRAYS) (DIVERGENCE_FAST) (DIVERGENCE_SLOW) ISO SHIFT X (BAR2POS)+6*(ESPACING)
EMITTING RECT Y (BAR_P) (BAR_WIDTH/2) (BAR_LENGTH/2) (NRAYS) (DIVERGENCE_FAST) (DIVERGENCE_SLOW) ISO SHIFT X (BAR2POS)+7*(ESPACING)
EMITTING RECT Y (BAR_P) (BAR_WIDTH/2) (BAR_LENGTH/2) (NRAYS) (DIVERGENCE_FAST) (DIVERGENCE_SLOW) ISO SHIFT X (BAR2POS)+8*(ESPACING)
EMITTING RECT Y (BAR_P) (BAR_WIDTH/2) (BAR_LENGTH/2) (NRAYS) (DIVERGENCE_FAST) (DIVERGENCE_SLOW) ISO SHIFT X (BAR2POS)+9*(ESPACING)
EMITTING RECT Y (BAR_P) (BAR_WIDTH/2) (BAR_LENGTH/2) (NRAYS) (DIVERGENCE_FAST) (DIVERGENCE_SLOW) ISO SHIFT X (BAR2POS)+10*(ESPACING)
EMITTING RECT Y (BAR_P) (BAR_WIDTH/2) (BAR_LENGTH/2) (NRAYS) (DIVERGENCE_FAST) (DIVERGENCE_SLOW) ISO SHIFT X (BAR2POS)+11*(ESPACING)
EMITTING RECT Y (BAR_P) (BAR_WIDTH/2) (BAR_LENGTH/2) (NRAYS) (DIVERGENCE_FAST) (DIVERGENCE_SLOW) ISO SHIFT X (BAR2POS)+12*(ESPACING)
EMITTING RECT Y (BAR_P) (BAR_WIDTH/2) (BAR_LENGTH/2) (NRAYS) (DIVERGENCE_FAST) (DIVERGENCE_SLOW) ISO SHIFT X (BAR2POS)+13*(ESPACING)
EMITTING RECT Y (BAR_P) (BAR_WIDTH/2) (BAR_LENGTH/2) (NRAYS) (DIVERGENCE_FAST) (DIVERGENCE_SLOW) ISO SHIFT X (BAR2POS)+14*(ESPACING)
EMITTING RECT Y (BAR_P) (BAR_WIDTH/2) (BAR_LENGTH/2) (NRAYS) (DIVERGENCE_FAST) (DIVERGENCE_SLOW) ISO SHIFT X (BAR2POS)+15*(ESPACING)
EMITTING RECT Y (BAR_P) (BAR_WIDTH/2) (BAR_LENGTH/2) (NRAYS) (DIVERGENCE_FAST) (DIVERGENCE_SLOW) ISO SHIFT X (BAR2POS)+16*(ESPACING)
EMITTING RECT Y (BAR_P) (BAR_WIDTH/2) (BAR_LENGTH/2) (NRAYS) (DIVERGENCE_FAST) (DIVERGENCE_SLOW) ISO SHIFT X (BAR2POS)+17*(ESPACING)
EMITTING RECT Y (BAR_P) (BAR_WIDTH/2) (BAR_LENGTH/2) (NRAYS) (DIVERGENCE_FAST) (DIVERGENCE_SLOW) ISO SHIFT X (BAR2POS)+18*(ESPACING)
EMITTING RECT Y (BAR_P) (BAR_WIDTH/2) (BAR_LENGTH/2) (NRAYS) (DIVERGENCE_FAST) (DIVERGENCE_SLOW) ISO SHIFT X (BAR2POS)+19*(ESPACING)
EMITTING RECT Y (BAR_P) (BAR_WIDTH/2) (BAR_LENGTH/2) (NRAYS) (DIVERGENCE_FAST) (DIVERGENCE_SLOW) ISO SHIFT X (BAR2POS)+20*(ESPACING)
EMITTING RECT Y (BAR_P) (BAR_WIDTH/2) (BAR_LENGTH/2) (NRAYS) (DIVERGENCE_FAST) (DIVERGENCE_SLOW) ISO SHIFT X (BAR2POS)+21*(ESPACING)
EMITTING RECT Y (BAR_P) (BAR_WIDTH/2) (BAR_LENGTH/2) (NRAYS) (DIVERGENCE_FAST) (DIVERGENCE_SLOW) ISO SHIFT X (BAR2POS)+22*(ESPACING)
EMITTING RECT Y (BAR_P) (BAR_WIDTH/2) (BAR_LENGTH/2) (NRAYS) (DIVERGENCE_FAST) (DIVERGENCE_SLOW) ISO SHIFT X (BAR2POS)+23*(ESPACING)
EMITTING RECT Y (BAR_P) (BAR_WIDTH/2) (BAR_LENGTH/2) (NRAYS) (DIVERGENCE_FAST) (DIVERGENCE_SLOW) ISO SHIFT X (BAR2POS)+24*(ESPACING)
EMITTING RECT Y (BAR_P) (BAR_WIDTH/2) (BAR_LENGTH/2) (NRAYS) (DIVERGENCE_FAST) (DIVERGENCE_SLOW) ISO SHIFT X (BAR2POS)+25*(ESPACING)
EMITTING RECT Y (BAR_P) (BAR_WIDTH/2) (BAR_LENGTH/2) (NRAYS) (DIVERGENCE_FAST) (DIVERGENCE_SLOW) ISO SHIFT X (BAR2POS)+26*(ESPACING)
EMITTING RECT Y (BAR_P) (BAR_WIDTH/2) (BAR_LENGTH/2) (NRAYS) (DIVERGENCE_FAST) (DIVERGENCE_SLOW) ISO SHIFT X (BAR2POS)+27*(ESPACING)
EMITTING RECT Y (BAR_P) (BAR_WIDTH/2) (BAR_LENGTH/2) (NRAYS) (DIVERGENCE_FAST) (DIVERGENCE_SLOW) ISO SHIFT X (BAR2POS)+28*(ESPACING)
EMITTING RECT Y (BAR_P) (BAR_WIDTH/2) (BAR_LENGTH/2) (NRAYS) (DIVERGENCE_FAST) (DIVERGENCE_SLOW) ISO SHIFT X (BAR2POS)+29*(ESPACING)
EMITTING RECT Y (BAR_P) (BAR_WIDTH/2) (BAR_LENGTH/2) (NRAYS) (DIVERGENCE_FAST) (DIVERGENCE_SLOW) ISO SHIFT X (BAR2POS)+30*(ESPACING)

EMITTING RECT Y (BAR_P) (BAR_WIDTH/2) (BAR_LENGTH/2) (NRAYS) (DIVERGENCE_FAST) (DIVERGENCE_SLOW) ISO SHIFT X (BAR2POS)+31*(ESPACING)
EMITTING RECT Y (BAR_P) (BAR_WIDTH/2) (BAR_LENGTH/2) (NRAYS) (DIVERGENCE_FAST) (DIVERGENCE_SLOW) ISO SHIFT X (BAR2POS)+32*(ESPACING)
EMITTING RECT Y (BAR_P) (BAR_WIDTH/2) (BAR_LENGTH/2) (NRAYS) (DIVERGENCE_FAST) (DIVERGENCE_SLOW) ISO SHIFT X (BAR2POS)+33*(ESPACING)
EMITTING RECT Y (BAR_P) (BAR_WIDTH/2) (BAR_LENGTH/2) (NRAYS) (DIVERGENCE_FAST) (DIVERGENCE_SLOW) ISO SHIFT X (BAR2POS)+34*(ESPACING)
EMITTING RECT Y (BAR_P) (BAR_WIDTH/2) (BAR_LENGTH/2) (NRAYS) (DIVERGENCE_FAST) (DIVERGENCE_SLOW) ISO SHIFT X (BAR2POS)+35*(ESPACING)
EMITTING RECT Y (BAR_P) (BAR_WIDTH/2) (BAR_LENGTH/2) (NRAYS) (DIVERGENCE_FAST) (DIVERGENCE_SLOW) ISO SHIFT X (BAR2POS)+36*(ESPACING)
EMITTING RECT Y (BAR_P) (BAR_WIDTH/2) (BAR_LENGTH/2) (NRAYS) (DIVERGENCE_FAST) (DIVERGENCE_SLOW) ISO SHIFT X (BAR2POS)+37*(ESPACING)
EMITTING RECT Y (BAR_P) (BAR_WIDTH/2) (BAR_LENGTH/2) (NRAYS) (DIVERGENCE_FAST) (DIVERGENCE_SLOW) ISO SHIFT X (BAR2POS)+38*(ESPACING)
EMITTING RECT Y (BAR_P) (BAR_WIDTH/2) (BAR_LENGTH/2) (NRAYS) (DIVERGENCE_FAST) (DIVERGENCE_SLOW) ISO SHIFT X (BAR2POS)+39*(ESPACING)
EMITTING RECT Y (BAR_P) (BAR_WIDTH/2) (BAR_LENGTH/2) (NRAYS) (DIVERGENCE_FAST) (DIVERGENCE_SLOW) ISO SHIFT X (BAR2POS)+40*(ESPACING)
EMITTING RECT Y (BAR_P) (BAR_WIDTH/2) (BAR_LENGTH/2) (NRAYS) (DIVERGENCE_FAST) (DIVERGENCE_SLOW) ISO SHIFT X (BAR2POS)+41*(ESPACING)
EMITTING RECT Y (BAR_P) (BAR_WIDTH/2) (BAR_LENGTH/2) (NRAYS) (DIVERGENCE_FAST) (DIVERGENCE_SLOW) ISO SHIFT X (BAR2POS)+42*(ESPACING)
EMITTING RECT Y (BAR_P) (BAR_WIDTH/2) (BAR_LENGTH/2) (NRAYS) (DIVERGENCE_FAST) (DIVERGENCE_SLOW) ISO SHIFT X (BAR2POS)+43*(ESPACING)
EMITTING RECT Y (BAR_P) (BAR_WIDTH/2) (BAR_LENGTH/2) (NRAYS) (DIVERGENCE_FAST) (DIVERGENCE_SLOW) ISO SHIFT X (BAR2POS)+44*(ESPACING)
EMITTING RECT Y (BAR_P) (BAR_WIDTH/2) (BAR_LENGTH/2) (NRAYS) (DIVERGENCE_FAST) (DIVERGENCE_SLOW) ISO SHIFT X (BAR2POS)+45*(ESPACING)
EMITTING RECT Y (BAR_P) (BAR_WIDTH/2) (BAR_LENGTH/2) (NRAYS) (DIVERGENCE_FAST) (DIVERGENCE_SLOW) ISO SHIFT X (BAR2POS)+46*(ESPACING)
EMITTING RECT Y (BAR_P) (BAR_WIDTH/2) (BAR_LENGTH/2) (NRAYS) (DIVERGENCE_FAST) (DIVERGENCE_SLOW) ISO SHIFT X (BAR2POS)+47*(ESPACING)
EMITTING RECT Y (BAR_P) (BAR_WIDTH/2) (BAR_LENGTH/2) (NRAYS) (DIVERGENCE_FAST) (DIVERGENCE_SLOW) ISO SHIFT X (BAR2POS)+48*(ESPACING)
EMITTING RECT Y (BAR_P) (BAR_WIDTH/2) (BAR_LENGTH/2) (NRAYS) (DIVERGENCE_FAST) (DIVERGENCE_SLOW) ISO SHIFT X (BAR2POS)+49*(ESPACING)
EMITTING RECT Y (BAR_P) (BAR_WIDTH/2) (BAR_LENGTH/2) (NRAYS) (DIVERGENCE_FAST) (DIVERGENCE_SLOW) ISO SHIFT X (BAR2POS)+50*(ESPACING)
EMITTING RECT Y (BAR_P) (BAR_WIDTH/2) (BAR_LENGTH/2) (NRAYS) (DIVERGENCE_FAST) (DIVERGENCE_SLOW) ISO SHIFT X (BAR2POS)+51*(ESPACING)
EMITTING RECT Y (BAR_P) (BAR_WIDTH/2) (BAR_LENGTH/2) (NRAYS) (DIVERGENCE_FAST) (DIVERGENCE_SLOW) ISO SHIFT X (BAR2POS)+52*(ESPACING)
EMITTING RECT Y (BAR_P) (BAR_WIDTH/2) (BAR_LENGTH/2) (NRAYS) (DIVERGENCE_FAST) (DIVERGENCE_SLOW) ISO SHIFT X (BAR2POS)+53*(ESPACING)
EMITTING RECT Y (BAR_P) (BAR_WIDTH/2) (BAR_LENGTH/2) (NRAYS) (DIVERGENCE_FAST) (DIVERGENCE_SLOW) ISO SHIFT X (BAR2POS)+54*(ESPACING)
EMITTING RECT Y (BAR_P) (BAR_WIDTH/2) (BAR_LENGTH/2) (NRAYS) (DIVERGENCE_FAST) (DIVERGENCE_SLOW) ISO SHIFT X (BAR2POS)+55*(ESPACING)
EMITTING RECT Y (BAR_P) (BAR_WIDTH/2) (BAR_LENGTH/2) (NRAYS) (DIVERGENCE_FAST) (DIVERGENCE_SLOW) ISO SHIFT X (BAR2POS)+56*(ESPACING)
EMITTING RECT Y (BAR_P) (BAR_WIDTH/2) (BAR_LENGTH/2) (NRAYS) (DIVERGENCE_FAST) (DIVERGENCE_SLOW) ISO SHIFT X (BAR2POS)+57*(ESPACING)
EMITTING RECT Y (BAR_P) (BAR_WIDTH/2) (BAR_LENGTH/2) (NRAYS) (DIVERGENCE_FAST) (DIVERGENCE_SLOW) ISO SHIFT X (BAR2POS)+58*(ESPACING)
EMITTING RECT Y (BAR_P) (BAR_WIDTH/2) (BAR_LENGTH/2) (NRAYS) (DIVERGENCE_FAST) (DIVERGENCE_SLOW) ISO SHIFT X (BAR2POS)+59*(ESPACING)
EMITTING RECT Y (BAR_P) (BAR_WIDTH/2) (BAR_LENGTH/2) (NRAYS) (DIVERGENCE_FAST) (DIVERGENCE_SLOW) ISO SHIFT X (BAR2POS)+60*(ESPACING)
EMITTING RECT Y (BAR_P) (BAR_WIDTH/2) (BAR_LENGTH/2) (NRAYS) (DIVERGENCE_FAST) (DIVERGENCE_SLOW) ISO SHIFT X (BAR2POS)+61*(ESPACING)
EMITTING RECT Y (BAR_P) (BAR_WIDTH/2) (BAR_LENGTH/2) (NRAYS) (DIVERGENCE_FAST) (DIVERGENCE_SLOW) ISO SHIFT X (BAR2POS)+62*(ESPACING)
EMITTING RECT Y (BAR_P) (BAR_WIDTH/2) (BAR_LENGTH/2) (NRAYS) (DIVERGENCE_FAST) (DIVERGENCE_SLOW) ISO SHIFT X (BAR2POS)+63*(ESPACING)

EMITTING RECT Y (BAR_P) (BAR_WIDTH/2) (BAR_LENGTH/2) (NRAYS) (DIVERGENCE_FAST) (DIVERGENCE_SLOW) ISO SHIFT X (BAR2POS)+64*(ESPACING)
EMITTING RECT Y (BAR_P) (BAR_WIDTH/2) (BAR_LENGTH/2) (NRAYS) (DIVERGENCE_FAST) (DIVERGENCE_SLOW) ISO SHIFT X (BAR2POS)+65*(ESPACING)
EMITTING RECT Y (BAR_P) (BAR_WIDTH/2) (BAR_LENGTH/2) (NRAYS) (DIVERGENCE_FAST) (DIVERGENCE_SLOW) ISO SHIFT X (BAR2POS)+66*(ESPACING)
EMITTING RECT Y (BAR_P) (BAR_WIDTH/2) (BAR_LENGTH/2) (NRAYS) (DIVERGENCE_FAST) (DIVERGENCE_SLOW) ISO SHIFT X (BAR2POS)+67*(ESPACING)
EMITTING RECT Y (BAR_P) (BAR_WIDTH/2) (BAR_LENGTH/2) (NRAYS) (DIVERGENCE_FAST) (DIVERGENCE_SLOW) ISO SHIFT X (BAR2POS)+68*(ESPACING)

BAR3POS=(BAR2POS)+68*(ESPACING)+.5
EMITTING RECT Y (BAR_P) (BAR_WIDTH/2) (BAR_LENGTH/2) (NRAYS) (DIVERGENCE_FAST) (DIVERGENCE_SLOW) ISO SHIFT X (BAR3POS)+0*(ESPACING)
EMITTING RECT Y (BAR_P) (BAR_WIDTH/2) (BAR_LENGTH/2) (NRAYS) (DIVERGENCE_FAST) (DIVERGENCE_SLOW) ISO SHIFT X (BAR3POS)+1*(ESPACING)
EMITTING RECT Y (BAR_P) (BAR_WIDTH/2) (BAR_LENGTH/2) (NRAYS) (DIVERGENCE_FAST) (DIVERGENCE_SLOW) ISO SHIFT X (BAR3POS)+2*(ESPACING)
EMITTING RECT Y (BAR_P) (BAR_WIDTH/2) (BAR_LENGTH/2) (NRAYS) (DIVERGENCE_FAST) (DIVERGENCE_SLOW) ISO SHIFT X (BAR3POS)+3*(ESPACING)
EMITTING RECT Y (BAR_P) (BAR_WIDTH/2) (BAR_LENGTH/2) (NRAYS) (DIVERGENCE_FAST) (DIVERGENCE_SLOW) ISO SHIFT X (BAR3POS)+4*(ESPACING)
EMITTING RECT Y (BAR_P) (BAR_WIDTH/2) (BAR_LENGTH/2) (NRAYS) (DIVERGENCE_FAST) (DIVERGENCE_SLOW) ISO SHIFT X (BAR3POS)+5*(ESPACING)
EMITTING RECT Y (BAR_P) (BAR_WIDTH/2) (BAR_LENGTH/2) (NRAYS) (DIVERGENCE_FAST) (DIVERGENCE_SLOW) ISO SHIFT X (BAR3POS)+6*(ESPACING)
EMITTING RECT Y (BAR_P) (BAR_WIDTH/2) (BAR_LENGTH/2) (NRAYS) (DIVERGENCE_FAST) (DIVERGENCE_SLOW) ISO SHIFT X (BAR3POS)+7*(ESPACING)
EMITTING RECT Y (BAR_P) (BAR_WIDTH/2) (BAR_LENGTH/2) (NRAYS) (DIVERGENCE_FAST) (DIVERGENCE_SLOW) ISO SHIFT X (BAR3POS)+8*(ESPACING)
EMITTING RECT Y (BAR_P) (BAR_WIDTH/2) (BAR_LENGTH/2) (NRAYS) (DIVERGENCE_FAST) (DIVERGENCE_SLOW) ISO SHIFT X (BAR3POS)+9*(ESPACING)
EMITTING RECT Y (BAR_P) (BAR_WIDTH/2) (BAR_LENGTH/2) (NRAYS) (DIVERGENCE_FAST) (DIVERGENCE_SLOW) ISO SHIFT X (BAR3POS)+10*(ESPACING)
EMITTING RECT Y (BAR_P) (BAR_WIDTH/2) (BAR_LENGTH/2) (NRAYS) (DIVERGENCE_FAST) (DIVERGENCE_SLOW) ISO SHIFT X (BAR3POS)+11*(ESPACING)
EMITTING RECT Y (BAR_P) (BAR_WIDTH/2) (BAR_LENGTH/2) (NRAYS) (DIVERGENCE_FAST) (DIVERGENCE_SLOW) ISO SHIFT X (BAR3POS)+12*(ESPACING)
EMITTING RECT Y (BAR_P) (BAR_WIDTH/2) (BAR_LENGTH/2) (NRAYS) (DIVERGENCE_FAST) (DIVERGENCE_SLOW) ISO SHIFT X (BAR3POS)+13*(ESPACING)
EMITTING RECT Y (BAR_P) (BAR_WIDTH/2) (BAR_LENGTH/2) (NRAYS) (DIVERGENCE_FAST) (DIVERGENCE_SLOW) ISO SHIFT X (BAR3POS)+14*(ESPACING)
EMITTING RECT Y (BAR_P) (BAR_WIDTH/2) (BAR_LENGTH/2) (NRAYS) (DIVERGENCE_FAST) (DIVERGENCE_SLOW) ISO SHIFT X (BAR3POS)+15*(ESPACING)
EMITTING RECT Y (BAR_P) (BAR_WIDTH/2) (BAR_LENGTH/2) (NRAYS) (DIVERGENCE_FAST) (DIVERGENCE_SLOW) ISO SHIFT X (BAR3POS)+16*(ESPACING)
EMITTING RECT Y (BAR_P) (BAR_WIDTH/2) (BAR_LENGTH/2) (NRAYS) (DIVERGENCE_FAST) (DIVERGENCE_SLOW) ISO SHIFT X (BAR3POS)+17*(ESPACING)
EMITTING RECT Y (BAR_P) (BAR_WIDTH/2) (BAR_LENGTH/2) (NRAYS) (DIVERGENCE_FAST) (DIVERGENCE_SLOW) ISO SHIFT X (BAR3POS)+18*(ESPACING)
EMITTING RECT Y (BAR_P) (BAR_WIDTH/2) (BAR_LENGTH/2) (NRAYS) (DIVERGENCE_FAST) (DIVERGENCE_SLOW) ISO SHIFT X (BAR3POS)+19*(ESPACING)
EMITTING RECT Y (BAR_P) (BAR_WIDTH/2) (BAR_LENGTH/2) (NRAYS) (DIVERGENCE_FAST) (DIVERGENCE_SLOW) ISO SHIFT X (BAR3POS)+20*(ESPACING)
EMITTING RECT Y (BAR_P) (BAR_WIDTH/2) (BAR_LENGTH/2) (NRAYS) (DIVERGENCE_FAST) (DIVERGENCE_SLOW) ISO SHIFT X (BAR3POS)+21*(ESPACING)
EMITTING RECT Y (BAR_P) (BAR_WIDTH/2) (BAR_LENGTH/2) (NRAYS) (DIVERGENCE_FAST) (DIVERGENCE_SLOW) ISO SHIFT X (BAR3POS)+22*(ESPACING)
EMITTING RECT Y (BAR_P) (BAR_WIDTH/2) (BAR_LENGTH/2) (NRAYS) (DIVERGENCE_FAST) (DIVERGENCE_SLOW) ISO SHIFT X (BAR3POS)+23*(ESPACING)
EMITTING RECT Y (BAR_P) (BAR_WIDTH/2) (BAR_LENGTH/2) (NRAYS) (DIVERGENCE_FAST) (DIVERGENCE_SLOW) ISO SHIFT X (BAR3POS)+24*(ESPACING)
EMITTING RECT Y (BAR_P) (BAR_WIDTH/2) (BAR_LENGTH/2) (NRAYS) (DIVERGENCE_FAST) (DIVERGENCE_SLOW) ISO SHIFT X (BAR3POS)+25*(ESPACING)
EMITTING RECT Y (BAR_P) (BAR_WIDTH/2) (BAR_LENGTH/2) (NRAYS) (DIVERGENCE_FAST) (DIVERGENCE_SLOW) ISO SHIFT X (BAR3POS)+26*(ESPACING)

EMITTING RECT Y (BAR_P) (BAR_WIDTH/2) (BAR_LENGTH/2) (NRAYS) (DIVERGENCE_FAST) (DIVERGENCE_SLOW) ISO SHIFT X (BAR3POS)+27*(ESPACING)
EMITTING RECT Y (BAR_P) (BAR_WIDTH/2) (BAR_LENGTH/2) (NRAYS) (DIVERGENCE_FAST) (DIVERGENCE_SLOW) ISO SHIFT X (BAR3POS)+28*(ESPACING)
EMITTING RECT Y (BAR_P) (BAR_WIDTH/2) (BAR_LENGTH/2) (NRAYS) (DIVERGENCE_FAST) (DIVERGENCE_SLOW) ISO SHIFT X (BAR3POS)+29*(ESPACING)
EMITTING RECT Y (BAR_P) (BAR_WIDTH/2) (BAR_LENGTH/2) (NRAYS) (DIVERGENCE_FAST) (DIVERGENCE_SLOW) ISO SHIFT X (BAR3POS)+30*(ESPACING)
EMITTING RECT Y (BAR_P) (BAR_WIDTH/2) (BAR_LENGTH/2) (NRAYS) (DIVERGENCE_FAST) (DIVERGENCE_SLOW) ISO SHIFT X (BAR3POS)+31*(ESPACING)
EMITTING RECT Y (BAR_P) (BAR_WIDTH/2) (BAR_LENGTH/2) (NRAYS) (DIVERGENCE_FAST) (DIVERGENCE_SLOW) ISO SHIFT X (BAR3POS)+32*(ESPACING)
EMITTING RECT Y (BAR_P) (BAR_WIDTH/2) (BAR_LENGTH/2) (NRAYS) (DIVERGENCE_FAST) (DIVERGENCE_SLOW) ISO SHIFT X (BAR3POS)+33*(ESPACING)
EMITTING RECT Y (BAR_P) (BAR_WIDTH/2) (BAR_LENGTH/2) (NRAYS) (DIVERGENCE_FAST) (DIVERGENCE_SLOW) ISO SHIFT X (BAR3POS)+34*(ESPACING)
EMITTING RECT Y (BAR_P) (BAR_WIDTH/2) (BAR_LENGTH/2) (NRAYS) (DIVERGENCE_FAST) (DIVERGENCE_SLOW) ISO SHIFT X (BAR3POS)+35*(ESPACING)
EMITTING RECT Y (BAR_P) (BAR_WIDTH/2) (BAR_LENGTH/2) (NRAYS) (DIVERGENCE_FAST) (DIVERGENCE_SLOW) ISO SHIFT X (BAR3POS)+36*(ESPACING)
EMITTING RECT Y (BAR_P) (BAR_WIDTH/2) (BAR_LENGTH/2) (NRAYS) (DIVERGENCE_FAST) (DIVERGENCE_SLOW) ISO SHIFT X (BAR3POS)+37*(ESPACING)
EMITTING RECT Y (BAR_P) (BAR_WIDTH/2) (BAR_LENGTH/2) (NRAYS) (DIVERGENCE_FAST) (DIVERGENCE_SLOW) ISO SHIFT X (BAR3POS)+38*(ESPACING)
EMITTING RECT Y (BAR_P) (BAR_WIDTH/2) (BAR_LENGTH/2) (NRAYS) (DIVERGENCE_FAST) (DIVERGENCE_SLOW) ISO SHIFT X (BAR3POS)+39*(ESPACING)
EMITTING RECT Y (BAR_P) (BAR_WIDTH/2) (BAR_LENGTH/2) (NRAYS) (DIVERGENCE_FAST) (DIVERGENCE_SLOW) ISO SHIFT X (BAR3POS)+40*(ESPACING)
EMITTING RECT Y (BAR_P) (BAR_WIDTH/2) (BAR_LENGTH/2) (NRAYS) (DIVERGENCE_FAST) (DIVERGENCE_SLOW) ISO SHIFT X (BAR3POS)+41*(ESPACING)
EMITTING RECT Y (BAR_P) (BAR_WIDTH/2) (BAR_LENGTH/2) (NRAYS) (DIVERGENCE_FAST) (DIVERGENCE_SLOW) ISO SHIFT X (BAR3POS)+42*(ESPACING)
EMITTING RECT Y (BAR_P) (BAR_WIDTH/2) (BAR_LENGTH/2) (NRAYS) (DIVERGENCE_FAST) (DIVERGENCE_SLOW) ISO SHIFT X (BAR3POS)+43*(ESPACING)
EMITTING RECT Y (BAR_P) (BAR_WIDTH/2) (BAR_LENGTH/2) (NRAYS) (DIVERGENCE_FAST) (DIVERGENCE_SLOW) ISO SHIFT X (BAR3POS)+44*(ESPACING)
EMITTING RECT Y (BAR_P) (BAR_WIDTH/2) (BAR_LENGTH/2) (NRAYS) (DIVERGENCE_FAST) (DIVERGENCE_SLOW) ISO SHIFT X (BAR3POS)+45*(ESPACING)
EMITTING RECT Y (BAR_P) (BAR_WIDTH/2) (BAR_LENGTH/2) (NRAYS) (DIVERGENCE_FAST) (DIVERGENCE_SLOW) ISO SHIFT X (BAR3POS)+46*(ESPACING)
EMITTING RECT Y (BAR_P) (BAR_WIDTH/2) (BAR_LENGTH/2) (NRAYS) (DIVERGENCE_FAST) (DIVERGENCE_SLOW) ISO SHIFT X (BAR3POS)+47*(ESPACING)
EMITTING RECT Y (BAR_P) (BAR_WIDTH/2) (BAR_LENGTH/2) (NRAYS) (DIVERGENCE_FAST) (DIVERGENCE_SLOW) ISO SHIFT X (BAR3POS)+48*(ESPACING)
EMITTING RECT Y (BAR_P) (BAR_WIDTH/2) (BAR_LENGTH/2) (NRAYS) (DIVERGENCE_FAST) (DIVERGENCE_SLOW) ISO SHIFT X (BAR3POS)+49*(ESPACING)
EMITTING RECT Y (BAR_P) (BAR_WIDTH/2) (BAR_LENGTH/2) (NRAYS) (DIVERGENCE_FAST) (DIVERGENCE_SLOW) ISO SHIFT X (BAR3POS)+50*(ESPACING)
EMITTING RECT Y (BAR_P) (BAR_WIDTH/2) (BAR_LENGTH/2) (NRAYS) (DIVERGENCE_FAST) (DIVERGENCE_SLOW) ISO SHIFT X (BAR3POS)+51*(ESPACING)
EMITTING RECT Y (BAR_P) (BAR_WIDTH/2) (BAR_LENGTH/2) (NRAYS) (DIVERGENCE_FAST) (DIVERGENCE_SLOW) ISO SHIFT X (BAR3POS)+52*(ESPACING)
EMITTING RECT Y (BAR_P) (BAR_WIDTH/2) (BAR_LENGTH/2) (NRAYS) (DIVERGENCE_FAST) (DIVERGENCE_SLOW) ISO SHIFT X (BAR3POS)+53*(ESPACING)
EMITTING RECT Y (BAR_P) (BAR_WIDTH/2) (BAR_LENGTH/2) (NRAYS) (DIVERGENCE_FAST) (DIVERGENCE_SLOW) ISO SHIFT X (BAR3POS)+54*(ESPACING)
EMITTING RECT Y (BAR_P) (BAR_WIDTH/2) (BAR_LENGTH/2) (NRAYS) (DIVERGENCE_FAST) (DIVERGENCE_SLOW) ISO SHIFT X (BAR3POS)+55*(ESPACING)
EMITTING RECT Y (BAR_P) (BAR_WIDTH/2) (BAR_LENGTH/2) (NRAYS) (DIVERGENCE_FAST) (DIVERGENCE_SLOW) ISO SHIFT X (BAR3POS)+56*(ESPACING)
EMITTING RECT Y (BAR_P) (BAR_WIDTH/2) (BAR_LENGTH/2) (NRAYS) (DIVERGENCE_FAST) (DIVERGENCE_SLOW) ISO SHIFT X (BAR3POS)+57*(ESPACING)
EMITTING RECT Y (BAR_P) (BAR_WIDTH/2) (BAR_LENGTH/2) (NRAYS) (DIVERGENCE_FAST) (DIVERGENCE_SLOW) ISO SHIFT X (BAR3POS)+58*(ESPACING)
EMITTING RECT Y (BAR_P) (BAR_WIDTH/2) (BAR_LENGTH/2) (NRAYS) (DIVERGENCE_FAST) (DIVERGENCE_SLOW) ISO SHIFT X (BAR3POS)+59*(ESPACING)

```
EMITTING RECT Y (BAR_P) (BAR_WIDTH/2) (BAR_LENGTH/2) (NRAYS) (DIVERGENCE_FAST) (DIVERGENCE_SLOW)     ISO
SHIFT X (BAR3POS)+60*(ESPACING)
EMITTING RECT Y (BAR_P) (BAR_WIDTH/2) (BAR_LENGTH/2) (NRAYS) (DIVERGENCE_FAST) (DIVERGENCE_SLOW)     ISO
SHIFT X (BAR3POS)+61*(ESPACING)
EMITTING RECT Y (BAR_P) (BAR_WIDTH/2) (BAR_LENGTH/2) (NRAYS) (DIVERGENCE_FAST) (DIVERGENCE_SLOW)     ISO
SHIFT X (BAR3POS)+62*(ESPACING)
EMITTING RECT Y (BAR_P) (BAR_WIDTH/2) (BAR_LENGTH/2) (NRAYS) (DIVERGENCE_FAST) (DIVERGENCE_SLOW)     ISO
SHIFT X (BAR3POS)+63*(ESPACING)
EMITTING RECT Y (BAR_P) (BAR_WIDTH/2) (BAR_LENGTH/2) (NRAYS) (DIVERGENCE_FAST) (DIVERGENCE_SLOW)     ISO
SHIFT X (BAR3POS)+64*(ESPACING)
EMITTING RECT Y (BAR_P) (BAR_WIDTH/2) (BAR_LENGTH/2) (NRAYS) (DIVERGENCE_FAST) (DIVERGENCE_SLOW)     ISO
SHIFT X (BAR3POS)+65*(ESPACING)
EMITTING RECT Y (BAR_P) (BAR_WIDTH/2) (BAR_LENGTH/2) (NRAYS) (DIVERGENCE_FAST) (DIVERGENCE_SLOW)     ISO
SHIFT X (BAR3POS)+66*(ESPACING)
EMITTING RECT Y (BAR_P) (BAR_WIDTH/2) (BAR_LENGTH/2) (NRAYS) (DIVERGENCE_FAST) (DIVERGENCE_SLOW)     ISO
SHIFT X (BAR3POS)+67*(ESPACING)
EMITTING RECT Y (BAR_P) (BAR_WIDTH/2) (BAR_LENGTH/2) (NRAYS) (DIVERGENCE_FAST) (DIVERGENCE_SLOW)     ISO
SHIFT X (BAR3POS)+68*(ESPACING)
FLUX TOTAL 150


!!WINDOW Z X
!!PLOT RAYS 1

PIXELS 101
WINDOW Y Z
!! TRACE RAYS WITH OPTIONAL PLOT
!!PLOT BEAMS
!!PLOT RAYS
!!$VIEW
!!DUMP
!!$VIEW LASTDUMP.DIS


!! ANALYSIS BLOCK BEGINS HERE
VOXELS ABSORBED 0 (FLENGTH) -4@(CORED/2) 101 25 25
MISSED .5

TRACE PLOT 10000 OVERLAY
PLOT FACETS

$COPY 9 ABS_FLUX.DIS !! Copies default bro009.dat to named file
STATS
$VIEW
&VIEW ABS_FLUX.DIS  !! Adds the volume distribution to 3D viewer
!! Hide (H) sides of box in viewer to see VOXELS data.
!! Use 8 and 9 keys to move selected planes or Shift-Drag.
RETURN

!!PATHS
!!WINDOW X Y
!!SELECT ONLY PATH 2
!!PROFILES OVERLAY
!!HISTORY PLOT
!!SPOTS POSITION
```

APPENDIX B – SCHEMATIC FOR FIBER V-GROOVE AND COOLING BLOCK

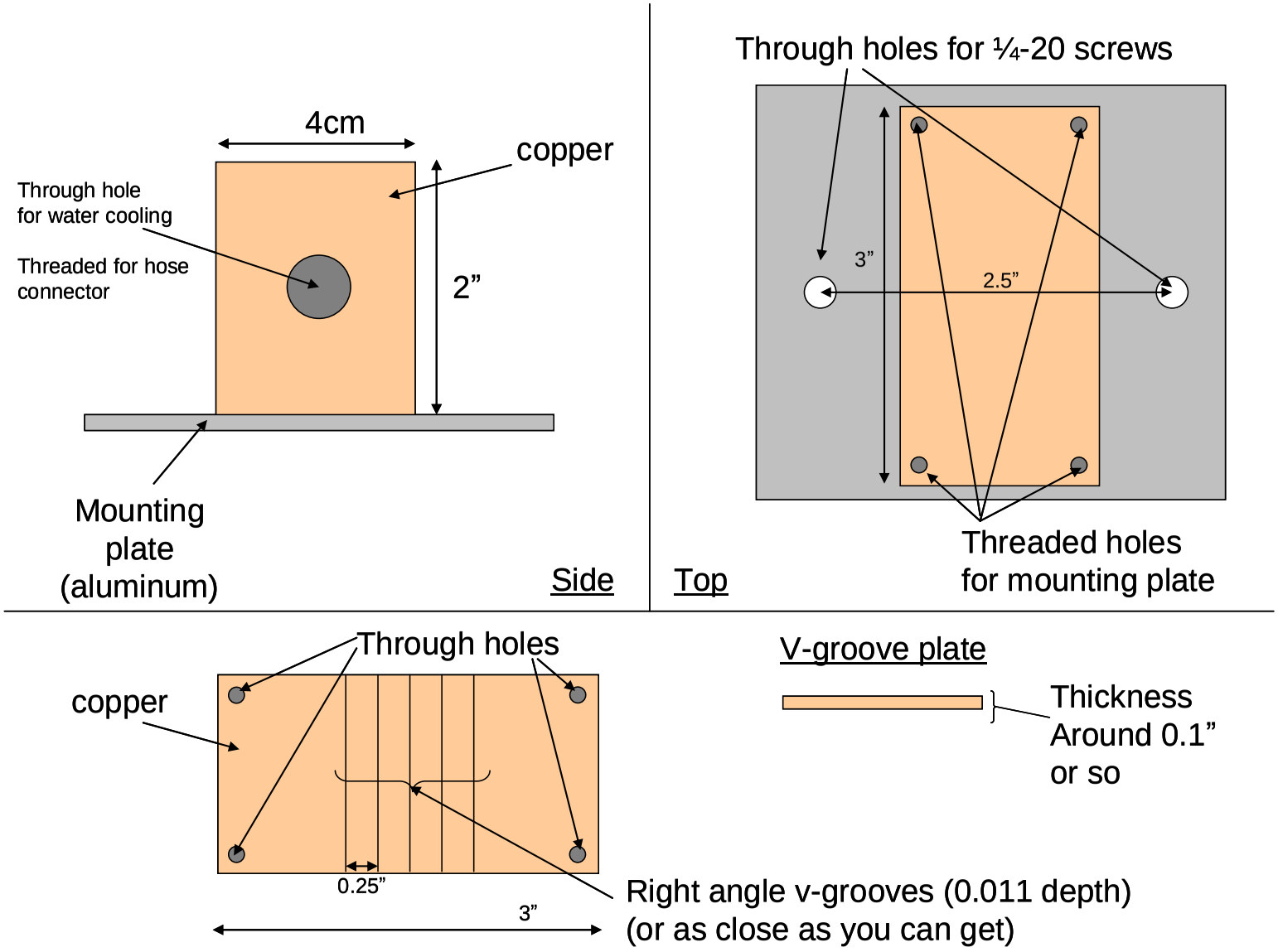
4cm
copper
Through hole
for water cooling
Threaded for hose
connector
2”
Mounting
plate
(aluminum)
Side
Through holes for ¼-20 screws
3”
2.5”
Threaded holes
for mounting plate
Top
Through holes
copper
0.25”
3”
Right angle v-grooves (0.011 depth)
(or as close as you can get)
V-groove plate
Thickness
Around 0.1”
or so

APPENDIX C – RATE EQUATION MODELING CODE

Generator of long pulse temporal output power data

```
function
[out,eout,outconv]=longpulse(temperature,spl,eta,detadT,sigmaer,dsigemissdT,p
umpenergy)
% Longpulse Rate Equation Integrator
% dflux/dt=(flux)*c*n*(l/l')sigma-(L-lnR)/(res lifetime)+(l/l')*n*omega/tau
% dn/dt = P*eff/(hv)-gamma*n*c*flux*sigma
% Pout = (1-R1)/(1+R1)*A*hv*c*flux
tic
%constants
c=2.998e8;                          %speed of light (m/s)
h=6.626e-34;                        %plank's constant (J*s)
k=1.380658e-23;                      %boltzmann's constant (J/K)

%material properties
peakwave=1.533e-6;                  %peak emission cross section wavelength (m)
wavelengther=1.555e-6;              %laser emission wavelength (m)
wavelengthcr=.65e-6;                %pump band wavelength (m)
penergyer=h*c/wavelengther;         %energy of laser photon (J)
penergycr=h*c/wavelengthcr;         %energy of pump photon (J)
penergypeak=h*c/peakwave;           %energy of peak cross section wavelength (J)
%sigmaer=5e-25;                      %stimulated emission cross section at 20C
(m)
sigmacr=5e-26;                      %absorption cross section of pump (m)
gamma=2.2;                            %degeneracy factor
tau21=8e-3;                         %lifetime of emission transition
tau30=3e-3;                         %lifetime of pump transition
tautran=204e-6;                     %transfer lifetime from pump to emission band
ntoter=1.2e25;                      %ion density of lasing ion (#/m^3)
ntotcr=1.2e26;                      %ion density of pump ion (#/m^3)


% resonator properties
R1=.8;                             %output coupler reflectivity
R2=.99;                               %reflectivity of HR mirror
l=.03;                              %gain material length (m)
lprime=15e-2;                       %resonator length (m)
%spl=.02;                            %single pass loss
dia=.003;                           %rod diameter (m)
area=pi()*(dia/2)^2;                %rod cross sectional area (m^2)
zeta=1.05;                            %mode overlap parameter
marea=zeta*area;                    %effective cross sectional area of laser mode
in cavity
L=-2*log(1-spl);                    %double pass logritmic loss
epsilon=L-log(R1*R2);               %loss factor
reslife=2*lprime/c;                 %resonator lifetime (s)
omega=2*marea/(lprime/2)^2;          %solid angle of resonant mode for
spontaneous emission

%initial conditions
```

```
n1=ntoter;                          %initial occupation of lower laser level
(#/m^3)
n2=0;                               %initial occupation of upper laser lavel
(#/m^3)
n0=ntotcr;                          %initial occupation of lower pump level
(#/m^3)
n3=0;                               %initial occupation of upper pump level
(#/m^3)
%flux=0;
flux=1/(marea*l);                    %initial photon density in cavity (#/m^3)
n=n2-(gamma-1)*n1;                  %initial inversion (#/m^3)

%pump properties
%eta=.0047;                             %pump efficiency at 20C
%pumpenergy=28;                         %energy in pump pulse
pumptime=800e-6;                       %length of pump pulse
Pmax=pumpenergy/(.75*pumptime);        %peak power of pump pulse
%pumppower=pumpenergy/pumptime;

%timestep
totaltime=1.8e-3;%pumptime*1.25+tautran;        %total integration time
step=totaltime/1000;                            %default time step

%temperature dependent variables
%dsigemissdT=0;
%rate of change of emssion cross section per Kelvin
sigmaer=(temperature-20)*dsigemissdT+sigmaer;
%emssion cross section is equal to (delta_sigma + sigma)
sigmaerabs=sigmaer*exp(-(penergypeak-penergyer)/(k*(temperature+273.15)));
%absorption cross section from emission cross section using reciprocity
%detadT=-.00001;
%rate of change in pump efficiency per degree C
eta=eta+(temperature-20)*detadT;
%pump efficiency at given temperature

%calculation
j=1;
time=0;                                         %elapsed time (initially set
to zero)
timestep=1e-10;                                  %starting timestep (s)
out(1,1)=time;
out(1,2)=n;
out(1,3)=flux;
out(1,4)=(1-R1)/(1+R1)*marea*penergyer*c*flux;
while time<totaltime
    if time<=(0.0625*pumptime)
% creates pump power distribution
        pumppower=time*Pmax/(.0625*pumptime);
%
    elseif time>(0.0625*pumptime)&&time<=(.9375*pumptime)
%
            pumppower=(-0.4*Pmax*8*(time-.0625*pumptime)/(7*pumptime))+Pmax;
%
```

```
    elseif time>(.9375*pumptime)&&time<=pumptime
%
            pumppower=-.6*Pmax*(time-
0.9375*pumptime)/(0.0625*pumptime)+0.6*Pmax;           %
    else
%
        pumppower=0;
%
    end
%
    dfluxdt=flux*c*(n2*sigmaer-(gamma-1)*n1*sigmaerabs)*(l/lprime)*zeta-
flux*epsilon/reslife+n2*(l/lprime)*omega/tau21;  %  numerical integration
    dn3dt=pumppower*eta*sigmacr*n0/(penergycr*area*l)-n3/tau30-n3/tautran;
%       |
    dn2dt=n3/tautran-n2/tau21-(n2*sigmaer-(gamma-1)*n1*sigmaerabs)*c*flux;
%       |
    dn1dt=-dn2dt;
%       v
    dn0dt=-dn3dt;
    dflux=dfluxdt*timestep;
    dn3=dn3dt*timestep;
    dn2=dn2dt*timestep;
    dn1=dn1dt*timestep;
    dn0=dn0dt*timestep;
    newn3=n3+dn3;
    newn2=n2+dn2;
    newn1=n1+dn1;
    newn0=n0+dn0;
    newn=newn2-(gamma-1)*newn1;
%       ^
    newflux=flux+dflux;
%       |
    newtime=time+timestep;
%       |
    Pout=(1-R1)/(1+R1)*area*penergyer*c*newflux;
%       |


    if ((j==1)||((abs((newn-n)/n)<.1)&&(abs((newflux-
flux)/flux)<.1))||(timestep<1e-12))&&newflux>0         % if values of n and
flux
        out(j+1,1)=newtime;
% are stable, or time step is
        out(j+1,2)=newn;
% too small the load values into
        out(j+1,3)=newflux;
% output matrix
        out(j+1,4)=Pout;
        out(j+1,5)=pumppower;
        time=newtime;
        n3=newn3;
        n2=newn2;
        n1=newn1;
```

```
        n0=newn0;
        n=newn;
        flux=newflux;
        timestep=step;
        j=j+1;
    else
        timestep=timestep/2;
% if not, then halve the time step
    end
% and try again
    %time
end
j
%calculate total enrgy in output pulse
for i=1:(j-1)
    dpower(i)=(out(i+1,4)+out(i,4))/2;
    dtime(i)=out(i+1,1)-out(i,1);
    energy(i)=dpower(i)*dtime(i);
end
eout=sum(energy);               %total energy in output pulse

%resample data and create even time steps
numrsteps=10000;
%number of steps in new array
rstep=totaltime/numrsteps;
%time increment of new step
detector=rc(20e-6,rstep,totaltime);
%create detector response data
[num,j]=size(out);
%determine size of initial data array
j=0;
for i=1:(numrsteps)
    rtime=rstep*(i-1);
    for j=1:(num-1)
%create new, resampled array called newout
    if rtime>out(j,1)&&rtime<out(j+1,1)
%
        dy=out(j+1,4)-out(j,4);
%
        dt=out(j+1,1)-out(j,1);
%
        newdt=rtime-out(j,1);
%
        newdy=newdt*dy/dt;
%
        newy=out(j,4)+newdy;
%
        newout(i,1)=rtime;
%
        newout(i,2)=newy;
%
    elseif time==0
%
```

```
            newout(i,1)=out(i,1);
%
            newout(i,2)=out(i,4);
%
    end
    end
    if rtime<=(0.0625*pumptime)
%Add pump profile to array
        pumppower=rtime*Pmax/(.0625*pumptime);
%
    elseif rtime>(0.0625*pumptime)&&rtime<=(.9375*pumptime)
%
            pumppower=(-0.4*Pmax*8*(rtime-.0625*pumptime)/(7*pumptime))+Pmax;
%
    elseif rtime>(.9375*pumptime)&&rtime<=pumptime
%
            pumppower=-.6*Pmax*(rtime-
0.9375*pumptime)/(0.0625*pumptime)+0.6*Pmax;          %
    else
%
        pumppower=0;
%
    end
%
newout(i,3)=pumppower;
%
end

%convolve detector response with laser output
outconv1(:,2)=conv(newout(:,2),detector);
[n1]=size(outconv1);
for i=1:n1
    time(i)=rstep*(i-1);
end
%save detector convolved output into outconv array
outconv1(:,1)=time;
outconv=outconv1;
out=newout;
toc
```

Streamlined code to produce Eout vs. Ein curves

```
function [outputenergy]=longpenergy(pumpenergy,R1)
% Longpulse Rate Equation Integrator
% dflux/dt=(flux)*c*n*(l/l')sigma-(L-lnR)/(res lifetime)+(l/l')*n*omega/tau
% dn/dt = P*eff/(hv)-gamma*n*c*flux*sigma
% Pout = (1-R1)/(1+R1)*A*hv*c*flux

%constants
c=2.998e8;                          %speed of light (m/s)
h=6.626e-34;                        %plank's constant (J*s)
k=1.380658e-23;                      %boltzmann's constant (J/K)

%material properties
peakwave=1.533e-6;                  %peak emission cross section wavelength (m)
wavelengther=1.58e-6;              %laser emission wavelength (m)
wavelengthcr=.65e-6;                %pump band wavelength (m)
penergyer=h*c/wavelengther;         %energy of laser photon (J)
penergycr=h*c/wavelengthcr;         %energy of pump photon (J)
penergypeak=h*c/peakwave;           %energy of peak cross section wavelength (J)
sigmaer=2.61e-25;                      %stimulated emission cross section at 20C
(m)
sigmacr=5e-26;                      %absorption cross section of pump (m)
gamma=2;                            %degeneracy factor
tau21=8e-3;                         %lifetime of emission transition
tau30=3e-3;                         %lifetime of pump transition
tautran=204e-6;                     %transfer lifetime from pump to emission band
ntoter=1.2e25;                      %ion density of lasing ion (#/m^3)
ntotcr=1.2e26;                      %ion density of pump ion (#/m^3)


% resonator properties
%R1=.8;                             %output coupler reflectivity
R2=.999;                               %reflectivity of HR mirror
l=.03;                              %gain material length (m)
lprime=15e-2;                       %resonator length (m)
spl=.044;                            %single pass loss
dia=.003;                           %rod diameter (m)
area=pi()*(dia/2)^2;                %rod cross sectional area (m^2)
zeta=1;                            %mode overlap parameter
marea=zeta*area;                    %effective cross sectional area of laser mode
in cavity
L=-2*log(1-spl);                    %double pass logritmic loss
epsilon=L-log(R1*R2);               %loss factor
reslife=2*lprime/c;                 %resonator lifetime (s)
omega=2*marea/(lprime/2)^2;          %solid angle of resonant mode for
spontaneous emission

%initial conditions
```

```
n1=ntoter;                          %initial occupation of lower laser level
(#/m^3)
n2=0;                               %initial occupation of upper laser lavel
(#/m^3)
n0=ntotcr;                          %initial occupation of lower pump level
(#/m^3)
n3=0;                               %initial occupation of upper pump level
(#/m^3)
%flux=0;
flux=1/(marea*l);                    %initial photon density in cavity (#/m^3)
n=n2-(gamma-1)*n1;                  %initial inversion (#/m^3)

%pump properties
eta=.0047;                              %pump efficiency at 20C
%pumpenergy=80;                          %energy in pump pulse
pumptime=800e-6;                        %length of pump pulse
Pmax=pumpenergy/(.75*pumptime);         %peak power of pump pulse
%pumppower=pumpenergy/pumptime;

%timestep
totaltime=1.8e-3;%pumptime*1.25+tautran;        %total integration time
step=totaltime/1000;                            %default time step

%temperature dependent variables
temperature=20;
dsigemissdT=0;
%rate of change of emssion cross section per Kelvin
sigmaer=(temperature-20)*dsigemissdT+sigmaer;
%emssion cross section is equal to (delta_sigma + sigma)
sigmaerabs=sigmaer*exp(-(penergypeak-penergyer)/(k*(temperature+273.15)));
%absorption cross section from emission cross section using reciprocity
detadT=0;
%rate of change in pump efficiency per degree C
eta=eta+(temperature-20)*detadT;
%pump efficiency at given temperature

%calculation
j=1;
time=0;                                         %elapsed time (initially set
to zero)
timestep=1e-10;                                  %starting timestep (s)
Pout=0;
Eout=0;
%tic
while time<totaltime
    if time<=(0.0625*pumptime)
% creates pump power distribution
        pumppower=time*Pmax/(.0625*pumptime);
%
    elseif time>(0.0625*pumptime)&&time<=(.9375*pumptime)
%
            pumppower=(-0.4*Pmax*8*(time-.0625*pumptime)/(7*pumptime))+Pmax;
%
```

```
    elseif time>(.9375*pumptime)&&time<=pumptime
%
            pumppower=-.6*Pmax*(time-
0.9375*pumptime)/(0.0625*pumptime)+0.6*Pmax;           %
    else
%
        pumppower=0;
%
    end
%
    dfluxdt=flux*c*(n2*sigmaer-(gamma-1)*n1*sigmaerabs)*(l/lprime)*zeta-
flux*epsilon/reslife+n2*(l/lprime)*omega/tau21;  %  numerical integration
    dn3dt=pumppower*eta*sigmacr*n0/(penergycr*area*l)-n3/tau30-n3/tautran;
%       |
    dn2dt=n3/tautran-n2/tau21-(n2*sigmaer-(gamma-1)*n1*sigmaerabs)*c*flux;
%       |
    dn1dt=-dn2dt;
%       v
    dn0dt=-dn3dt;
    dflux=dfluxdt*timestep;
    dn3=dn3dt*timestep;
    dn2=dn2dt*timestep;
    dn1=dn1dt*timestep;
    dn0=dn0dt*timestep;
    n3=n3+dn3;
    n2=n2+dn2;
    n1=n1+dn1;
    n0=n0+dn0;
    n=n2-(gamma-1)*n1;
%       ^
    flux=flux+dflux;
%       |
    time=time+timestep;
%       |
    Poutnew=(1-R1)/(1+R1)*marea*penergyer*c*flux;
%       |
    Eoutnew=Eout+(Poutnew+Pout)*timestep/2;
    Pout=Poutnew;
    Eout=Eoutnew;
end
%toc
outputenergy=Eout;
```

Siumulation Code for Passive Q-switch Modeling

```
function [out,eout,outconv]=qpulse(temperature,spl,eta,pumpenergy)
% passive q switch pulse Rate Equation Integrator
% dflux/dt=(flux)*c*n*(l/l')sigma-(L-lnR)/(res lifetime)+(l/l')*n*omega/tau
% dn/dt = P*eff/(hv)-gamma*n*c*flux*sigma
% Pout = (1-R1)/(1+R1)*A*hv*c*flux
tic
%constants
c=2.998e8;                          %speed of light (m/s)
h=6.626e-34;                        %plank's constant (J*s)
k=1.380658e-23;                      %boltzmann's constant (J/K)

%material properties
peakwave=1.533e-6;                  %peak emission cross section wavelength (m)
wavelengther=1.555e-6;              %laser emission wavelength (m)
wavelengthcr=.65e-6;                %pump band wavelength (m)
penergyer=h*c/wavelengther;         %energy of laser photon (J)
penergycr=h*c/wavelengthcr;         %energy of pump photon (J)
penergypeak=h*c/peakwave;           %energy of peak cross section wavelength (J)
sigmaer=5e-25;                      %stimulated emission cross section at 20C (m)
sigmacr=5e-26;                      %absorption cross section of pump (m)
gamma=2.2;                            %degeneracy factor
tau21=8e-3;                         %lifetime of emission transition
tau30=3e-3;                         %lifetime of pump transition
tautran=204e-6;                     %transfer lifetime from pump to emission band
ntoter=1.2e25;                      %ion density of lasing ion (#/m^3)
ntotcr=1.2e26;                      %ion density of pump ion (#/m^3)


% resonator properties
R1=.7;                             %output coupler reflectivity
R2=.99;                               %reflectivity of HR mirror
l=.03;                              %gain material length (m)
lprime=15e-2;                       %resonator length (m)
%spl=.02;                            %single pass loss
qloss=.05;                          %q switch loss
dia=.003;                           %rod diameter (m)
area=pi()*(dia/2)^2;                %rod cross sectional area (m^2)
zeta=1;                            %mode overlap parameter
marea=zeta*area;                    %effective cross sectional area of laser mode
in cavity
Lopen=-2*log(1-spl);                    %double pass logritmic loss with q switch
open
epsilonopen=Lopen-log(R1*R2);               %loss factor with q switch open
Lclose=-2*log(1-(spl+qloss));                    %double pass logritmic loss with
q switch closed
epsilonclose=Lclose-log(R1*R2);               %loss factor with q switch closed
epsilon=epsilonclose;
reslife=2*lprime/c;                 %resonator lifetime (s)
omega=2*marea/(lprime/2)^2;          %solid angle of resonant mode for
spontaneous emission
```

```
%initial conditions
n1=ntoter;                          %initial occupation of lower laser level
(#/m^3)
n2=0;                               %initial occupation of upper laser lavel
(#/m^3)
n0=ntotcr;                          %initial occupation of lower pump level
(#/m^3)
n3=0;                               %initial occupation of upper pump level
(#/m^3)
%flux=0;
flux=1/(marea*l);                    %initial photon density in cavity (#/m^3)
n=n2-(gamma-1)*n1;                  %initial inversion (#/m^3)

%pump properties
%eta=.0047;                             %pump efficiency at 20C
%pumpenergy=28;                         %energy in pump pulse
pumptime=800e-6;                       %length of pump pulse
Pmax=pumpenergy/(.75*pumptime);        %peak power of pump pulse
%pumppower=pumpenergy/pumptime;

%timestep
totaltime=1.8e-3;%pumptime*1.25+tautran;        %total integration time
step=totaltime/1000;                            %default time step

%temperature dependent variables
dsigemissdT=0;
%rate of change of emssion cross section per Kelvin
sigmaer=(temperature-20)*dsigemissdT+sigmaer;
%emssion cross section is equal to (delta_sigma + sigma)
sigmaerabs=sigmaer*exp(-(penergypeak-penergyer)/(k*(temperature+273.15)));
%absorption cross section from emission cross section using reciprocity
detadT=-.00001;
%rate of change in pump efficiency per degree C
eta=eta+(temperature-20)*detadT;
%pump efficiency at given temperature

%calculation
j=1;
time=0;                                         %elapsed time (initially set
to zero)
timestep=1e-10;                                  %starting timestep (s)
out(1,1)=time;
out(1,2)=n;
out(1,3)=flux;
out(1,4)=(1-R1)/(1+R1)*marea*penergyer*c*flux;
while time<totaltime
    if time<=(0.0625*pumptime)
% creates pump power distribution
        pumppower=time*Pmax/(.0625*pumptime);
%
    elseif time>(0.0625*pumptime)&&time<=(.9375*pumptime)
%
```

```
            pumppower=(-0.4*Pmax*8*(time-.0625*pumptime)/(7*pumptime))+Pmax;
%
    elseif time>(.9375*pumptime)&&time<=pumptime
%
            pumppower=-.6*Pmax*(time-
0.9375*pumptime)/(0.0625*pumptime)+0.6*Pmax;           %
    else
%
        pumppower=0;
%
    end
%
    dfluxdt=flux*c*(n2*sigmaer-(gamma-1)*n1*sigmaerabs)*(l/lprime)*zeta-
flux*epsilon/reslife+n2*(l/lprime)*omega/tau21;  %  numerical integration
    dn3dt=pumppower*eta*sigmacr*n0/(penergycr*area*l)-n3/tau30-n3/tautran;
%       |
    dn2dt=n3/tautran-n2/tau21-(n2*sigmaer-(gamma-1)*n1*sigmaerabs)*c*flux;
%       |
    dn1dt=-dn2dt;
%       v
    dn0dt=-dn3dt;
    dflux=dfluxdt*timestep;
    dn3=dn3dt*timestep;
    dn2=dn2dt*timestep;
    dn1=dn1dt*timestep;
    dn0=dn0dt*timestep;
    newn3=n3+dn3;
    newn2=n2+dn2;
    newn1=n1+dn1;
    newn0=n0+dn0;
    newn=newn2-(gamma-1)*newn1;
%       ^
    newflux=flux+dflux;
%       |
    newtime=time+timestep;
%       |
    Pout=(1-R1)/(1+R1)*area*penergyer*c*newflux;
%       |


    if ((j==1)||((abs((newn-n)/n)<.1)&&(abs((newflux-
flux)/flux)<.1))||(timestep<1e-12))&&newflux>0         % if values of n and
flux
        out(j+1,1)=newtime;
% are stable, or time step is
        out(j+1,2)=newn;
% too small the load values into
        out(j+1,3)=newflux;
% output matrix
        out(j+1,4)=Pout;
        out(j+1,5)=pumppower;
        time=newtime;
        n3=newn3;
```

```
        n2=newn2;
        n1=newn1;
        n0=newn0;
        n=newn;
        flux=newflux;
        timestep=step;
        j=j+1;
    else
        timestep=timestep/2;
% if not, then halve the time step
    end
% and try again
    if (flux*c*(n2*sigmaer-(gamma-
1)*n1*sigmaerabs)*(l/lprime)*zeta)>(flux*epsilon/reslife)
        epsilon=epsilonopen;
    end
    if (flux*c*(n2*sigmaer-(gamma-
1)*n1*sigmaerabs)*(l/lprime)*zeta)<(flux*epsilon/reslife)
        epsilon=epsilonclose;
    end
    %time
end
j
%calculate total enrgy in output pulse
for i=1:(j-1)
    dpower(i)=(out(i+1,4)+out(i,4))/2;
    dtime(i)=out(i+1,1)-out(i,1);
    energy(i)=dpower(i)*dtime(i);
end
eout=sum(energy);               %total energy in output pulse

%resample data and create even time steps
numrsteps=10000;
%number of steps in new array
rstep=totaltime/numrsteps;
%time increment of new step
detector=rc(20e-6,rstep,totaltime);
%create detector response data
[num,j]=size(out);
%determine size of initial data array
j=0;
for i=1:(numrsteps)
    rtime=rstep*(i-1);
    for j=1:(num-1)
%create new, resampled array called newout
    if rtime>out(j,1)&&rtime<out(j+1,1)
%
        dy=out(j+1,4)-out(j,4);
%
        dt=out(j+1,1)-out(j,1);
%
        newdt=rtime-out(j,1);
%
```

```
        newdy=newdt*dy/dt;
%
        newy=out(j,4)+newdy;
%
        newout(i,1)=rtime;
%
        newout(i,2)=newy;
%
    elseif time==0
%
            newout(i,1)=out(i,1);
%
            newout(i,2)=out(i,4);
%
    end
    end
    if rtime<=(0.0625*pumptime)
%Add pump profile to array
        pumppower=rtime*Pmax/(.0625*pumptime);
%
    elseif rtime>(0.0625*pumptime)&&rtime<=(.9375*pumptime)
%
            pumppower=(-0.4*Pmax*8*(rtime-.0625*pumptime)/(7*pumptime))+Pmax;
%
    elseif rtime>(.9375*pumptime)&&rtime<=pumptime
%
            pumppower=-.6*Pmax*(rtime-
0.9375*pumptime)/(0.0625*pumptime)+0.6*Pmax;          %
    else
%
        pumppower=0;
%
    end
%
newout(i,3)=pumppower;
%
end
%plot(newout(:,2))
%figure
%plot(detector)
%figure
%convolve detector response with laser output
outconv1(:,2)=conv(newout(:,2),detector);
[n1]=size(outconv1);
for i=1:n1
    time(i)=rstep*(i-1);
end
%save detector convolved output into outconv array
outconv1(:,1)=time;
%plot(outconv1(:,1),outconv1(:,2))
outconv=outconv1;
%out=newout;
toc
```

REFERENCES

1. T.H. Maiman, “Stimulated optical radiation in ruby". *Nature*, Vol. 187 pp. 493–494, 1960.
2. E. Snitzer, “Optical Maser Action of Nd^{3+} in a Barium Crown Glass,” *Physical Review Letters*, Vol. 7, No. 12, pp.444-446, 1961.
3. T. McComb, M. Richardson, and M. Bass, “High-Power Fiber Lasers and Amplifiers,” Handbook of Optics, Third Edition, Vol. 5, New York: McGraw-Hill, 2010.
4. J. Buck, “Nonlinear Effects in Optical Fibers,” Handbook of Optics, Third Edition, Vol. 5, New York: McGraw-Hill, 2010.
5. J. Reintjes, M. Bashkasky, “Stimulated Raman and Brillouin Scattering,” Handbook of Optics, Third Edition, Vol. 4, New York: McGraw-Hill, 2010.
6. Y. Chen, V. Sudesh, T. McComb, M. Richardson, M. Bass, J. Ballato, “Lasing in a gain-guided index antiguided fiber,” *Journal of the Optical Society of America B*, vol. 24, pp. 1683-1688, 2007.
7. Y. Chen, T. McComb, V. Sudesh, M. Richardson, and M. Bass, “Very large-core, single-mode, gain-guided, index-antiguided fiber lasers,” *Optics Letters*, vol. 32, no. 17, pp. 2505-2507, 2007.
8. E. Snitzer, “Proposed Fiber Cavities for Optical Masers,” *Journal of Applied Physics,* Volume 32, pp. 36, 1961.
9. C. J. Koester and E. Snitzer, “Amplification in a Fiber Laser,” *Applied Optics,* Vol. 3, No. 10, pp. 1182-1186, 1964.
10. J. Stone and C.A. Burrus, “Neodymium-Doped Silica Lasers in End-Pumped Fiber Geometry,” *Applied Physics Letters*, Vol. 23, pp. 388, 1973.

11. J. Stone and C. A. Burrus, “Neodymium-Doped Fiber Lasers: Room Temperature CW Operation with an Injection Laser Pump,” *IEEE Journal of Quantum Electronics*, Vol. 10, No. 9, pp 794, 1974.

12. R. J Mears, L. Reekie, S. B. Poole, D. N. Payne, “Neodymium-Doped Silica Single-Mode Fiber Lasers,” *Electronics Letters*, Vol. 21, pp. 738, 1985.

13. R. J Mears, L. Reekie, S. B. Poole, D. N. Payne, “Low-Threshold Tunable CW and Q-Switched Fibre Laser Operating at 1.55 μm,” *Electronics Letters*, Vol. 22, pp.159, 1986.

14. L. Reekie, R. Mears, S. Poole, and D. N. Payne, “Tunable Single-Mode Fiber Lasers,” *Journal of Lightwave Technology*, Vol. 4, No. 7, pp 956-960, 1986.

15. E. Snitzer, H. Po, F. Hakimi, R. Tumminelli, and B. C. McCollum, “Double-Clad, Offset Core Nd Fiber Laser,” *Optical Fiber Sensors Conference Proc.*, Vol. 1, 1988.

16. V. Dominic, S. MacCormack, R. Waarts, S. Sanders, S. Bicknese, R. Dohle, E. Wolak, P. Yeh, and E. Zucker, “110W Fibre Laser,” *Electronics Letters*, Vol. 35, No. 14, pp. 1158-1160, 1999.

17. C.C. Ranaud, H. L. Offerhaus, J. Nilsson, W. A. Clarkson, P. Turner, D. J. Richardson, and A. B. Grudinin, “Characteristics of Q-switched Cladding-Pumped Ytterbium-Doped Fiber Lasers with Different High-Energy Fiber Designs,” *IEEE Journal of Quantum Electronics*, Vol. 37, No. 2, pp. 199-206, 2001.

18. J. W. Dawson, M. J. Messrly, R. J. Beach, M. Y. Shverdin, E. A. Stappaerts, A. K. Sridharan, P. H. Pax, J. E. Heebner, C. W. Siders, and C. P. J. Barty, “Analysis of the Scalability of Diffraction-Limited Fiber Lasers and Amplifiers to High Average Power,” *Optics Express*, Vol. 16, No. 17, pp.13240-13266, 2008

19. V. Fomin, A. Mashkin, M. Abramov, A. Ferin, and V. Gapontsev, "3kW Yb Fiber Lasers with a Single Mode Output," *International Symposium on High Power Fiber Lasers and Their Applications*, St. Petersburg, 2006.

20. J. A. Buck, Fundamentals of Optical Fibers, New York:Wiley-IEEE Press, 2004.

21. A. Yariv, Optical Electronics in Modern Communications, 5th edition, New York: Oxford University Press,1997.

22. J. A. Alvarez-Chavez, H.L. Offerhaus, J. Nilsson, P. Turner, W. A. Clackson, P. Turner, D. J. Richardson, and A. B. Gudinin, "High-Energy, High-Power Ytterbium-Doped Q-Switched Fiber Laser," *Optics Letters*, Vol. 25, No. 1. pp. 37-39, 2000.

23. J. P. Koplow, D. A. V. Kliner, and L. Goldberg, "Single-Mode Operation of a coiled Multimode Fiber Amplifier," *Optics Letters*, Vol. 25, No.7, pp.442-444, 2000.

24. D. Marcuse, "Curvature Loss Formula for Optical Fibers," *Journal of the Optical Society of America*, Vol. 66, No. 3, pp.216, 1976.

25. R. T. Schermer, "Mode Scalability in Bent Optical Fibers," *Optics Express*, Vol.15, No. 24, pp. 15674-15701, 2007.

26. J. W. Dawson, R. J Beach, I. Jovanovic, W. Benoit, Z. Liao, and S. Payne, "Large Flattened Mode Optical Fiber for Reduction of Nonlinear Effects," *Proceedings of SPIE, Vol. 5335 Fiber Lasers: Technology, Systems and Applications*, 2004.

27. A. K. Ghatak, I. C. Goyal, and R. Jindal, "Design of a Waveguide Refractive Index Profile to Obtain a Flat Modal Field," *International Conference on Fiber Optics and Photonics: Selected Papers from Photonics India '98*, New Delhi, India:SPIE, 1999.

28. P. S. J. Russell, "Photonic-Crystal Fibers," *Journal of Lightwave Technology*, Vol. 24, No. 12, pp.4729-4749, 2006.

29. J.C. Knight, "Photonic Crystal Fibers and Fiber Lasers (Invited)," *Journal of the Optical Society of America B*, Vol. 24, No. 8, pp.1661-1668, 2007.

30. T. A. Birks, J. C. Knight, and P. S. J. Russell, "Endlessly Single-Mode Photonic Crystal Fiber," Optics Letters, Vol. 22, No. 13, pp. 961-963, 1997.

31. F. Qiang, W. Shi, K. Guiyun, Long Jin., Yang Yue., J. Du., Q. Shi, Q. Liu, B. Liu, Y. Liu, S. Yuan, and X. Dong, "Proposal for All-Solid Photonic Bandbgap Fiber with Improved Dispersion Characteristics," *Photonics Technology Letters IEEE*, Vol. 19, No. 16, pp. 1239-1241, 2007.

32. L. Dong, J. Li, H. McKay, A. Marcinkevicius, B. Thomas, M. Moore, L. Fu, and M. E. Fermann, "Robust and Practical Optical Fibers for Single Mode Operation with Core Diameters up to 170 μm," in *CLEO 2008*, San Jose, California, 2008.

33. L. Dong, X. Peng, and J. Li, "Leakage Channel Optical Fibers and Large Effective Area," *Journal of the Optical Society of America B*, Vol. 34, No. 8, pp.1689-1697, 2007.

34. W. S. Wong, W. Peng, J. M. Mclaughlin, and L. Dong, "Breaking the Limit of Maximum Effective Area for Robust Single-Mode Propagation in Optical Fibers," *Optics Letters*, Vol. 30, No. 21, pp. 2855-2857, 2005.

35. M. C. Swan, C. H. Liu, D. Guertin, N. Jacobson, K. Tankala, and A. Galvanauskas, "33 μm Core Effectively Single-Mode Chirally-Coupled-Core Fiber Laser at 1064 nm," *Optical Fiber Communication Conference and Exposition and the National fiber Optic Engineers Conference*, San Diego, California, 2008.

36. C. H. Liu, G. Chang, N. Litchinister, D. Guertin, N. Jacobson, K. Tankala, and A. Galvanauskas, "Chirally Coupled Core Fibers at 1500-nm and 1064-nm for Effectively Single-Mode Core Size Scaling," in *CLEO*, Baltimore, Maryland, 2007.

37. R. J. Beach, M. D. Feit, R. H. Page, L. D. Brasure, R. Wilcox, and S. A. Payne, "Scalable Antiguided Ribbon Laser," Journal of the Optical Society of America B, Vol. 19, No. 7, pp. 1521-1534, 2002.

38. M. Wrage, P. Glas, M. Leitner, T. Sandrock, N. N. Elkin, A. P. Napartovich, and A. G. Sukharev, "Experimental and Numerical Determination of Coupling Constant in a Multicore Fiber," Optical Communication, Vol. 175, pp. 97-102, 2000.

39. A. E. Siegman, "Propagating modes in gain-guided optical fibers," *Journal of the Optical Society of America A*, vol. 20, pp. 1617-1628, 2003.

40. A. E. Siegman, Y. Chen, V. Sudesh, M. Richardson, M.Bass, P. Foy, W. Hawkins, and J. Ballato, "Confined propagation and near single-mode laser oscillation in a gain-guided, index antiguided optical fiber," *Applied Physics Letters,* vol. 89, 251101, 2006.

41. A. E. Siegman, "Gain-guided, index-antiguided fiber lasers," *Journal of the Optical Society of America B*, vol. 24, no. 8, pp. 1677-1682, 2007.

42. V. Sudesh, T. McComb, Y. Chen, M. Bass, M. Richardson, J. Ballato, A. E. Siegman, "Diode-pumped 200 μm diameter core, gain-guided, index-antiguided single mode fiber laser," *Applied Physics B*, Vol. 90, pp. 369-372, 2008.

43. X. Wang, C. Xiong, and W. Xie, "Field deformation and loss by curvature in gain guided and index anti-guided fibrs," *Optics Communications*, Vol. 281, pp. 4626-4630, 2008.

44. W. Xie, C. Xiong, X. Wang, Z. Wang, Y. Liu, "Single-Mode Parabolic Gain-Guiding Optical Fiber with Core Diameter up to 200 μm," *International Journal of Infrared and Millimeter Waves*, Vol. 29, pp. 406-415, 2008.

45. X. Wang, C. Xiong, Q. Qiu, X. Wen, "Analysis of Ytterbium-doped gain guided and index antiguided fiber amplifier," *Proceedings of SPIE*, Vol. 7278, 72780C, 2009.

46. X. Wang, C. Xiong, J. Luo, "Coupling coefficients evaluation of a directional coupler using gain guided and index antiguided fibers," *Optics Communications*, Vol. 282, pp.382-386, 2009.

47. V. P. Gapontsev, P. I. Sawvsky, and I.E. Smartsev, "1.5 μm Erbium Glass Lasers," in *Conference on Lasers and ElectroOptics*, San Jose, California, 1990.

48. D. Minelly, E. R. Taylor, K. P. Iedrzuewiski, J. Wang, and D. N. Paune, "Laser-Diode Pumped Neodymium-Doped Fibre Laser with Output Power >1W," in *Conference on Lasers and ElectroOptics*, 1992.

49. H. Po, J. D. Cao, B. M. Laiberte, R. A .Minns, R. F. Robinson, B. H. Rockney, R. R. Tricca, and Y. H. Zhang, "High Power Neodymium-Doped Single Transverse Mode Fibre Laser," *Electronics Letters*, Vol 29, No. 17, pp. 1500-1501, 1993.

50. W. Koechner, "Solid-State Laser Engineering", 6th, rev. and updated ed., Springer (2006).

51. N. E. Alexseev, A. A. Izyneev, V. B. Kravchenko, Yu. S. Milyavskii, and S. P. Rozman, "Etching of Phosphate Glasses," *Steklo I Keramika*, No. 7, pp. 11-12, 1983.

52. M. Sparks, "Optical Distortion by Heated Windows in High-Power Laser Systems", *Journal of Applied Physics*, Vol. 42, pp. 5029 (1971).

53. Hans J. Hoffmann, Werner W. Jochs, and Gerhard Westenberger, “Dispersion formula for the thermo-optic coefficient of optical glasses”, *Proceedings of SPIE,* Vol. 1327, pp. 219 (1990).

54. Jonathan F. Schonfeld, “Analysis and modeling of thermal blooming compensation”, *Proceedings of SPIE*, Vol. 1221, pp. 118 (1990).

55. M. Bass, L. Weichman, S. Vigil, and B. Brickeen, “The Temperature Dependence of Nd^{3+} Doped Solid-State Lasers*”, IEEE Journal of Quantum Electronics*, Vol. 39, No.6 (2003).

56. J. Koroshetz, B. Brickeen, S.Fahr, A. Rapaport, and M. Bass , "Athermal Emission in Yb,Er:glass," *Optics Express*, V.15, No.18, pp 11530-11535 (2007).

57. T.Y. Chung and M. Bass, “Temperature-independent lasers using output couplers with temperature-dependent reflectivity”, *Applied Optics*, **Vol.** 45, No. 36, **pp** 9198-9202 (2006).

50. W. Koechner, “Solid-State Laser Engineering”, 6th, rev. and updated ed., Springer (2006).

59. Optigrate Inc., 3267 Progress Drive, Orlando, Florida 32826

60. E. Hecht, “Optics”, 4th Ed., Pearson Education Inc., (2002).

61. O. Efimov, L. Glebov, L. Glebova, K. Richardson and V. Smirnov, “High-Efficiency Bragg gratings in photothermorefractive glass”, *Applied Optics*, Vol. 38, No. 4 (1999).

62. L. Glebov, V. Smirnov, C.M. Stickley and I. Ciapurin, “New Approach to Robust Optics for HEL Systems”, *Proceedings of SPIE*, Vol. 4724, pp 101, (2002)

63. O. M. Efimov, L. B. Glebov, L. N. Glebova, and V. I. Smirnov, “Process for production of high efficiency volume diffractive elements in photo-thermo-refractive glass,” U. S. Patent 6,586,141 B1 (July 1, 2003).

64. O. M. Efimov, L. B. Glebov, and V. I. Smirnov, “High efficiency volume diffractive elements in photo-thermorefractive glass,” U. S. Patent 6,673,497 B2 (January 6, 2004).

65. L. Glebov, “Volume Bragg Gratings in PTR Glass--New Optical Elements for Laser Design”, *ASSP Technical Digest*, Paper Code MD1, (2008).

66. T.Y. Chung, A. Rapaport, V. Smirnov, L.B. Glebov, M.C. Richardson, and M. Bass, “Solid-state laser spectral narrowing using a volumetric photothermal refractive Bragg grating cavity mirror”, *Optics Letters*, Vol. 31, No. 2, pp 229-231 (2006).

67. J. K. Franks, “What is eye safe?”, *Proceedings of SPIE*, 2 (1991).

68. V. P. Gapontsev, S. M. Matisin, A. A. Isineev and V. B. Kravchenko, “Erbium glass lasers and their applications”, *Optics and Laser Technology*, Vol. 14, pp. 189, (1982).

69. V.V. Akulinichev, I.V. Kurnin and E. G. Kurochkina, “Eye-safe Lidar by the Solid State Er:glass Laser”, *Proceedings of SPIE*, Vol. 5478, pp. 291 (2003).

70. Z. J. Kiss and R. C. Duncan, “Optical Maser Action in CaWO4:Er^{3+}”,*Proceedings of IRE*, Vol. 50, pp. 1531 (1962).

71. E. Snitzer and R. Woodcock, “Yb^{3+} - Er^{3+} Glass Laser”, *Applied Physics Letters* 6, 45 (1965).

72. P. Laporta, S. De Silverstri, V. Magni and O. Svelto, “Diode-pumped cw bulk Er:Yb:glass laser”, *Optics Letters*, Vol. 16, No. 24, (1991).

73. E. Snitzer, R. Woodcock and J. Segre, “Phosphate Glass Er^{3+} Laser”, *IEEE Journal of Quantum Electronics*, Vol. 4, No. 5, 360, (1968).

74. Kigre, Inc., “Datasheet for QX/Er Glass”, 100 Marshland Road, Hilton Head, SC.

75. M. Lukac and M. Marincek, “Effect of sensitizers on flash lamp pumping efficiency and heat deposition in Er-glasses”, *Proceedings of SPIE*, Vol. 1277, pp. 40, (1990).

76. E. Desurvire and J.R. Simpson, “Evaluation of $^4I_{15/2}$ and $^4I_{13/2}$ Stark-level energies in Erbium-doped aluminosilicate glass fibers”, *Optics Letters*, Vol. 15, No. 10 (1990).

77. C. C. Robinson, “Multiple sites for Er^{3+} in alkali silicate glasses (I). The principal sixfold coordinated site of Er^{3+} in silicate glass”, *Journal of Non-Crystalline Solids* 15, 1 (1974).

78. N. E. Alekseev, V. P. Gapontsev, M. E. Zhabotinskii, V.B. Kravchenko, and Yu. P. Rudnitskii, “*Laser Phosphate Glasses”*, M. E. Zhabotinskii, ed. (Nauka, Moscow, 1980).

79. T.Y. Chung, V. Smirnov, M. Hemmer, L. B. Glebov, M. C. Richardson, and M. Bass, “Unexpected properties of a laser resonator with volumetric Bragg grating end mirrors,” in *Conference on Lasers and Electro-Optics_Quantum Electronics and Laser Science,* (OSA, 2006).

80. F. J. McClung and R. W. Hellwarth, “Giant Optical Pulsations from Ruby,” *Journal of Applied Physics,* Vol. 33, No. 3, pp. 828-829, 1962.

81. B. H Soffer, “Giant Pulse Operation by a Passive, Reversibly Bleachable Absorber,” *Communications*, pg. 2551, 1964.

82. K. Yumashev, “Saturable absorber Co^{2+}:$MgAl_2O_4$ crystal for Q switching of 1.34-μm Nd^{3+}:$YAlO_3$ and 1.54-μm Er^{3+}:glass lasers,” *Applied Optics,* Vo. 38, No. 30, pp.6343-6346, 1999.

83. B. Denker, B. Galagan, E. Godovikova and M. Meilman, V. Osiko, S. Sverchkov, “The Efficient Saturable Absorber for 1.54 μm Er Glass Lasers,” *OSA TOPS Advanced Solid State Lasers,* Vol. 26, pp. 618-620, 1999.

84. R. Wu, J. D. Myers, M. J. Myers, B. Denker, B. Galagan, S. Sverchkov and J. Hutchinson, "Co^{2+}:$MgAl_2O_4$ Crystal Passive Q-Switch Performance At 1.34, 1.44 and 1.54 micron," *ASSL conference*, 2000.

85. R. Wu, T. Chen, J. D. Myers, M. J. Myers and C. Hardy, "Multi-Pulses Behavior in a Erbium Glass laser Q-switched by Cobalt Spinal," *AreoSense 2003*, Orlando, Florida, 2003.

86. A. McInnes and J. Richards, "Thermal Properties of Erbium Glass Lasers," *OSA Proceedings on Advanced Solid-State Lasers*, Vol. 15, pp. 229-232, 1993.

87. B. Denker, B. Galagan and S. Sverchkov, "Temperature Efficiency Variations of Erbium Glass Lasers," *OSA TOPS Advanced Solid State Lasers*, Vol. 19, pp. 469-471, 1998.

88. V. Sudesh, T. McComb, M. Richardson, W. Hageman, M. Bass, J. Ballato, A. Siegman "Waveguide-pumping gain guided index antiguided fiber laser," U. S. Patent 7,668,211 (February 23, 2010).